

**AFRL-PR-WP-TR-2007-2033**

**RESEARCH ON NITRIDE THIN  
FILMS, ADVANCED PLASMA  
DIAGNOSTICS, AND CHARGED-  
PARTICLE PROCESSES**



**William C. Lanter  
Wei Guo, Ph.D.  
Charles Q. Jiao, Ph.D.**

**Innovative Scientific Solutions, Inc.  
2766 Indian Ripple Road  
Dayton, OH 45440-3638**

**David C. Ingram, Ph.D.  
Ohio University  
Department of Physics and Astronomy  
Athens, OH 45701**

**JULY 2006**

**Final Report for 21 July 2000 – 01 June 2006**

**Approved for public release; distribution unlimited.**

**STINFO COPY**

**PROPULSION DIRECTORATE  
AIR FORCE MATERIEL COMMAND  
AIR FORCE RESEARCH LABORATORY  
WRIGHT-PATTERSON AIR FORCE BASE, OH 45433-7251**

## NOTICE AND SIGNATURE PAGE

Using Government drawings, specifications, or other data included in this document for any purpose other than Government procurement does not in any way obligate the U.S. Government. The fact that the Government formulated or supplied the drawings, specifications, or other data does not license the holder or any other person or corporation; or convey any rights or permission to manufacture, use, or sell any patented invention that may relate to them.

This report was cleared for public release by the Air Force Research Laboratory Wright Site (AFRL/WS) Public Affairs Office and is available to the general public, including foreign nationals. Copies may be obtained from the Defense Technical Information Center (DTIC) (<http://www.dtic.mil>).

AFRL-PR-WP-TR-2007-2033 HAS BEEN REVIEWED AND IS APPROVED FOR PUBLICATION IN ACCORDANCE WITH ASSIGNED DISTRIBUTION STATEMENT.

\*//Signature//

CHARLES A. DEJOSEPH, Jr., Ph.D.  
Principal Research Physicist  
Electrical Technology & Plasma Physics Branch

//Signature//

JOSEPH A. WEIMER  
Chief  
Electrical Technology & Plasma Physics Branch

//Signature//

KIRK L. YERKES, Ph.D.  
Deputy for Science  
Power Division

This report is published in the interest of scientific and technical information exchange, and its publication does not constitute the Government's approval or disapproval of its ideas or findings.

\*Disseminated copies will show “//Signature//” stamped or typed above the signature blocks.

# REPORT DOCUMENTATION PAGE

*Form Approved*  
OMB No. 0704-0188

The public reporting burden for this collection of information is estimated to average 1 hour per response, including the time for reviewing instructions, searching existing data sources, gathering and maintaining the data needed, and completing and reviewing the collection of information. Send comments regarding this burden estimate or any other aspect of this collection of information, including suggestions for reducing this burden, to Department of Defense, Washington Headquarters Services, Directorate for Information Operations and Reports (0704-0188), 1215 Jefferson Davis Highway, Suite 1204, Arlington, VA 22202-4302. Respondents should be aware that notwithstanding any other provision of law, no person shall be subject to any penalty for failing to comply with a collection of information if it does not display a currently valid OMB control number. **PLEASE DO NOT RETURN YOUR FORM TO THE ABOVE ADDRESS.**

<b>1. REPORT DATE (DD-MM-YY)</b> July 2006		<b>2. REPORT TYPE</b> Final		<b>3. DATES COVERED (From - To)</b> 07/21/2000 – 06/01/2006	
<b>4. TITLE AND SUBTITLE</b> RESEARCH ON NITRIDE THIN FILMS, ADVANCED PLASMA DIAGNOSTICS, AND CHARGED-PARTICLE PROCESSES				<b>5a. CONTRACT NUMBER</b> F33615-00-C-2055	
				<b>5b. GRANT NUMBER</b>	
				<b>5c. PROGRAM ELEMENT NUMBER</b> 61102F	
<b>6. AUTHOR(S)</b> William C. Lanter, Wei Guo, Ph.D., and Charles Q. Jiao, Ph.D. (Innovative Scientific Solutions, Inc.) David C. Ingram, Ph.D. (Ohio University)				<b>5d. PROJECT NUMBER</b> 2301	
				<b>5e. TASK NUMBER</b> DW	
				<b>5f. WORK UNIT NUMBER</b> 23	
<b>7. PERFORMING ORGANIZATION NAME(S) AND ADDRESS(ES)</b> Innovative Scientific Solutions, Inc. 2766 Indian Ripple Road Dayton, OH 45440-3638				<b>8. PERFORMING ORGANIZATION REPORT NUMBER</b> 2055 Final	
<b>9. SPONSORING/MONITORING AGENCY NAME(S) AND ADDRESS(ES)</b> Propulsion Directorate Air Force Research Laboratory Air Force Materiel Command Wright-Patterson AFB, OH 45433-7251				<b>10. SPONSORING/MONITORING AGENCY ACRONYM(S)</b> AFRL-PR-WP	
				<b>11. SPONSORING/MONITORING AGENCY REPORT NUMBER(S)</b> AFRL-PR-WP-TR-2007-2033	
<b>12. DISTRIBUTION/AVAILABILITY STATEMENT</b> Approved for public release; distribution unlimited.					
<b>13. SUPPLEMENTARY NOTES</b> PAO case number: AFRL/WS 07-0479; Date cleared: 05 Mar 2007. This report contains color.					
<b>14. ABSTRACT</b> This program has three sub-tasks: 1) Nitride Thin-Film Coatings, 2) Advanced Plasma Diagnostics, and 3) Studies of Charged-Particle Processes. The focus of Task 1 has been to develop amorphous carbon-nitride films utilizing controlled plasma-generated ions to increase the nitrogen concentration within the film. It is anticipated that development of films with higher concentrations of nitrogen will lead to properties similar to those theoretically calculated for crystalline $\beta$ -C <sub>3</sub> N <sub>4</sub> . Successful development of this film will facilitate the creation of a smooth, extremely hard, thermally stable amorphous film. Applications can include hard-coating protection, solid lubricants, reduced friction and wear coatings, thermal heat spreaders, and high-temperature dielectrics. In Task 2 advanced diagnostics of plasmas with various operating conditions have been performed to gain a better understanding of the generated plasma fields. Task 3 has utilized Fourier Transform Mass Spectrometry (FTMS) to investigate gas-phase reactions of charged particles. Ion chemistries have been studied in selected compounds of great interest in areas including plasma processing and combustion. Cross sections of electron-impact ionization of these compounds have been measured and the kinetics of the reactions between the ions and their parent molecules examined.					
<b>15. SUBJECT TERMS</b> Carbon Nitride, Electrical Properties, Thermal Stability, Single-Ion-Beam Deposition, Dual-Ion-Beam Deposition, Thin-Film Growth, Plasma Diagnostics, Fourier Transform Mass Spectrometry, Electron-Impact Ionization, Cross Sections, Ion-Molecule Reactions, Plasma-Processing Gases, Combustion					
<b>16. SECURITY CLASSIFICATION OF:</b>			<b>17. LIMITATION OF ABSTRACT:</b> SAR	<b>18. NUMBER OF PAGES</b> 134	<b>19a. NAME OF RESPONSIBLE PERSON (Monitor)</b> Charles A. DeJoseph, Ph.D. <b>19b. TELEPHONE NUMBER (Include Area Code)</b> N/A
<b>a. REPORT</b> Unclassified	<b>b. ABSTRACT</b> Unclassified	<b>c. THIS PAGE</b> Unclassified			

## Table of Contents

<u>Section</u>	<u>Page</u>
<b>TASK 1. CARBON-NITRIDE THIN-FILM COATINGS</b> .....	1
1.0 INTRODUCTION .....	1
2.0 EXPERIMENTAL EQUIPMENT .....	5
2.1 Large-Area-Deposition System (LADS) .....	5
2.1.1 Equipment Modifications .....	6
3.0 COLLABORATIVE RESEARCH .....	11
3.1 Arylite Polymer .....	11
3.2 MEMS .....	12
3.3 Metal Coupon .....	13
3.3.1 Hardness Testing .....	13
3.3.2 Wear Testing .....	14
3.3.3 Corrosion Testing .....	15
3.4 Carbon-Composite Coupons .....	16
4.0 EXPERIMENTAL DETAILS .....	18
4.1 Setup .....	18
4.2 Substrates .....	20
4.3 CN <sub>x</sub> Film Depositions .....	21
4.4 Capacitors .....	22
5.0 RESULTS .....	24
5.1 Deposition-Chamber Preparation .....	24
5.2 Film Adhesion .....	24
5.3 Sample Preparation .....	25
5.4 Film Growth Rate .....	25
5.5 Deposition Temperature .....	27
5.6 Thermal Annealing .....	28
5.7 Imaging .....	30
5.7.1 Optical Microscopy .....	30
5.8 Film Composition .....	33
5.8.1 XPS Analysis .....	37
5.8.2 RBS and ERS Analysis .....	37
5.8.3 X-Ray Diffraction (XRD) .....	50
5.9 IR Transmission .....	50
5.10 Mass Spectroscopy .....	51
5.11 Optical Band Gap .....	52

## Table of Contents (Continued)

<u>Section</u>	<u>Page</u>
5.12 Electrical Characteristics .....	53
5.12.1 n-Type Dopants .....	55
5.12.2 Hydrogen Concentration .....	56
5.12.3 Capacitance .....	56
5.12.4 Dissipation .....	58
5.12.5 Resistivity .....	60
5.12.6 Voltage Breakdown .....	63
5.12.7 Dielectric Constant .....	66
6.0 CONCLUSIONS .....	68
7.0 FURTHER RESEARCH .....	69
8.0 PUBLICATIONS AND PRESENTATIONS .....	70
<b>TASK 2. ADVANCED PLASMA DIAGNOSTICS .....</b>	<b>84</b>
1.0 GENERAL OVERVIEW .....	84
2.0 MEASUREMENTS IN ARGON PULSED ICP .....	85
2.1 Pulsed ICP Plasma Generation and Characterization .....	85
2.2 Time-Resolved Current and Voltage Measurements on Pulsed rf ICP .....	86
2.3 Time-Resolved Langmuir-Probe Measurements on Pulsed ICP Source .....	96
3.0 MEASUREMENTS IN NITROGEN PULSED ICP .....	103
3.1 Investigation of Mode Transitions in Pulsed ICP System .....	103
3.2 Time-Resolved Rotational Temperature Measurements of N <sub>2</sub> and N <sub>2</sub> <sup>+</sup> in Pulsed ICP .....	103
<b>TASK 3. STUDIES OF CHARGED-PARTICLE PROCESSES .....</b>	<b>110</b>
<b>APPENDIX: Ohio University Final Report on the Development of             Nitride Thin Films by Ion-Beam Deposition .....</b>	<b>190</b>

## List of Figures

<b><u>Figure</u></b>		<b><u>Page</u></b>
1	Schematic of LADS .....	5
2	Quartz rf Window .....	8
3	Comparison of DLC, N-DLC, and O-DLC Coated PFE (Arylite) Polymer Films .....	12
4	Photo of Coated Metal Samples .....	17
5	Photo of Carbon-Composite Samples after Coating .....	18
6	Diagram Illustrating Single-Ion-Beam Deposition .....	19
7	Diagram Showing Original Orientation of 20-cm Ion Source, 3-cm Ion Source, and Sample .....	20
8	Schematic of Final Arrangement of Dual-Ion-Beam System, with One Beam Used to Sputter Graphite onto Substrate and Second Used to Bombard Growing Film .....	20
9	Schematic of Developed Parallel-Flat-Plate Capacitor Array .....	23
10	Image of Created Flat-Plate Capacitor Array .....	24
11	CN <sub>x</sub> Deposition Rate for Various Runs and Substrate Materials .....	27
12	Graph of Sample Temperatures during Various Deposition Runs .....	29
13	Elemental Composition of Film with 1.23% Hydrogen Concentration .....	30
14	Elemental Composition of Film with 11% Hydrogen .....	31
15	Optical Image of Sample No. 645 Si .....	32
16	Optical Image of Sample No. 633 Al <sub>2</sub> O <sub>3</sub> .....	32
17	Optical Image of Sample No. 646 CrAlSi .....	33
18	RBS Spectrum from Sample No. 491 Using Silicon Substrate .....	34
19	RBS Data from Sample No. 505 with Glassy-Carbon Substrate .....	36

**List of Figures (Continued)**

<b><u>Figure</u></b>		<b><u>Page</u></b>
20	XPS Spectrum of Glassy-Carbon Substrate .....	36
21	XPS Spectrum of Sample No. 487 Prior to Sputter Cleaning Top Surface Layer .....	37
22	XPS Spectrum of Sample No. 487 after Sputter Cleaning for 10 min .....	38
23	RBS Data from Sample No. 456 .....	39
24	RBS Data from Sample No. 515, Demonstrating a Thick Film .....	40
25	RBS Spectrum of Sample No. 487 .....	40
26	RBS Data from Sample No. 517, Demonstrating a Thin Film .....	41
27	Nitrogen Concentration in Films as Function of Input Gas Mixture for Three Ion-Source Operating Conditions .....	42
28	Hydrogen Concentration as Function of Input Gas Mixture and Three Ion-Source Operating Conditions .....	43
29	Density of Films as Function of Input Gas Mixture for Three Ion-Source Operating Conditions .....	44
30	Elemental Composition for Each Run Condition .....	45
31	Elemental-Composition Ratios for Each Run Condition .....	46
32	Three-Axis Compositional Phase Diagram Showing Experimental Results Ranging from DLC to Recently Formed CN <sub>x</sub> .....	48
33	XRD Data for Sample No. 40210616 on Quartz Substrate .....	49
34	FTIR Spectrum of NaCl Salt Crystal and CN <sub>x</sub> Film Deposited on NaCl .....	50
35	FTIR Spectra of Run Nos. 602, 612, 615, 617, and 618 .....	51
36	Zoomed-In View of FTIR Spectra for Run Nos. 602, 612, 615, 617, and 618 .....	52

**List of Figures (Continued)**

<b><u>Figure</u></b>		<b><u>Page</u></b>
37	UV-Visible Optical Band-Gap Data as Function of Nitrogen-to-Hydrogen Ratio .....	57
38	Median $D_f$ Values for Various Substrate Materials .....	59
39	Capacitor Pads with $D_f$ Values Less Than 1.0 .....	60
40	Highest Resistivities Achieved under Each Run Condition .....	62
41	Voltage-Breakdown Graph .....	64
42	Sample Displaying Linear I-V Curve--Characteristic of Resistor .....	65
43	Sample Demonstrating Plateau in Breakdown, Indicating Possible Clearing Effect .....	65
44	Values of $\epsilon_r$ for Each Sample Condition and Substrate Type .....	67

## List of Tables

<b><u>Table</u></b>		<b><u>Page</u></b>
1	Material Properties .....	4
2	Vickers Hardness .....	14
3	Wear Track Depth .....	15
4	Corrosion Test Data .....	16
5	Compositional Summary for CN <sub>x</sub> Deposition .....	47
6	Run Parameters for Mass-Spectrum Graph .....	52
7	Optical Band-Gap Measurements .....	53
8	Optical Band Gap for Common Materials .....	53
9	Hydrogen Concentrations and Properties of Select CN <sub>x</sub> Depositions .....	56
10	Dissipation-Factor Summary .....	59
11	Electrical Summary of CN <sub>x</sub> Capacitors .....	72
12	Optical-Imaging Summary .....	75
13	RBS and ERS Summary .....	78
14	Electrical Summary for Single-Ion-Beam CN <sub>x</sub> Depositon .....	82

## PREFACE

This final report for the program entitled, "Research on Nitride Thin Films, Advanced Plasma Diagnostics, And Charged-Particle Processes," was developed under AFOSR Contract No. F33615-00-C-2055. Innovative Scientific Solutions, Inc. (ISSI) provided the expertise for this program, which was performed for the Air Force Research Laboratory at the Wright Site Laboratory at Wright-Patterson AFB, Ohio. This program was divided into three sub-tasks: 1) Nitride Thin Film Coatings, 2) Advanced Plasma Diagnostics, and 3) Charged-Particle Processes. Ohio University, operating on a sub-contractual basis for Task 1, performed compositional analysis on various carbon-nitride films using Rutherford-Backscattering Spectroscopy and Elastic-Recoil Spectroscopy. The final report for the Ohio University subcontractual effort can be found in the Appendix.

The objective of Task 1 was to perform research on single- and dual-ion-beam sputtered carbon, for the purpose of creating carbon-nitride films and to gain an understanding of the fundamental ion-beam-deposition parameters while optimizing the deposition-process conditions and the resulting films. In Task 2, advanced diagnostics of plasmas under various operating conditions were performed to gain a better understanding of the generated plasma fields. Task 3 utilized Fourier Transform Mass Spectrometry (FTMS) to analyze charged-particle reactions.

As a result of the work performed during this program, several manuscripts were published in journals and professional proceedings, and presentations were given at professional meetings. This contract also provided support for three years to Asghar Kayani, a graduate student with Ohio University, who received his Ph.D in 2004; his thesis was entitled "Deposition and Characterization of Diamond-Like Films with and without Hydrogen and Nitrogen."

The authors would like to thank Drs. Charles DeJoseph and Susan Heidger of the Air Force Research Laboratory for their technical discussions and guidance, Dr. David C. Ingram of Ohio University for sample compositional analysis and guidance, and Dr. Bang Tsao and Mr. Vic McNier of the University of Dayton Research Institute for their assistance with metal depositions and electrical characterizations.

Dr. Larry Goss was the ISSI Program Manager for this effort. Mr. William C. Lanter was the Principal Investigator for Task 1, with assistance from Mr. B. Allen Tolson and guidance from Dr. David Ingram of Ohio University. Dr. Wei Guo was the initial Principal Investigator for Task 2, and Mr. B. Allen Tolson followed as a Support Technician for daily operations. Dr. Charles Jiao was the Principal Investigator for Task 3.

## SUMMARY

A large-area deposition system developed under a previous contract,<sup>1</sup> consisting of a 20-cm 13.56-MHz radio-frequency (rf) inductivity coupled ion gun and a four-axis substrate scanner, was modified with the addition of a 3-cm Kaufman ion gun and utilized to conduct carbon-nitride film depositions. Carbon-nitride films were deposited onto various substrates: silicon, glassy carbon, aluminum-coated silicon, nickel-coated silicon, chromium-coated silicon, 7059 corning glass, quartz, sodium-chloride salt crystal, carbon composite, Fluorinated Polyester (FPE) polymer, 440C steel, and 316 stainless steel. FPE was utilized in a joint effort to develop a transparent oxygen barrier for flexible flat-panel displays. 440C steel and 316 stainless steel were coated in a collaborative effort for friction and wear testing. Carbon composite samples were coated in collaboration with the Materials Directorate of AFRL to provide a protective filler coating for eliminating lubrication uptake into composites used for high-speed bearing races in turbine engines. The metal-coated and silicon samples were utilized for the development of capacitors. Remaining samples were utilized for various film characterizations.

Amorphous carbon-nitride (CN<sub>x</sub>) samples were developed and tested for composition, thermal stability, thermal conductivity, IR transmission, and electrical properties such as dielectric constant, resistivity, breakdown strength, and dissipation factor. Thermal stability was shown to be the best attribute. Low-hydrogen-concentration CN<sub>x</sub> samples remain thermally stable with no compositional degradation up to 600°C and remain intact with no evidence of spallation, cracking, or peeling up to 900°C. Films with higher concentrations of hydrogen remain stable up to 400°C prior to compositional degradation. Electrical properties have improved, but additional research is required before the material can become useful. Films with measured dissipation factor of 0.1 - 0.02 can be produced consistently. These values are higher than desired but are within an acceptable starting range. The highest breakdown voltage achieved was 393 kV/mm, and the dielectric constant for acceptable capacitors ranges from 1.9 to 12. The thermal conductivity is undetermined at this point. Measurements were conducted but exceeded the sensitivity of the equipment used. Thicker films must be developed for accurate thermal measurements. Infra-red (IR) transmission of CN<sub>x</sub> on a salt crystal showed negligible absorption in the measured range of 700 to 4000 wavenumbers. Hardness along with friction and wear measurements were not performed; however, experience with the film and literature searches indicate that CN<sub>x</sub> films adhere better and are significantly harder than comparable diamond-like-carbon (DLC) films.

The most notable problematic characteristic of CN<sub>x</sub> films is resistivity. Values up to 10<sup>12</sup> Ω-cm were measured. However, a significant portion of the films exhibited relatively low resistivity values. With varying results from run to run, the precise growth parameters required for successful development of CN<sub>x</sub> films remain unknown. It is anticipated that further study into the microstructure and morphology of the film in conjunction with electrical testing under various growth conditions is required to gain a better understanding of the growth parameters. All of the CN<sub>x</sub> film results to date indicate that successful development of this film will result in a film with properties superior to those of DLC films.

---

<sup>1</sup>R.L.C. Wu and W.C. Lanter, "Apparatus Modification for Large Area Surface Treatment," Final Report No. WL-TR-95-2106 (1995).

The plasma-diagnostics chamber was modified to increase the amount of energy used for creation of plasmas. This also increased the pressure ranges for which the plasma could be created and extended the plasma-characterization range.

Modifications involved conversion of the original rf power supply and matching network to a higher powered, pulsed, rf power supply. The associated rf matching network with the new power supply had to be custom fitted to the existing plasma discharge chamber. Modifications were also performed on the Langmuir probe tip to enhance measurements.

The Fourier Transform Mass Spectrometer (FTMS) was utilized to study ion chemistries in compounds including gases relevant to plasma etching processes such as  $\text{CF}_3\text{Br}$ ,  $\text{CF}_3\text{I}$ ,  $\text{NO}_2$ ,  $\text{CH}_3\text{NO}_2$ ,  $l\text{-C}_4\text{F}_8$ , and  $c\text{-C}_5\text{F}_8$ , gases relevant to plasma enhanced chemical vapor deposition such as diethylzinc  $\text{Zn}(\text{C}_2\text{H}_5)_2$  and hexamethyldisiloxane ( $\text{Si}_2\text{OC}_6\text{H}_{18}$ ), and gases relevant to combustion such as  $n\text{-C}_8\text{H}_{18}$ ,  $n\text{-C}_{10}\text{H}_{22}$ ,  $\text{C}_{10}\text{H}_8$  (naphthalene),  $\text{C}_6\text{H}_6$  (benzene), Quadricyclane ( $\text{C}_7\text{H}_8$ ), JP-10 ( $\text{C}_{10}\text{H}_{16}$ , tetrahydrodicyclopentadiene), and  $n\text{-C}_4\text{H}_{10}$ . A study on pyridine ( $\text{C}_5\text{H}_5\text{N}$ ) was also carried out in collaboration with a research group at NASA that recently performed theoretical calculations on the ionization cross sections of benzene and pyridine as part of a program to investigate the role played by electron-impact dissociative ionization in the processes of DNA damage by space radiation.

# **TASK 1. CARBON-NITRIDE THIN-FILM COATINGS**

## **1.0 INTRODUCTION**

Discrete electrical components that are capable of storing greater amounts of energy while being subjected to rapid power extraction are in demand. Additionally, these components are being placed closer to the point of use--requiring that they operate in extreme temperature environments. Concurrently, it is preferred that these components weigh less and occupy less physical space than devices presently available. These requirements result in electronics and associated components which operate in temperature ranges that cause failure with standard devices.

Heat is one of the main reasons for component failure. To operate in extreme temperature environments, electronic and electrical components must withstand higher ambient temperatures without loss of integrity or decomposition of the device. Another major concern is internal thermal gradients that create localized hot spots, which may exceed the temperature rating and weaken the mechanical integrity of the device. Thus, it is vital that a uniform temperature be maintained throughout the device.

The high-energy-density capacitor is one type of discrete electrical component that is vital for the mission of the Air Force with regard to developing advanced directed-energy weapons such as airborne lasers and high-pulse-power microwaves. Increasing the specific energy density of a capacitor enables it to store a greater amount of power. This will result in more powerful weapons, with a reduction in the amount of time-on-target required for destruction and an increase in the range; this will allow the target to be engaged from greater distances and reduce the vulnerability of delivery systems.

Portability is another critical issue for the Air Force. Replacing mechanical systems with point-of-use electrical systems will reduce the quantity of mechanical components and, in turn, the weight of an entire system, thus increasing portability. Portability can be further improved by reducing the weight and size of electronic components within point-of-use electrical systems. Weight and size reductions of system components benefit space-based systems and airborne weapons by increasing payload capability or weapon lethality. A concurrent weight and size reduction in system delivery components allows a comparable increase in the power components required for advanced directed-energy weapons such as airborne lasers and high-pulse-power microwaves.

In the commercial sector, high-power high-energy-storage devices used in hybrid and plug-in hybrid-powered automobiles, heart defibrillators, and industrial equipment will benefit from a new generation of capacitors. High-temperature electronic components are needed in conventional as well as hybrid-powered automobiles, where point-of-use electronics adjacent to the engine are subjected to conditions of extreme heat. Likewise, large current draws in hybrid-powered automobiles generate excessive heat levels--the leading cause of failure for many electronic sub-systems.

For these systems portable, high-temperature, high-energy-storage power and electronic devices are needed. For smaller, lightweight packages, advanced electronic components that meet these stringent new requirements are not presently available. These components must also be capable of withstanding higher voltages and temperatures to allow high-energy-density storage and rapid power extraction.

All of these electronic packages have a common weak link--the capacitor. Capacitors are extremely large in comparison with other electronics because of the area required to store power and the inherent weakness of the insulating material, or dielectric, required to provide separation and insulation. Common power capacitors currently in use have a maximum operating temperature of 125°C (257°F). Recent research has resulted in the development of amorphous carbon-nitride (a-CN<sub>x</sub>, or simply CN<sub>x</sub>) for use as a high-temperature dielectric that is suitable for construction of small, lightweight capacitors. This material has been theoretically determined to have a low dielectric constant. Measured resistivity is presently as high as  $1 \times 10^{12} \Omega\text{-cm}$ , and thermal stability with no degradation of the film is at a maximum of 600°C (1112°F), which is ideal for high-temperature, high-energy storage applications. Although elemental degradation occurs at temperatures in excess of 600°C, no evidence of spallation, peeling, or cracking of the film up to 900°C (1652°F) was found.

For size reduction a dielectric material requires a higher dielectric constant or higher energy-density that is achieved with higher voltage breakdown strength. However, materials with a high dielectric constant tend to have lower voltage-breakdown strength than those with a low dielectric constant.<sup>2</sup> Therefore, a suitable dielectric must display characteristics of high voltage-breakdown strength, thermal conductivity, and resistivity along with a low dielectric constant and dissipation factor.

Liu and Cohen<sup>3,4,5</sup> theoretically determined carbon nitride ( $\beta\text{-C}_3\text{N}_4$ ) to be a material that is harder than diamond. It is calculated to be a wide-band-gap material<sup>4</sup> with properties similar to those of diamond. Based on this, various research efforts have been concentrated on growing crystalline  $\beta\text{-C}_3\text{N}_4$ ; however, very little success has been achieved. Muhl and Méndez reviewed research involving attempts at crystalline growth.<sup>6</sup> Amorphous forms of carbon and nitrogen (CN<sub>x</sub>) with varying types of bonding and compositional ratios are grown with relative ease, but high nitrogen concentrations are difficult to achieve. These various forms of amorphous carbon and carbon nitride range from conductive hard carbons to electrically insulating diamond-like carbon (DLC). From the similarities found in comparing DLC and diamond, it is anticipated that an amorphous form of CN<sub>x</sub> can be produced that will display properties similar to those theoretically determined for  $\beta\text{-C}_3\text{N}_4$ .

---

<sup>2</sup>M. Rabuffi, G. Picci, "Status Quo and Future Prospects for Metallized Polypropylene Energy Storage Capacitors," IEEE Trans. Plasma Sci. 30 (2002) 1939.

<sup>3</sup>M. L. Cohen, Phys. Rev. B 32 (1985) 7988.

<sup>4</sup>A. Y. Liu, M. L. Cohen, "Prediction of New Low Compressibility Solids," Science 245 (1989) 841.

<sup>5</sup>A. Y. Liu, M. L. Cohen, "Structural Properties and Electronic Structure of Low-Compressibility Materials:  $\beta\text{-C}_3\text{N}_4$ ," Phys. Rev. B 41 (1990) 10727.

<sup>6</sup>S. Muhl, J. M Méndez, Diam. Rel. Mat. 8 (1999) 1809-1830.

Numerous studies of amorphous  $CN_x$  have been conducted with varying compositions of hydrogen, carbon, and nitrogen. Most of these studies report on tribological properties, with only a few reporting on electrical properties.<sup>7,8,9,10,11</sup> In these papers electrical properties range from conductive<sup>9</sup> to highly resistive.<sup>7</sup> It is suspected that this lack of electrical data and the conflicting results are due to difficulties involved in incorporating high concentrations of nitrogen into the film.

The focus of this program was to develop amorphous carbon nitride films utilizing controlled plasma-generated ions to increase the nitrogen concentration within the film. It is anticipated that development of films with higher concentrations of nitrogen will lead to properties similar to those theoretically calculated for crystalline  $\beta-C_3N_4$ .

The pursuit in the development of amorphous  $CN_x$  lies in the need for a smooth, highly thermally conductive and electrically insulating thin film. Table 1 on the following page summarizes various properties, comparing diamond, DLC,  $CN_x$ , and a commonly used dielectric, silicon dioxide ( $SiO_2$ ). A review of these properties shows that diamond displays all of the desired properties required from high-performance, high-temperature electronics. The current problems with this material are the extremely high temperatures needed to create it (600 - 900°C), rigidity, and the inability to create large-area single crystals needed to provide smooth surfaces for further development of electronic devices. DLC has been developed to the point where it is now relatively easy to create, and it exhibits most properties similar to diamond. Its added features are that it can be synthesized at near room temperatures and that it is smooth.  $SiO_2$  is a common material that is currently in use in electronics. Most of its properties are desirable, and it is extremely easy to synthesize. However, the greatest drawback for this material is that its thermal conductivity is extremely low compared to that of the other materials. This limitation is a major factor in failures in electronic devices due to heat buildup. Carbon nitride shows promise since its properties are similar to those of diamond, much like DLC. Its largest advantage over DLC, however, is the theoretical anticipation for its increased thermal conductivity and its proven superiority in thermal stability, listed as the max use temperature.

Advanced capacitors currently under study employ DLC or fluorine polyester (FPE). These materials can operate at temperatures up to 200°C (392°F) and 250°C (482°F), respectively. In DLC the film-composition range is around 60% carbon and 40% hydrogen. Hydrogen is easily incorporated during deposition, and prevention of its incorporation during film growth is extremely difficult. This is a disadvantage since hydrogen is easily liberated at elevated temperatures--thus, the maximum use temperature of 200°C (392°F) for DLC. While this represents an improvement over current technology, these temperatures still can be easily

---

<sup>7</sup>M. Aono, S. Nitta, "High Resistivity and Low Dielectric Constant Amorphous Carbon Nitride Films: Application to Low-k Materials for ULSI," *Diam. Rel. Mat.* 11 (2002) 1219-1222.

<sup>8</sup>M. A. Monclus, D. C. Cameron, A. K. M. S. Chowdhury, *Thin Solid Films* 341 (1999) 94-100.

<sup>9</sup>E. Broitman, N. Hellgren, K. Järrendahl, M. P. Johanson, S. Olafsson, J.-E. Sungren, L. Hultman, "Electrical and Optical Properties of  $CN_x$  ( $0 \leq x \leq 0.25$ ) Films Deposited by Reactive Magnetron Sputtering," *J. Appl. Phys.* 89(2) (2001) 1184-1190.

<sup>10</sup>J. Wei, "Electrical Properties of Reactively-Sputtered Hydrogenated Carbon Nitride Films," *Int. J. Nanosc.* 3(4/5) (2004) 555-562.

<sup>11</sup>Y. Aoi, K. Ono, K. Sakurada, E. Kamijo, *Mat. Res. Soc. Symp. Proc.* 750 (2003) 285-290.

exceeded with high-current-draw applications.

It is anticipated that successful development of amorphous  $CN_x$  will lead to replacement of current state-of-the-art DLC films. This will result in improved films with feature qualities such as better adhesion, reduced friction, increased wear life, higher thermal stability, improved thermal conductivity, higher voltage-breakdown strengths, and increased energy densities.

Potential benefits of this development for military applications are 1) robust, high-temperature capacitors for more electric aircraft (MEA), satellites, and planetary robots, 2) improved capacitors for energy storage and rapid power draw for hybrid-powered or future electric-powered vehicles, 3) smaller, lighter capacitors with energy storage equivalent to that of larger capacitors developed using current technology--which can be used for smaller, more portable systems and equipment, 4) solid lubricants for harsh environments, 5) reduction in friction and wear on rolling or sliding surfaces, and 6) improved hard coatings for protection of IR windows.

In the commercial sector high-power, high-energy-storage devices used in hybrid and plug-in hybrid-powered automobiles, heart defibrillators, and industrial equipment will benefit from a new generation of capacitors. High-temperature electronic components are needed in conventional as well as hybrid-powered automobiles, where point-of-use electronics adjacent to the engine are subjected to conditions of extreme heat. Likewise, large current draws in hybrid-powered automobiles generate excessive heat levels. High heat levels are the leading cause of failure for many electronic sub-systems.

**Table 1. Material Properties**

	<b>Diamond (Thin Film)</b>	<b>DLC</b>	<b><math>CN_x</math> (Thin Film)</b>	<b><math>SiO_2</math></b>
<b>Electrical Properties</b>				
<b>Dielectric Constant</b>	3.5 - 5.7	2 - 3.5	1.5 - 5*	3.8 - 3.9
<b>Dielectric Strength (kV/mm)</b>	1000	100-200	50-400*	4 - 50
<b>Dissipation Factor</b>	0.014-0.0002	0.1 - 0.001	0.02*	0.0001
<b>Band Gap (eV)</b>	5.2 - 6.4	0.1 - 4	0.9 - 3.8*	8.9
<b>Electrical Resistivity (<math>\Omega</math>-cm)</b>	$>10^{14}$	$10^6 - 10^{12}$	$10^5 - 10^{14}$ *	$10^{12} - 10^{16}$
<b>Thermal Properties</b>				
<b>Thermal Conductivity (W/m-K)</b>	2400	50 - 180	100 - 250 <sup>?</sup>	1.4 - 2.0
<b>Max Use Temperature (<math>^{\circ}</math>C)</b>	800	300	600*	1100

\*Experimental Values

<sup>?</sup>Theoretically Determined Values

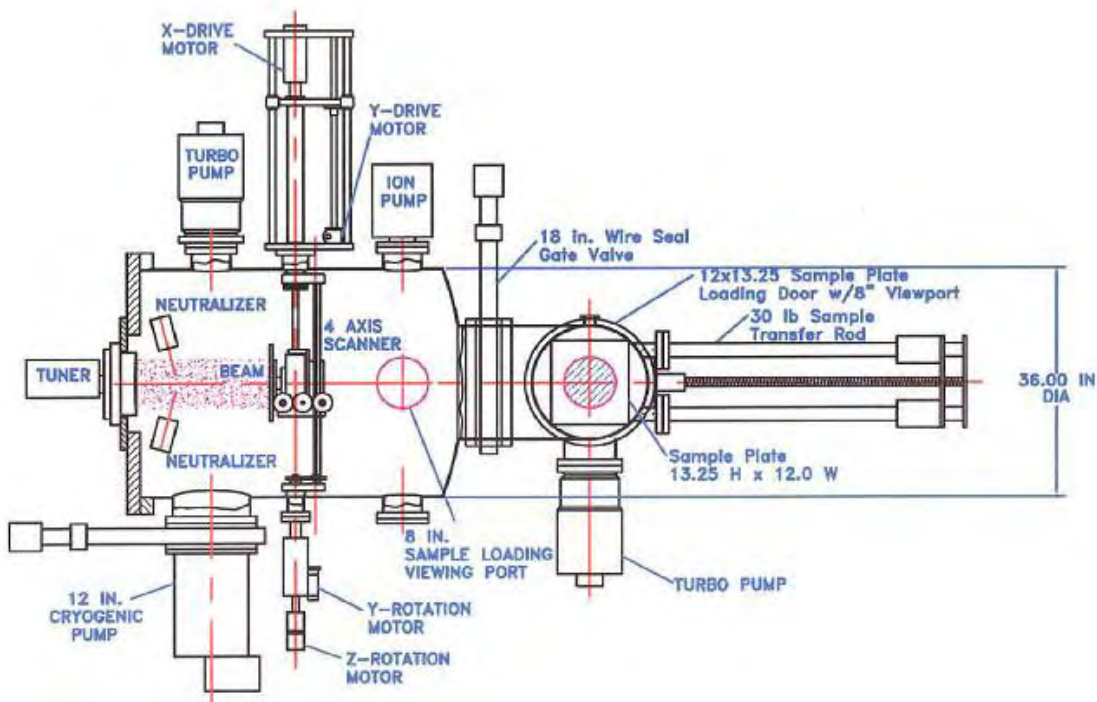


**Figure 1. Schematic of LADS.**

## 2.0 EXPERIMENTAL EQUIPMENT

### 2.1 Large-Area-Deposition System (LADS)

Figure 1 is a schematic of LADS, which was set up as a dual ion-beam-assisted, ion-beam-sputter deposition system. LADS is a 900-l ultra-high-vacuum (UHV) chamber with a 1000 cm<sup>2</sup> water-cooled sample-deposition area that is capable of achieving  $2.6 \times 10^{-6}$  Pa ( $2 \times 10^{-8}$  torr) background pressures. The system is pumped using a 3000-l/s cryogenic pump and a 1000-l/s turbo pump that is backed with a 600-l/s dry-scroll rough pump; the result is a completely oil-free vacuum system. The sample-deposition plate is mounted to a scanner with four degrees of motion: X, Y,  $\theta Y$ , and  $\theta Z$ . The water-cooled substrate holder can be maintained in a temperature range 5 - 35°C. Figure 1 details the system arrangement. An additional sample heater can heat samples up to 1000°C. Three internally mounted quartz lamps can also be utilized to heat the sample surface and for internal heating of the chamber for outgassing. A 20-cm, 13.56-MHz RF ion source is employed for broad-beam-assisted deposition of nitrogen, while a second (3-cm Kaufman) ion source utilizes nitrogen to sputter carbon from a carbon target; both concurrently deposit onto the sample target. These sources are fed with a seven-channel gas manifold. Four channels are combined into a mixing chamber and fed to the 20-cm rf ion source. Two additional channels are combined and fed to the 3-cm Kaufman ion source. The final channel is fed to two hollow-cathode neutralizers. Two off-axis quadrupole mass spectrometers are utilized to monitor chamber background prior to deposition and ionic species generated during film deposition. A computer-based data-acquisition system controls the

chamber system operations and performs data logging during deposition. Detailed descriptions can be found in previous reports.<sup>1,12</sup>

### **2.1.1 Equipment Modifications**

Several equipment modifications and updates were performed throughout the program when equipment failed or as necessitated for conducting the experiments.

#### ***2.1.1.1 Scroll Pump***

The original rough pump on LADS was a DS600 Dry Scroll rough pump from Varian Vacuum Products. Design issues with this pump cause moisture condensation from atmospheric pump-downs in the center shaft and bearings of the pump. This leads to premature failure due to rusting and accumulation of particulates pumped during film processing. To solve these problems, the pump head was reoriented so that the central port exhausted downward, allowing drainage of accumulated water. To improve exhaust velocities and eliminate particulate flow restrictions, the exhaust filter was removed. To minimize the number of particulates (created from the deposition process) entering the rough pump, a stainless steel mesh canister filter was installed on the inlet side of the pump.

A new Tri-scroll rough pump was ordered from Varian Vacuum Products. This pump was redesigned to eliminate the pump problems mentioned above. The pump was attached to the main deposition chamber, while the DS600 Dry Scroll pump was used as an assist through the load-lock chamber.

#### ***2.1.1.2 Turbo Pump***

Bearings on the main-chamber turbo pump, Varian Turbo-V1000A, failed; this resulted in a catastrophic failure that destroyed the turbine blades. A new turbo pump (macro-torr TV1001 Navigator) and corresponding controller (Turbo-V 1000HT) were installed.

#### ***2.1.1.3 Cryo-Pump***

The original CTI Helix Cryo-Pump mounted on the main deposition chamber developed a leak in the cryo-head. This head assembly was exchanged for a new head unit. Concurrently, the old helium-pump compressor was replaced with a new unit, Model 9600, to minimize further failures due to age or contamination. With the exchange of both the turbo pump and the cryo-pump, the LADS system was now able to achieve a background vacuum less than  $5 \times 10^{-8}$  torr, compared to vacuums of  $2 \times 10^{-6}$  torr prior to the pumps being replaced.

---

<sup>12</sup>R.L.C. Wu, W Guo, and W.C. Lanter, "Large Area Ion Beam Deposition of Diamond-Like Thin Films," Final Report No. AFRL-PR-WP-TR-1999-2082 (1999).

#### ***2.1.1.4 Water Recirculator***

The Neslab System II water recirculator utilized to cool LADS components experienced numerous pump and heat-exchanger coil failures due to building water. These persistent failures created numerous film-deposition delays. A new Tek-Temp NRD550 water recirculator was purchased, which has a maximum cooling capacity of 130,000 BTU/hr, flowing system water up to 6.5 gal/min at 40 psi.

#### ***2.1.1.5 Water Manifold***

The water-flow switches on the water manifold were corroded, and some were not functioning at the appropriate water-flow settings. The corrosion is due to de-ionized recirculated water aggressively attacking the brass switches. The switches were replaced with stainless steel Gems flow switches to prevent future problems, and the de-ionized, distilled recirculating water was replaced with spring water.

Water lines to the ion source from the manifold were changed from 1/4 in. to 3/8 in. lines to reduce the pressure drop in the lines and increase water flow. The flow switches were replaced with a 0.25-gpm switch for the 20-cm ion gun and 0.5-gpm switches for the turbo pumps.

#### ***2.1.1.6 Gas Flow Controller***

The original gas monitor for LADS was the MKS 647A gas-flow-controller power supply. Although the CPU and monitor were functioning, the backplane for the system failed, preventing communications with the data-acquisition system. This power supply and monitor unit, along with the associated gas-flow controllers, were replaced with Celerity (Unit Instruments) flow meters, Model 7361. A total of seven flow meters was purchased--three with a 50-sccm N<sub>2</sub> full-scale range, two with a 100-sccm N<sub>2</sub> full-scale range, and two with a 150-sccm N<sub>2</sub> full-scale range. These units can be re-programmed for full scale ranges down to one-third of their original full-scale range. The meters are computer controlled through RS-485 communications, can be controlled either by digital or analog means, and have viton seals on metal seats. These flow meters are more reliable and stable than the MKS flow meters. Additionally, up to 99 flow meters can be controlled via the same daisy-chained RS-485 connection. A ±15-V power supply was also purchased to power the flow meters. An RS-485 power signal booster was purchased, which was needed to drive more than three devices at a time.

#### ***2.1.1.7 Gas Manifold***

The original gas manifold contained five MKS flow controllers. The new purchase of seven Unit flow controllers necessitated the construction of a new gas flow control panel. The system is now capable of maintaining four independent gas flows to the 20-cm ion-source, two independent gas flows to the 3-cm ion source, and one gas source to the two ion-beam neutralizers.

### 2.1.1.8 20-cm Ion Source

#### *Grids*

Grids on 20 cm ion source are a consumable item that is replaced approximately on an annual basis. The original ion source manufacturer, Nordiko, was prohibitively expensive. CAD drawings, created in-house, are on file with Minteq International. This graphite manufacturer produces the grids for both the 20-cm and the 3-cm ion source for approximately one-third the cost of the OEM manufacturers.

#### *Quartz Window*

Quartz windows for the 20-cm ion source are another consumable item. An original window was sent to Scientific Glass of Florida (SGF) for manufacture of replacement windows. SGF, compared to OEM, was able to manufacture the windows at a significant cost reduction--a cost of \$525.00 versus \$5000.00 per window.

The new deposition process that utilized nitrogen in the 20-cm ion source appeared to be causing rapid erosion in the center of the rf quartz window, possibly due to the new gas mixtures with nitrogen, which may have been much more reactive to quartz. It is also possible that the rf field concentration with this new gas mixture is extremely strong in the central region.

To eliminate this problem, the rf coil was expanded by uncoiling it one full revolution, increasing its contact area across the window. The quartz window was modified by adding an additional 3/8 in. button of quartz to the exterior portion of the window and a 3/8-in. cone of quartz to the interior portion of the window. Figure 2 is a schematic of the changes.

Unfortunately, the modifications to the quartz windows induced stresses into them. The stresses were relieved by performing two anneals at 900°C--one with the window facing up and the second with the window facing down in the furnace. Anneals were performed in a standard lab-air environment.

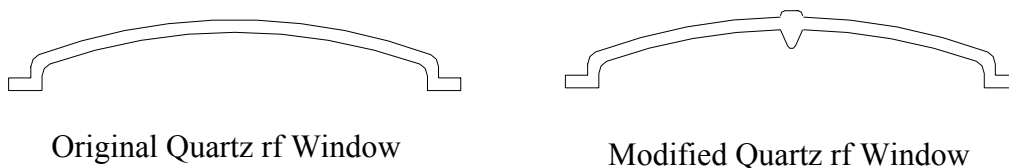


**Figure 2. Quartz rf Window.**

### 2.1.1.9 3-cm Ion Source

A 3-cm Kaufman ion source was installed into LADS for performing ion-beam sputter depositions. This ion source was originally built by Commonwealth Scientific, which has since been purchased by Veeco Vacuum Products. Further detailed discussions on the 3-cm ion source setup can be found in the Experimental Setup Section.

Power feed cables to the ion source had to be extended and modified to accommodate the distance required within the deposition system and to reduce arcing and erosion to the cables during plasma deposition. Ceramic fishbowl beads were added to each cable with a stainless steel ground shield. The entire wire harness was then encased into a flexible ceramic jacket.

Several supporting brackets were added internally to the chamber to support the 3-cm ion source as well as the 6-in. sputter target.

#### ***2.1.1.10 Sample Heater***

A sample heater was designed and developed to perform elevated-temperature depositions. The heater uses a boron-nitride electric resistive heater and can achieve temperatures up to 1000°C. Heat shields surround the heater for minimizing heat radiation to other components. Ceramic standoffs mount the heater to the sample cooling plate that is located on the four-axis scanner. The sample heater was fabricated at Ohio University and pre-tested to verify power-versus-temperature requirements. A power feedthrough was purchased to feed power through the chamber to the heater. A variac provides power to the heater.

#### ***2.1.1.11 Quartz Lamps***

Three 500-W quartz lamps were added to the system to provide front-surface heating of the samples and to assist with water bake-out during background vacuum pumping. These lamps are very effective at instantly heating of the internal chamber walls, as evidenced by residual gas analysis (RGA) and ionization pressure measurements.

#### ***2.1.1.12 Mass Spectrometers***

An Ametek/Dycor quadrupole mass spectrometer is attached to LADS, located 90° off of the 20-cm ion-gun beam axis. The linear operating range for this system is at pressures less than  $5 \times 10^{-5}$  torr. This system provides a high degree of sensitivity for hydrogen and can scan masses up to 200 amu.

To upgrade the system, an additional mass spectrometer was ordered from Hiden Analytical Instruments. The Hiden HMT 100 RC High Pressure RGA System is an open-source, non-differentially pumped quadrupole mass spectrometer that is capable of functioning linearly at pressures up to  $1 \times 10^{-3}$  torr while providing high mass resolution and high sensitivity for hydrogen and masses up to 100 amu.

#### ***2.1.1.13 Computer System***

LADS is partially controlled by means of a data-acquisition computer system (DAC). This system was developed slowly as the program evolved. Programming was performed utilizing National Instruments LabView software. The data-acquisition board (DAQ) was a PCI slot board, mounted internally to the computer, and was attached to external break-out boards for

data transfer and control. An opto-isolation interface was developed to provide voltage and noise protection due to LADS operating environment. Likewise, an interlock control panel was developed to control gas flow and to monitor critical system components for failure. System components designed with RS-232 communications were also controlled through the use of LabView software. An Octi-eight serial card was installed to provide an additional eight serial ports for communication. Windows XP Pro was used for the computer operating system.

#### ***2.1.1.14 Auxiliary Test Equipment***

##### ***Fourier Transform Infrared Spectrometer (FTIR)***

An FTIR available within the laboratory that contains LADS was utilized to characterize the amount of total IR absorption as well as the various absorption bands associated with elemental bonding within the film.

A water flow switch was designed to turn off power to the FTIR if the water should stop flowing. This was done to prevent overheating of the internal IR lamp. This IR lamp is a consumable item; the IR signal emitted decreases over time. As the signal decreases, measurement of opaque samples such as silicon becomes difficult. A new HeNe laser was installed and the system calibrated by a Thermo-Mattson Field Engineer. The laser provided precise measurement for the interferometer during operation.

##### ***Step Profilometer***

A Dektak step-profilometer was utilized to perform post-deposition thin-film-thickness measurements. This equipment is located in Building 18, Room 35, at Wright-Patterson AFB.

##### ***Capacitance Tester***

An LCR HP4284A capacitance meter with Signatone micropositioner probes, M/N S-725, was used to measure through-the-film capacitance and the dissipation factor ( $D_f$ ) [loss tangent ( $\delta$ )] of developed capacitors as a function of frequency. This equipment is located in Building 18B, Room 13.

##### ***Voltage-Breakdown/Insulation-Resistance Tester***

.For samples with acceptable  $D_f$  values, a Keithley 6517A high-resistance meter was used for D.C. resistance ( $R_{ir}$ ) and breakdown insulation resistance measurements ( $V_b$ ). This equipment is located in Building 18B, Room 13.

##### ***Dual rf Magnetron Sputtering System***

A dual-head, rf magnetron sputtering system was utilized to develop bottom and top electrodes for capacitor plates. This equipment is located in Building 18B, Room 13.

### *Optical Microscope*

An optical microscope was used for visual inspection of the surface of deposited films to determine the number of pinholes and macroscopic particles embedded within the film. This equipment is located in Building 18B, Room 13.

### *Rutherford Backscattering Spectroscopy (RBS) and Elastic Recoil Spectroscopy (ERS)*

RBS and ERS were performed on heat-treated as well as room-temperature (non-heat-treated) glassy-carbon and silicon samples. RBS was used to measure the elemental composition of heavier elements within the films, and ERS was employed to determine the hydrogen elemental content in the films. RBS was performed with 2.2-MeV alpha particles scattered through 168° to avoid problems due to non-Rutherford scattering from carbon and nitrogen that would occur above that energy. ERS was also performed with 2.2-MeV alpha particles. Recoiled protons were detected with a solid-state barrier detector set at 30° to the beam. A 13- $\mu\text{m}$  Mylar foil was used to prevent forward-scattered alpha particles from reaching the detector. The cross section used to determine the hydrogen concentration from the ERS data was that of Keay and Ingram.<sup>13</sup> This equipment is located at Ohio University, within the Edwards Accelerator Laboratory.

### *Quartz-Tube Furnace*

Two quartz-tube furnaces were available for use--one located at Ohio University within the Edwards Accelerator Laboratory and one at Building 18, Room 35. The tube furnace was utilized to anneal samples at elevated temperatures in a controlled environment.

### *Scanning Electron Microscope (SEM)*

An SEM located at Ohio University and one located in Building 18, room 35 where utilized to visualize microstructure features of the deposited film surfaces and cross-sectional view.

## **3.0 COLLABORATIVE RESEARCH**

This testing was exploratory in nature, and complete and thorough testing was not performed. Additionally, these tests were performed at the beginning of this program when  $\text{CN}_x$  film development methods had just begun. Further testing in these areas is required if current and accurate results are to be provided.

### **3.1 Arylite Polymer**

Arylite Polymer (commercial name for FPE) was coated through a collaborative research effort with Wright Technology Network. The intent was to use FPE film on a flexible printed circuit display. However, the film is oxygen permeable, which leads to degradation of the printed circuitry. Therefore, the objective was to apply to the polymer with DLC and nitrided-DLC a clear coating that would prevent oxygen permeation. Figure 3 is a photograph of the film

---

<sup>13</sup>J.C. Keay and D.C. Ingram, Nuc. Instr. and Meth. Phys. Res. B 211, (2003) 305.

depositions on the Arylite polymer displayed adjacent to a non-coated portion of the polymer for color-variance comparisons. The coatings are DLC, N-DLC, and O-DLC.

Initially, Sample No. 525 was created using fairly standard run parameters, with a hydrogen pre-cleaning run of 12 min and run duration of 10 min. These parameters should have created a film approximately 300 Å, which was expected to be fairly clear. However, this film was one of the darkest films in the series. The parameters were slightly altered for Run Nos. 526 and 527, and the duration of the runs was reduced. Normal experience has shown these films are technically too thin to exhibit visible coloring; nevertheless, the samples showed tinting. To determine the cause of the coloring, Run No. 528 was broken into run steps. Only hydrogen cleaning was performed on this sample. As seen in Figure 3, this resulted in a film darker than those in Run Nos. 526 and 527. It was determined that the hydrogen was physically altering the Arylite polymer film and causing the coloring. The best sample created (Run No. 531) used no additional hydrogen in the run. Run No. 532, which used N-DLC parameters, provided the next best sample. Run Nos. 533/534, 535/536, and 537/538 utilized the run parameters of Run No. 531, with run durations of 5, 10, and 15 min, respectively, and film coatings on both the front and the back sides of the Arylite polymer. Run No. 539 utilized O-DLC parameters. Although this film was technically clearer than that in Run No. 532, it is believed to be much thinner.



**Figure 3. Comparison of DLC, N-DLC, and O-DLC Coated PFE (Arylite) Polymer Films.**

### 3.2 MEMS

Micro Electro-Mechanical Systems (MEMS) were coated with a DLC film to reduce friction. Run Nos. 500 and 501 were combined onto the samples, with no break in vacuum between runs.

Run No. 500 was initiated using a 5-min deposition at high energy to increase the adhesion between the DLC and the substrate. The run was performed at a lower energy to increase the resistivity of the film. Run No. 501 was performed to increase the thickness on the MEMS devices. The total film created on the silicon witness sample was 2.65 μ thick. To date, this is the thickest film created that also had 100% adhesion. The MEMS devices also had 100% adhesion in a normal environment. No tape adhesion test was performed.

### 3.3 Metal Coupons

Metal coupons (2 x 2 cm) made of 316 stainless steel and 4140 steel were provided for a joint effort with Moyno Industries through Wright Technology Network and Wright Materials Laboratory. The intent of this coating project was to provide an environmentally friendly replacement for chromium--the current coating--while improving the wear characteristics of the scrolls utilized in the slurry pumps.

Fourteen depositions, Run Nos. 556-564 and Run Nos. 568-572, were performed for this test matrix. For each deposition run, two 316 stainless steel coupons and two 4140 steel coupons were used. Five of the deposition runs created films that failed the tape adhesion test. These failed films were removed from the metal coupons, and the film parameters were rerun with a base coat applied to increase the adhesion of the films. This resulted in nine completed deposition runs Nos. 556-558, 562-564, and 570-572). Figure 4 is a photograph of the samples after being coated. These coupons were deposited with DLC and with low-nitrogen-concentration  $CN_x$  using single-ion-beam deposition. The test results posted for these samples probably could be improved with the deposition of dual-ion-beam deposited  $CN_x$ .

After coating, the samples were sent to The University of Dayton Research Institute (UDRI) for three tests: hardness, wear, and corrosion.

#### 3.3.1 Hardness Testing

The samples were tested for hardness. Table 2 on the following page summarizes the results obtained from UDRI. For comparison, the average range of hardness for bare 4140 steel, 316 stainless steel, and hexavalent chrome are also displayed. As shown in the table, samples from Run No. 572 were the only ones comparable to samples coated with hexavalent chrome, with the 4140 steel being a better match than the 316 stainless steel. The extremely wide range difference cannot be explained, since the hardness of the coating should be independent of the substrate--assuming that the hardness of the substrates in question does not differ drastically. In that case, the substrate may have some effect.

The gas parameters in all deposition runs were varied to determine whether the various gas mixtures would affect the friction and wear characteristics. The ion energy was chosen in all cases to be 1500 V for the initial coat since previous research had shown that film stresses from lower energy deposition films cause failure of the film to adhere to metals. However, experience indicated that this did not occur with  $CN_x$  films. Adhesion, while not quantitatively tested, appeared to be better than with DLC, even at low deposition energies.

The rf power was set at 300 W for all depositions, except for Run Nos. 570 and 572. These two runs had the No. 571 had a hardness value comparable to that of Run No.570 but was performed using 150-W RF power. The film thickness of the witness sample for this run was 1000 Å less than that for Run No. 570. All three runs--Nos. 570, 571, and 572--had similar film thicknesses that were approximately 50-75% greater than those of the other film depositions. This could possibly explain the differences as well, although this should not be the case. It is possible that the film thicknesses of Sample Nos. 570, 571, and 572 exceeded the surface roughness of the

substrates, providing complete versus partial film coverage of the substrate, a problem that must be considered when depositing thin films. This is plausible, considering that the surface roughness of the substrates was unknown and that the hardness values of the thinner films approached the hardness values of the substrates themselves. Further studies must be conducted to determine whether the hardness was associated with the deposition conditions or the film thickness. Likewise, knowledge of CN<sub>x</sub> films gained during this program indicates that further improvements are possible.

**Table 2. Vickers Hardness**

SAMPLE NO.	FILM THICKNESS (Witness Sample**)	SUBSTRATE	VICKERS	STANDARD DEV.
Bare 316SS*			225	
Bare 4140 Steel*			315	
Hexavalent Chrome*			900-1100	
556	6078Å	316SS	333.71	39.68
		4140 Steel	332.64	69.92
557	10800Å	316SS	373.26	73.64
		4140 Steel	374.52	96.39
558	4794Å	316SS	260.71	122.54
		4140 Steel	303.08	109.28
562	8805Å	316SS	353.76	66.87
		4140 Steel	378.62	114.77
563	6653Å	316SS	342.08	46.27
		4140 Steel	275.46	86.02
564	8741Å	316SS	423.55	118.81
		4140 Steel	247.88	33.16
570	13900Å	316SS	534.89	113.97
		4140 Steel	555.38	177.69
571	12900Å	316SS	427.87	59.32
		4140 Steel	543.73	124.50
572	14300Å	316SS	637.50	338.40
		4140 Steel	935.91	320.13

\*Average Published Values

\*\*Glassy Carbon Substrate

### 3.3.2 Wear Testing

Wear testing was performed using a pin-on-disk setup with a 0.375-in. stainless steel ball at an applied force of 20 lb. The disk was spun at 40 RPM for 10 revolutions. No mention was made in the UDRI report of the medium in which the test was performed; therefore, it is assumed that the test was performed in open air on dry surfaces.

The tests appear to be non-conclusive. The films provided were extremely thin compared to the

hexavalent chrome coatings. Additionally, UDRI reported the wear track data for the hexavalent chrome in track width instead of depth, whereas the film-coated samples were reported in wear depth. Table 3 contains the results on the films tested by UDRI. A more suitable measurement would be the wear depth or track width per revolution. This test would provide an equal comparison with the hexavalent chrome. Likewise, it would be desirable to develop a computer-controlled test that measures the frictional force per revolution.

From the table it would appear that Substrate Nos. 556, 557, 563, and 564 performed better with a lower wear track depth indicated. A comparison of wear track depth and Vickers Hardness indicates that the softer films provided better lubrication between the ball and the coating. This may indicate that the coefficient of friction for the harder surfaces is greater than that for the softer films. The coefficient of friction for hexavalent chrome is 0.16. These data, however, were not provided for the coatings on the sample runs performed.

**Table 3. Wear Track Depth (microns)**

Sample No.	4140 Steel	316 Stainless Steel
556	1	2
557	1	2
562	1.5	2
563	1	2
564	1	2
570	2	2
571	2	4
572	2	2

### 3.3.3 Corrosion Testing

For corrosion testing the samples were placed in a salt-spray chamber per standard ASTM B-117 for a period of 240 hr. The uncoated lips of the samples were masked to eliminate corrosion effects from the uncoated substrate.

Table 4 on the following page shows results relevant to the amount of corrosion visible on the 4140 steel substrates. According to UDRI, no visible evidence of corrosion on the 316 stainless steel substrates was present; however, evidence of streaks of discoloration across the coating surface was observed, indicating that some pitting did occur on some of the 316 stainless steel substrates. UDRI indicates that this pitting appeared across the entire surface on Sample No. 571 but only in localized areas on Sample Nos. 557, 562, and 563.

Hexavalent Chrome is resistant to most organic acids, gases, oxygen, moisture, and sulfur but can be attacked by chlorides such as hydrochloric acid, sulfuric acid, or formic acid. However, even though the nitrated version of DLC films was not environmentally tested, DLC films are inert to acids, solvents, and salts. It is not clear why the films on 316 stainless steel showed no evidence of corrosion, as compared to those on 4140 steel. The streaking on the 316 stainless steel may be dried salt residue. The pitting would be attributed to pinholes in the film. The red-

rust corrosion as evidenced on the 4140 steel would also result from pinholes in the film. The testing, however, showed that the film from both substrates remained intact and did not lift off, which indicates that adhesion to both substrates was good and that no micro-channeling occurred. Run Nos. 562 and 570 did show promise, with the percent area covered with corrosion being 40% and 20%, respectively.

Further tests must be performed to confirm that the film adequately protects the surface, and the films should be checked under a microscope for pinholes.

**Table 4. Corrosion Test Data**

Sample No.	% Area of 4140 Steel Covered by Corrosion
556	100
557	100
562	40
563	90
564	100
570	20
571	100
572	100

### 3.4 Carbon-Composite Coupons

Eight samples were received--four with the fabric weave parallel to the deposition surface and four with the fabric weave perpendicular to the deposition surface. Figure 5 is a photograph of the samples after coating. These samples were provided by Dr. Lewis Rosado of AFRL/PRTM, Mechanical Systems Branch, Turbine Engine Division. The purpose of the nitrided-DLC coating was to seal the pores within the carbon composite to prevent oil uptake. The carbon composite is used as a bearing spacer in high-speed turbine bearings. The parallel weave represents the outer and inner surfaces of the spacer, and the perpendicular weave represents the inner bearing surface. The oil uptake from the bearing spacer interferes with the oil surface-wetting phenomenon that reduces friction, causing an increase in friction and premature failure.

The samples were 1/2 in. wide × 2 in. long × 1/4 in. thick. The deposition surface was 1/2 in. × 2 in. To maximize the number of film coatings, the samples were coated on the front and back sides. The sample coatings were performed in Deposition Run Nos. 556-560 and 565-567. Lubrication uptake tests to determine the amount of sealing performed by the nitrided-DLC films were performed by the Materials Directorate.

As with the collaborative tests, these were preliminary tests performed to determine the feasibility of the coating. Knowledge of the material was lacking and test variations were insufficient to provide accurate details. However, preliminary results indicated a 10% improvement over the bare substrates. Thicker film coatings along with knowledge of CN<sub>x</sub> gained during this program is anticipated to improve these results.

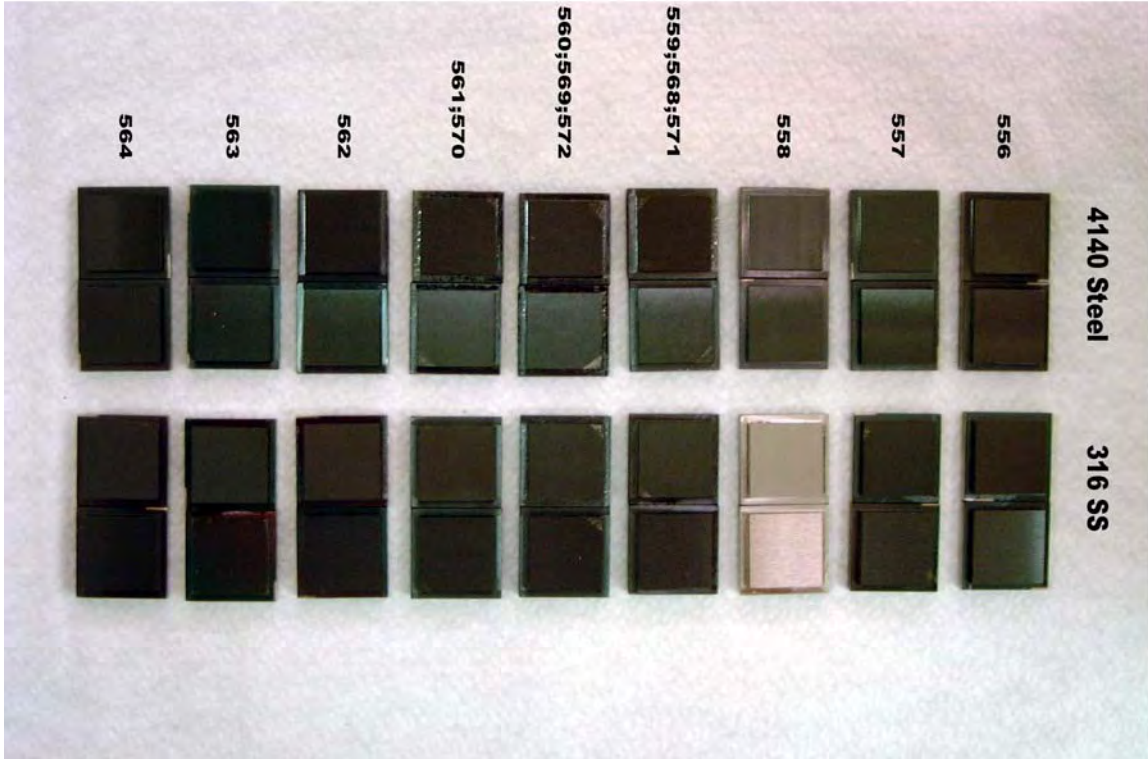
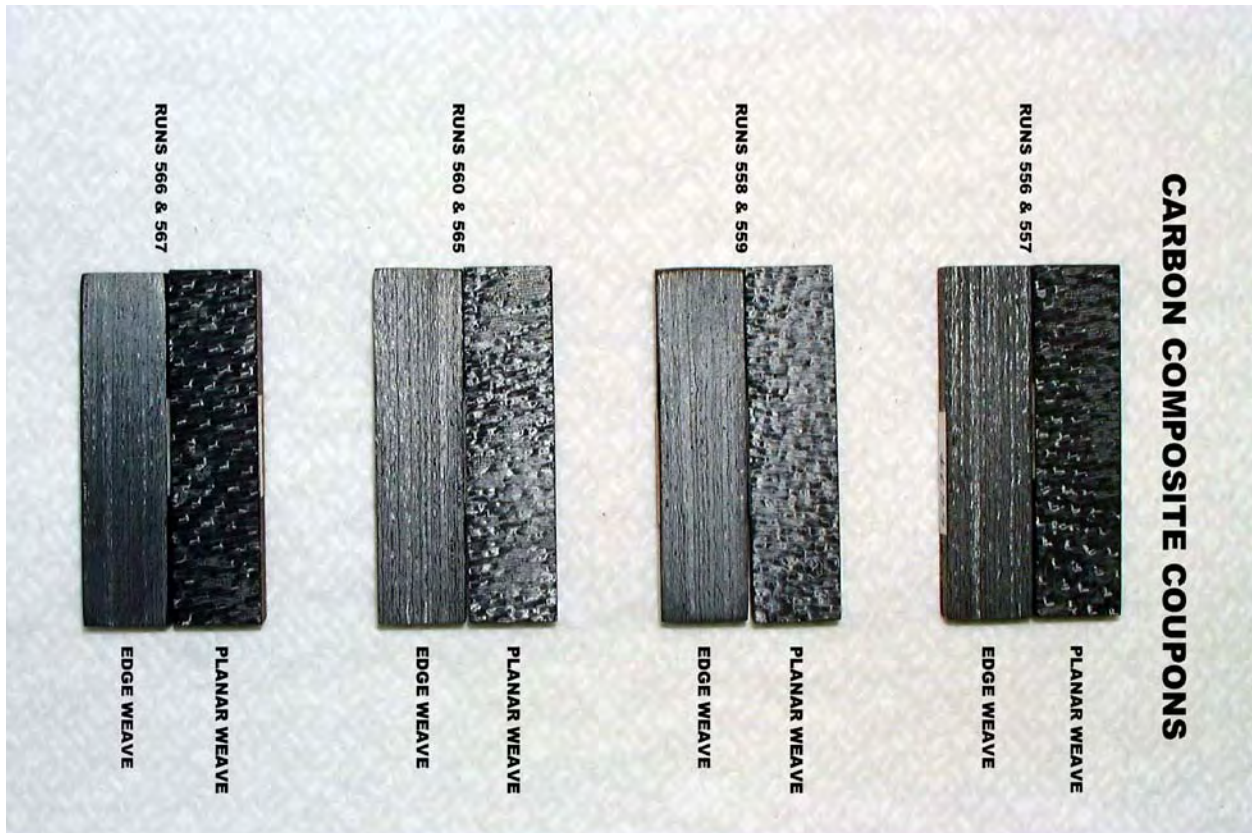


Figure 4. Photo of Coated Metal Samples.



**Figure 5. Photo of Carbon-Composite Samples after Coating.**

## **4.0 EXPERIMENTAL DETAILS**

### **4.1 Setup**

Most of the experimental depositions were performed using LADS. Details of this system were provided in the previous section. A few carbon-nitride film samples were also developed using a magnetron sputtering system located at Ohio University.

Initial film deposition was performed with the system setup in a single-ion-beam deposition mode to produce  $CN_x$  films by directly feeding various ratios and total flows of methane ( $CH_4$ ) and nitrogen ( $N_2$ ) into the 20-cm ion source. The ion source employed is 20 cm in diameter and utilizes an inductively coupled 13.56-MHz rf flat pancake coil antenna that operates with a continuous duty cycle. Dual grids are used to extract ions from the plasma for acceleration toward the sample plate using various acceleration energies. Electron beam neutralizers were utilized during a few depositions to observe differences in film characteristics. This sample deposition plate is located normal to the incident ion beam, 19 in. from the ion source. Figure 6 is a schematic of the single-ion-beam deposition arrangement.

A second (3-cm Kaufman) ion source was installed to provide ion-beam sputtering of a 99.98%, 6-in.-diameter carbon target. The carbon target was mounted to a thermally floating, electrically grounded back plate approximately 8 in. from the sample plate. In the 3-cm ion source, 99.999% argon was used for physical sputtering of carbon. This was changed to 99.999% nitrogen to perform reactive sputtering of carbon. Concurrently, 99.999% nitrogen was fed into the 20-cm ion source for assisted deposition to enhance and assist deposition of the growing sputtered film. Substrates were mounted to the water-cooled substrate holder that was maintained at temperatures ranging from 5 to 35°C--up to 150°C with sample heaters.

In the original orientation, the 3-cm ion source was located 45° off normal and at a distance of 12 in. from the sputter target. Likewise, the sputter target was mounted 45° off normal from both the 20-cm ion source and the sample deposition plate. This orientation resulted in large separation distances to prevent shadowing of the 20-cm ion source, which, in turn, resulted in a poor configuration for sputtering and a reduction in the ion-beam density on target due to space-charge separation. Concern was expressed concerning the ion beams from the 20-cm and the 3-cm ion sources crossing paths. Figure 7 is a schematic of the original orientation.

A schematic depicting the reorientation of the dual-ion-beam assisted, ion-beam sputter arrangement is shown in Figure 8. The sputter target was mounted approximately 10° off the normal axis with the sample deposition plate. The sample deposition plate was oriented at two positions--normal and at 10° off normal to the 20-cm ion source. The 10°-off-normal orientation was an attempt to bring the sputter target closer to a parallel orientation with the sample plate, which is limited because of internal mounting restrictions.

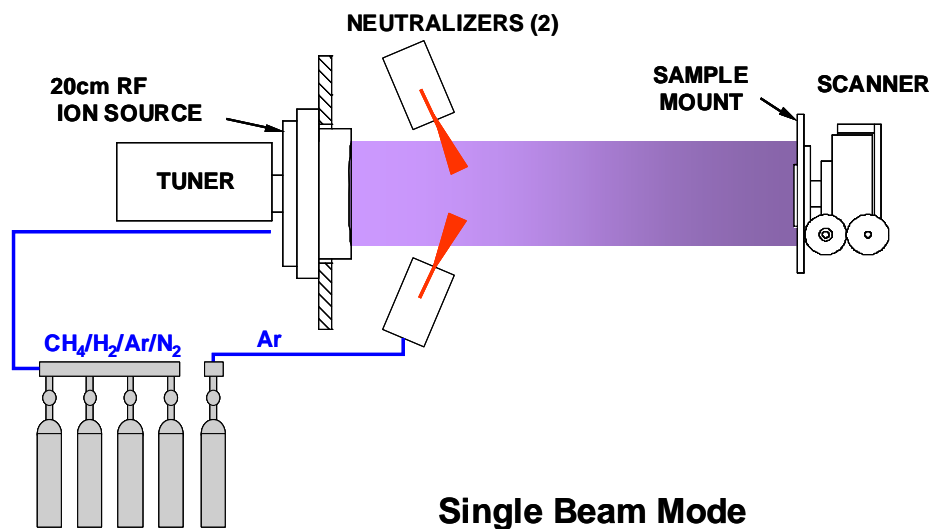


**Figure 6. Diagram Illustrating Single-Ion-Beam Deposition.**

The 3-cm Kaufman ion source was mounted 45° off the normal axis of the sputter target at a distance of 4 in. from the surface. This orientation prevented this ion source from blocking the sputtered flux to the sample-deposition plate and prevented shadowing of the 20-cm ion beam.

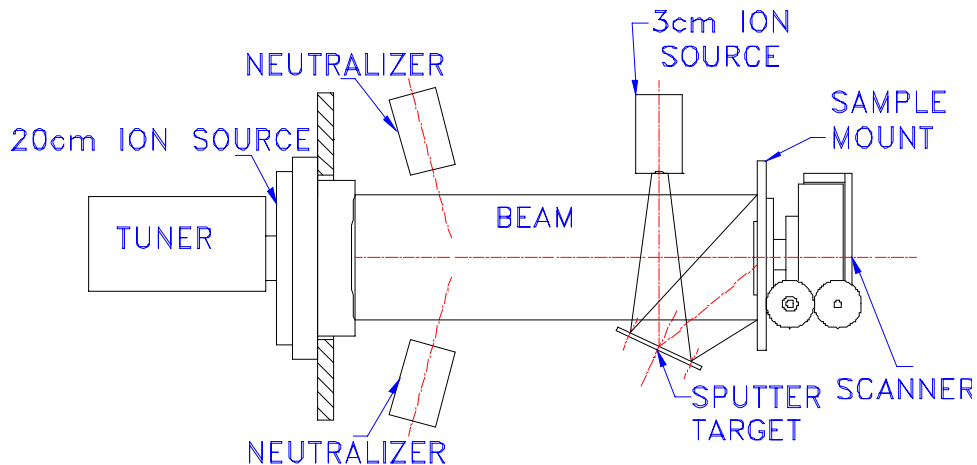


**Figure 7. Diagram Showing Original Orientation of 20-cm Ion Source, 3-cm Ion Source, and Sample.**

#### 4.2 Substrates

Carbon-nitride films were deposited onto various substrates: silicon (Si), glassy carbon (GIC), aluminum-coated silicon (AlSi), nickel-coated silicon (NiSi), chromium-aluminum-coated

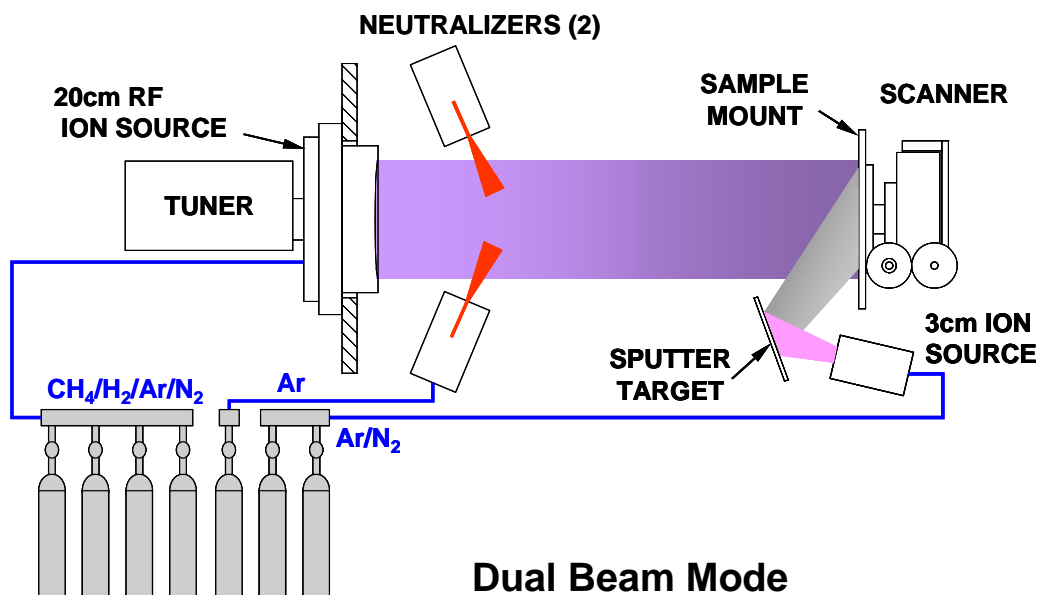


**Figure 8. Schematic of Final Arrangement of Dual-Ion-Beam System, with One Beam Used to Sputter Graphite onto Substrate and Second Used to Bombard Growing Film.**

silicon (CrAl), 7059 corning glass (Gl), quartz (Qz), sodium-chloride salt crystal (NaCl), carbon composite (CC), Fluorinated Polyester (FPE) polymer, 440C steel, and 316 stainless steel.

FPE was utilized in a joint effort to develop a transparent oxygen barrier for flexible flat-panel displays. 440C steel and 316 stainless steel were coated in a collaborative effort for friction and wear testing. Carbon-composite samples were coated in collaboration with the Materials Directorate of AFRL to provide a protective filler coating for eliminating lubrication uptake into composites used for high-speed bearing races in turbine engines. The metal-coated and silicon samples were utilized for the development of capacitors. The remaining samples were utilized for various film characterizations.

To develop parallel capacitor plates, various metals were magnetron sputtered onto polished silicon substrates. Polished silicon samples were used to provide an economical way to achieve very smooth metal surfaces. The sputtered metal base consisted of samples sputtered either with 99.999% aluminum or with 99.999% nickel. A portion of the aluminum deposited samples also had a thin (10-nm) layer of chromium deposited onto the top boundary layer between aluminum and  $CN_x$ . This layer was intended to block possible aluminum diffusion into the later deposited  $CN_x$  film layer.

Glassy-carbon samples were used for RBS, ERS, and thermal analysis. This material provides a cleaner background signal in RBS, which results in better detection of deposited carbon species. Silicon (Si) was used for ERS analysis, capacitor testing, and FTIR analysis. Sodium Chloride (NaCl) crystals were used to provide a very flat background with virtually no absorption in the mid-IR range. Quartz samples were also used for FTIR analysis, but with limiting absorption peaks.

### **4.3 $CN_x$ Film Depositions**

$CN_x$  film deposition parameters were dependent upon the run being a single- or dual-ion-beam arrangement. Initial runs were performed utilizing the single-ion-beam deposition mode. The rf power, ion-beam acceleration energy, gas ratios, gas types, and total gas flow were varied. Based on the various run conditions, a matrix table was being formulated.

The dual-ion-beam deposition mode is more difficult due to the low sputter yields associated with carbon. Parameters were varied with the 3-cm ion source to find parameters that would yield a sufficient amount of sputtered carbon along with the trade-offs to permit the 3-cm ion source to operate stably for extended periods of time. Gas was varied from 100% argon to 100% nitrogen. Argon provides physical sputtering of carbon due to momentum energy. Nitrogen provides some momentum energy, but this energy is intended to create surface reactions with carbon, resulting in reactive sputtering. Indirect parameters were adjusted to yield various beam currents as well. Likewise, acceleration energy was varied. Ideally, the highest beam currents along with the highest acceleration energies result in the highest sputter yields. However, the ion source is unable to operate in a stable mode under these conditions. These parameters were adjusted until operating beam currents at 60 mA at an ion acceleration of 1000 eV were selected. Total gas flow also played a role in this. The 3-cm ion source was operated with a gas flow of nitrogen set at 15 sccm.

A similar situation existed with the 2-cm ion source. The amount of rf energy to generate the plasma was varied to influence the number and type of radical species. This also controls, to a degree, the amount of total ion beam current. The ion beam acceleration, gas species, gas ratios, and total gas flows were varied as well.

Initially, depositions were performed once chamber background pressures were below  $6.6 \times 10^{-4}$  Pa ( $5 \times 10^{-6}$  torr). For dual-ion-beam depositions, runs were initiated after background pressure in the chamber was below  $1 \times 10^{-5}$  Pa ( $8 \times 10^{-8}$  torr). Operating pressures were dependent on the gas ratios and total flows, but most depositions were performed with operating pressures during depositions of  $2.3 \times 10^{-2}$  Pa ( $1.75 \times 10^{-4}$  torr) to  $2.6 \times 10^{-2}$  Pa ( $2 \times 10^{-4}$  torr), respectively.

With single-ion-beam deposition,  $CN_x$  films were grown using 99.999% nitrogen and 99.98% methane at various ratios for directly forming  $CN_x$  film. For dual-ion-beam deposition,  $CN_x$  films were deposited onto the various substrates mentioned using 99.999% nitrogen gas accelerated through the 3-cm Kaufman ion source to sputter reactively a 99.98%-pure graphite sputter target while employing the 20-cm, 13.56-MHz RF broad-beam ion source that accelerates additional 99.999% nitrogen for enhancing and assisting deposition of the growing sputtered film. Substrates were mounted to the water-cooled substrate holder that was maintained at a temperature range of 5 - 35°C.

The objective was to develop  $CN_x$  film with properties suitable for use in high-temperature electronics. Based on this, the deposition parameters of the ion sources were varied. The resulting films were studied with the intent of achieving the following goals and developing a correlation between deposition parameters and electrical properties:

1. Maximize Resistivity
2. Maximize Dielectric Strength
3. Maximize Energy Density
4. Maximize Film Thickness
5. Maximize Capacitance
6. Minimize Dissipation
7. Study Dielectric Constant

#### **4.4 Capacitors**

Si, AlSi, CrAlSi, and NiSi substrates were used as the base plate for creating bottom electrodes for capacitor structures. The AlSi, NiSi, and CrAlSi start from a base substrate of polished Si to provide a smooth, uniform layer. Magnetron-sputtered aluminum (1500 Å) was deposited onto 1 in.  $\times$  1 in. silicon plates to form the bottom electrode plate of the capacitor. One-half of those aluminized silicon plates have an additional 100 Å of chromium deposited on top of the aluminum to provide an interstitial buffer layer between the aluminum and the  $CN_x$  film that will be deposited. The chromium layer is intended to prevent aluminum diffusion into  $CN_x$  film, minimizing the possibility of creating an electrical short in the developed capacitors. NiSi substrates had 1500 Å of nickel magnetron-sputtered onto separate polished silicon samples.

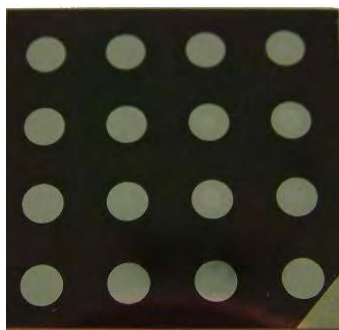


**Figure 9. Image of Created Flat-Plate Capacitor Array.**

Plain polished Si is also used as a bottom electrode plate for capacitors, forming a metal-insulator-semiconductor (MIS) structure commonly found in electronics. Prior to using silicon as a substrate base,  $1 \times 1$  in. corning-glass substrates were employed. These substrates used  $100 \text{ \AA}$  of chromium deposited onto the glass to enhance adhesion of the aluminum layer (AlG).

Capacitors were formed by depositing  $\text{CN}_x$  on the Si, AlSi, NiSi, and CrAlSi samples. Prior to  $\text{CN}_x$  deposition, these samples were masked at one corner to provide an electrical connection to the back plane. After deposition, the  $\text{CN}_x$ -coated electrode plates are mounted to a patterned mask, where aluminum dots of 3-mm diameter were e-beam evaporated to a thickness of  $2500 \text{ \AA}$  on top of the deposited film, forming an array of 16 parallel-plate capacitors with a single back-plane electrode of aluminum. For the CrAlSi samples, another  $100 \text{ \AA}$  of chromium was deposited onto the  $\text{CN}_x$  film prior to deposition of the  $2500 \text{ \AA}$  of aluminum. Figure 9 is a schematic of the completely developed capacitor, and Figure 10 contains an image of a developed capacitor.

## 5.0 RESULTS

### 5.1 Deposition-Chamber Preparation

The manner of pumping--cryogenic only, turbo only, or a combination--during  $CN_x$  film deposition does not appear to affect the composition of the created film, although the deposition

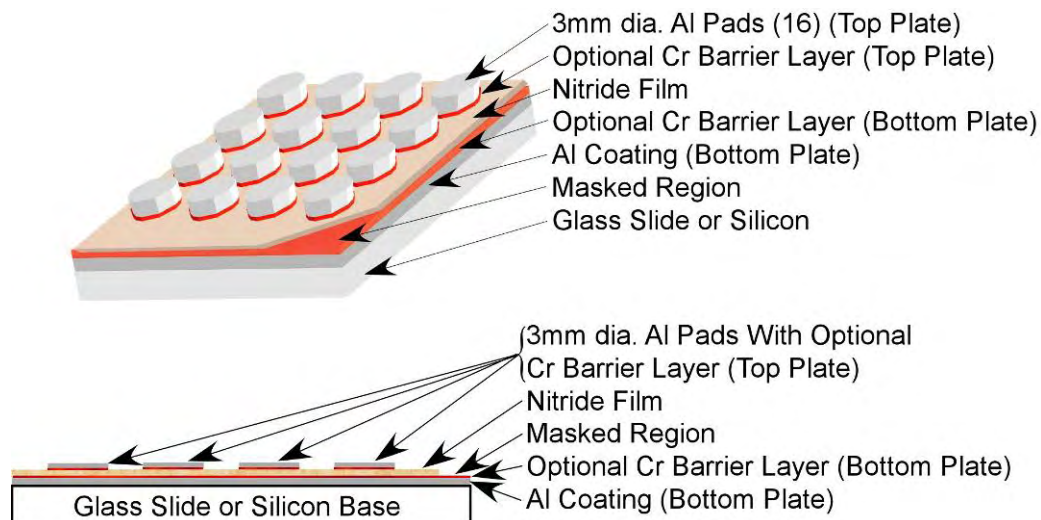


**Figure 10. Schematic of Developed Parallel-Flat-Plate Capacitor Array.**

chamber pressure did vary from  $8 \times 10^{-4}$  down to  $2 \times 10^{-4}$  torr, respectively.

Initial background pressure in combination with low-temperature chamber baking had no effect. For samples deposited with initial background pressures of  $5 \times 10^{-8}$  torr and quartz-lamp internal bake-out, hydrogen concentrations within the resultant  $CN_x$  films were lower than for samples deposited with initial background pressures at  $1 \times 10^{-6}$  torr and no bake-out.

### 5.2 Film Adhesion

Film adhesion is determined qualitatively by visual inspection of each sample upon removal from the deposition chamber. Most samples were visually determined to have 100% adhesion onto the substrate. The addition of nitrogen into the film is beneficial to the adhesion properties. Adhesion of  $CN_x$  appears to be better in comparison with standard DLC films. This is evident with low as well as high concentrations of nitrogen. Adhesion with the sample-deposition mounting plate was so great that the plate had to be wire brushed to remove the film. For DLC samples removal was accomplished with water and a scotch-brite pad.

Under almost all conditions, film adhesion was excellent. Tests were also conducted by immersing the sample into de-ionized water for 5 min. All immersed films remained intact with the substrate.

The majority of sample depositions occurred at room temperature or slightly above that level. Deposition temperatures are discussed further in a later section. However, some adhesion failures occurred on samples that were deposited with the substrate held below room temperature prior and during deposition. For these depositions, some degree of film failure occurred once the sample was exposed to atmospheric conditions, except in the case of nickel substrates. The reasons for this are not clear. At cooler temperatures it is possible that water was reducing the bonding at the interface. For background pressures of  $1 \times 10^{-6}$ , a monolayer of water developed onto surfaces within 1 sec, and at  $1 \times 10^{-8}$ , this occurred within 100 sec. At these rates, water is always be present at the surface boundary unless the samples are heated prior to deposition. In the case of nickel substrates, it is possible that adhesion of  $CN_x$  can overcome the water barrier through stronger and better matched bonding with nickel.

Another consideration is increased film stresses at lower temperatures. Surface heating or induced energy into the lattice relaxes film stresses. From the films that failed, it appears that the film stress was compressive, as indicated by the film relaxing once it was at atmospheric pressure--indicated by the film expanding and lifting from the substrate.

### **5.3 Sample Preparation**

While it is important that substrates be clean prior to film deposition, the cleaning procedure appears to have no influence on film adhesion. The exception to this would be pre-heating samples prior to the onset of deposition, as mentioned above. However, in the case of low-temperature depositions, the lack of adhesion was noticed at the end of the program, and no further studies were conducted on improvement.

The cleaning methods utilized were 1) acetone in ultrasonic, de-ionized water (D.I.) rinse, nitrogen dry; 2) ethanol in ultrasonic, D.I. rinse, nitrogen dry; and 3) Procedures 1 and 2 repeated with argon or nitrogen sputtering for 1 and 5 min prior to deposition. Sputtering was performed at normal incidence and  $10^\circ$  off normal incidence. There is no evidence of improvements with these cleaning procedures as compared to using apparently clean samples and directly depositing the film.

### **5.4 Film Growth Rate**

Single ion-beam deposition resulted in a higher  $CN_x$  film growth rate compared to dual-ion-beam deposition. However, dual-ion-beam deposition resulted in films with significantly less hydrogen and more nitrogen. For both single- and dual-ion-beam processes, the deposition rate was highest with no nitrogen gas added. As the nitrogen concentration within the gas mixture increased, the deposition rate decreased. There is evidence of variations in film thickness as a function of substrate materials. Glassy-carbon samples consistently displayed the highest growth rate, which can be accounted for by a shorter initial incubation growth period onto a carbon substrate as compared with other substrates.

Various growth conditions resulted in varying rates of deposition. For single-ion-beam deposition, deposition rates ranged from 10 to 130 Å/min. For dual-ion-beam deposition, rates

varied from 0.5 to 20 Å/min.

For single-ion-beam deposition, 99.99% CH<sub>4</sub> was mixed with 99.999% N<sub>2</sub> in various ratios and with various total gas flows. The rf power was varied from 150 to 600 W and ion acceleration varied from 50 to 100 eV.

Dual-ion-beam deposition of CN<sub>x</sub> film presented a unique challenge. The 3-cm ion source was used to sputter a carbon target, and 100% of 99.999%-pure N<sub>2</sub> was used as the source gas to provide reactive sputtering of the carbon. This deposited a CN<sub>x</sub> film onto the substrate. However, the amount of nitrogen incorporated into the resulting film was lower than desired. Therefore, the second 20-cm ion source was used to provide a broad beam of nitrogen for enhancing the nitrogen concentration into the film while increasing the adhesion and density of the film. However, a delicate balance exists between the quantity of nitrogen and the impinging ion energy since nitrogen is a reactive gas with carbon. This resulted in a competition between the growth rate of the carbon-nitride film that is sputtered onto the surface and the etch rate associated with the nitrogen ions that impinge on the carbon-nitride surface. This effect could be observed clearly in Sample Nos. 637 - 644, where higher nitrogen beam currents drastically reduced the total film thickness, and the substrates indicated that substrate sputtering occurred prior to film development.

In those samples the beam current increased four-fold during a change of ion-source grids and the quartz rFF transmission window.

For all other samples with film deposition, the measured film growth was relatively slow. The result was thin dielectric films. Thinner films usually have minor defects that become insignificant with thicker films. For a capacitor the ideal situation would be to develop the thinnest possible film. However, for a real capacitor device, a trade-off must be made between the dielectric thickness and the ability of the dielectric to perform under real growth conditions. This means that the deposition system must be run as long as possible to grow thicker films. The limitation to this process is that the filament ion source used for sputtering the carbon has an average life of 10 hr. Depending upon the growth conditions established for a particular deposition run, the average film thickness ranged from 108 to 7504 Å, with a median value of 1978 Å. Achieving an average film thickness of ~ 5000 Å on a capacitor would be desirable. This can be accomplished by performing several deposition runs on the same sample set and by performing a clean etch of the film between each run to remove the contamination layer that results when the sample is exposed to the atmosphere during filament changes on the ion source. The extended deposition time would be undesirable in a production setting. This limitation can be overcome by converting the sputter ion source to an rf sputter ion source. Also, adding film-thickness monitors to the system would allow the growth rate of the CN<sub>x</sub> film to be correlated with the correct amount of nitrogen flux from the broad-beam ion source. The overall effect would be an increase in film growth rate along with better control of film quality.

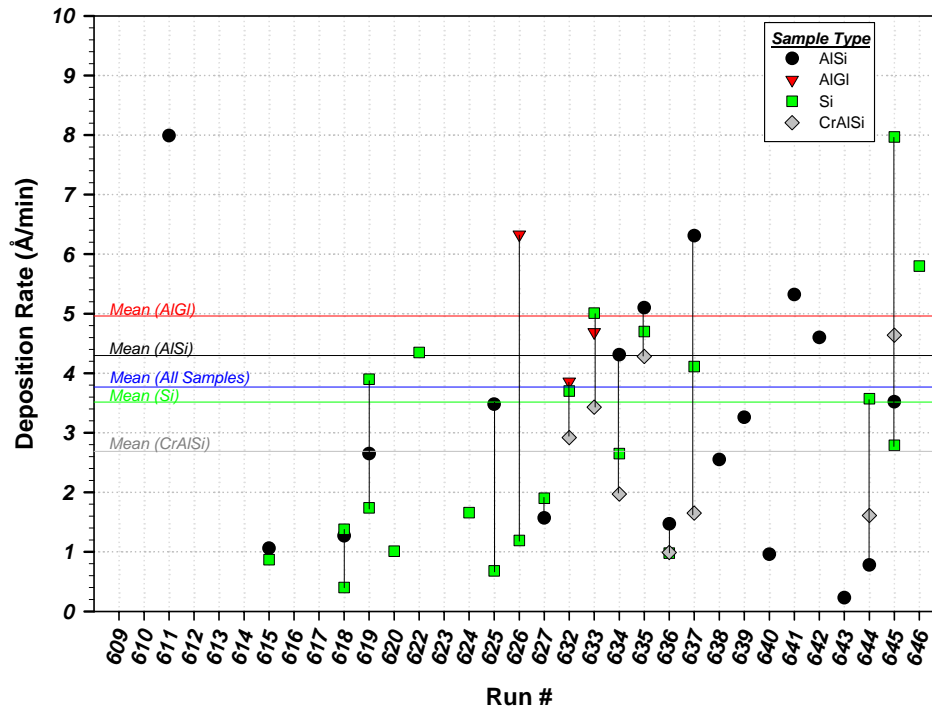


**Figure 11.  $CN_x$  Deposition Rate for Various Runs and Substrate Materials.**

Figure 11 displays the deposition rate for the four types of capacitor plates developed under this program. Changes in operating parameters and conditions from each experimental run created the scattering that is evident. In a comparison of the mean values, it appears that  $CN_x$  grows at a faster rate on aluminum-coated substrates, followed by silicon and then chromium. These rate changes are thought to occur during the incubation period when the film is initially grown on the substrate, where bonding of  $CN_x$  to aluminum occurs more rapidly than with the other materials. This also corresponds to the problems of aluminum diffusing into the  $CN_x$  matrix, which reduces the effectiveness of the  $CN_x$  dielectric.

The mean deposition rate of all samples is 3.8 Å/min. For comparison, the mean for aluminum on glass (AlGI) is 5.0 Å/min, for AlSi is 4.35 Å/min, for Si is 3.55 Å/min, and for CrAlSi is 2.7 Å/min. To deposit 5000 Å of  $CN_x$  using the mean growth rate on AlSi would require 19 hr of deposition run time utilizing the present deposition arrangement. Altering the ion-gun setup for production should increase the rate of  $CN_x$  deposition.

### 5.5 Deposition Temperature

Single-ion-beam depositions were performed with sample-deposition temperatures maintained at less than 100°C. The sample-mounting-plate cooling temperature was varied from 5°C to 35°C. Within this temperature range, no effects were noticeable.

As will be discussed in later sections, the hydrogen concentration within all sing-ion-beam-deposited samples was very high and the nitrogen concentrations peaked at 15%. A sample heater was developed for addition to the system to provide elevated-temperature depositions. The expectation was to raise the deposition temperature of the film to assist with liberating hydrogen bonded to the film, thus decreasing the amount of hydrogen in the  $CN_x$  film and increasing the nitrogen content.

Deposition temperature is a concern with regard to the overall properties of the deposited film. Figure 12 displays several dual-ion-beam deposition runs performed with recorded temperatures as a percent of run time. Percent run time was chosen because of varying durations of run time between sample sets. Sample No. 646 is the highest recorded deposition on this graph at 150°C average temperature. This sample achieved that temperature with assistance from front-surface quartz lamps inside the deposition chamber. All other depositions shown are below 110°C. Higher deposition temperatures assist with further reactions on the deposition surface. This method is usually performed for crystalline growth. For electrical-isolation requirements of  $CN_x$  samples,  $sp^3$  bonding is desired. For diamond growth this is achieved with high temperatures. However, amorphous films such as DLC and  $CN_x$  consist of multiple combinations of bonding.

Higher deposition temperatures of  $CN_x$  films or higher film surface energies due to energetic ions appear to result in higher graphitic structures that are  $sp^2$  bonded, which resulted in low-resistivity films. There are indications that at temperatures greater than 200°C, higher graphitic structures are created, while higher levels of  $sp^3$  bonding occur in depositions less than 100°C. Attempts were focused at growing films at temperatures less than 25°C; the properties of these films were not measured.

## 5.6 Thermal Annealing

After film depositions, the glassy-carbon and silicon samples were heat-treated in a quartz tube furnace with 99.999% argon flowing. The samples were heat-soaked for 20 min and then allowed to cool to room temperature while maintaining argon gas flow. Separate samples were individually soaked at the various temperature ranges, incremented at 100°C and starting from 100°C up to 900°C.

Rutherford Backscattering Spectroscopy (RBS) and Elastic Recoil Spectroscopy (ERS) were performed on the heat-treated as well as the room-temperature (non-heat-treated) samples. RBS was used to measure the elemental composition of the films, and ERS was used to determine the hydrogen content of the films.

Figure 13 is a graph of a sample with a low hydrogen concentration of 1.23%. The nitrogen concentration within the film decreases at temperatures above 600°C. This sample is representative of those with the highest thermal stability.

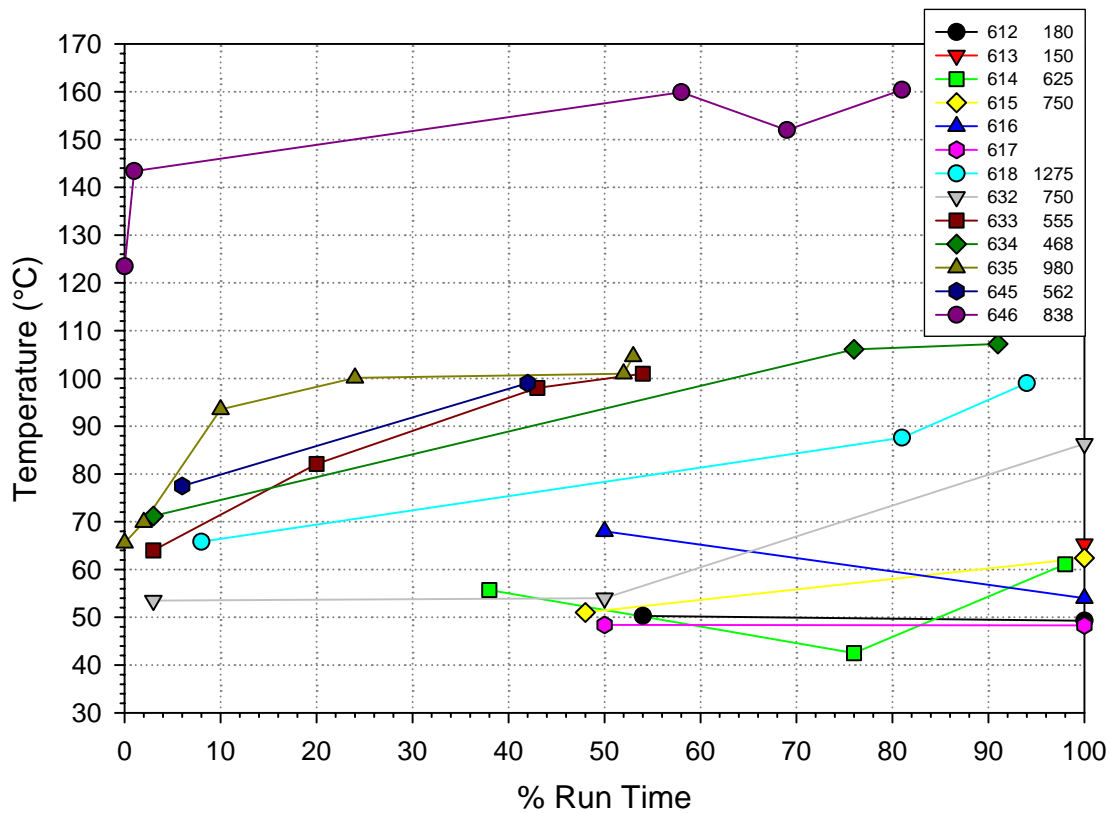
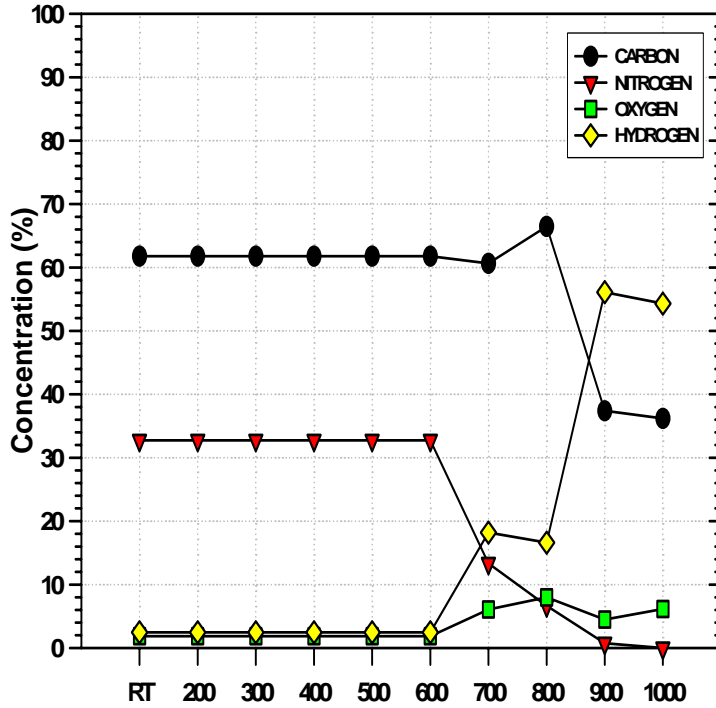


Figure 12. Graph of Sample Temperatures during Various Deposition Runs.



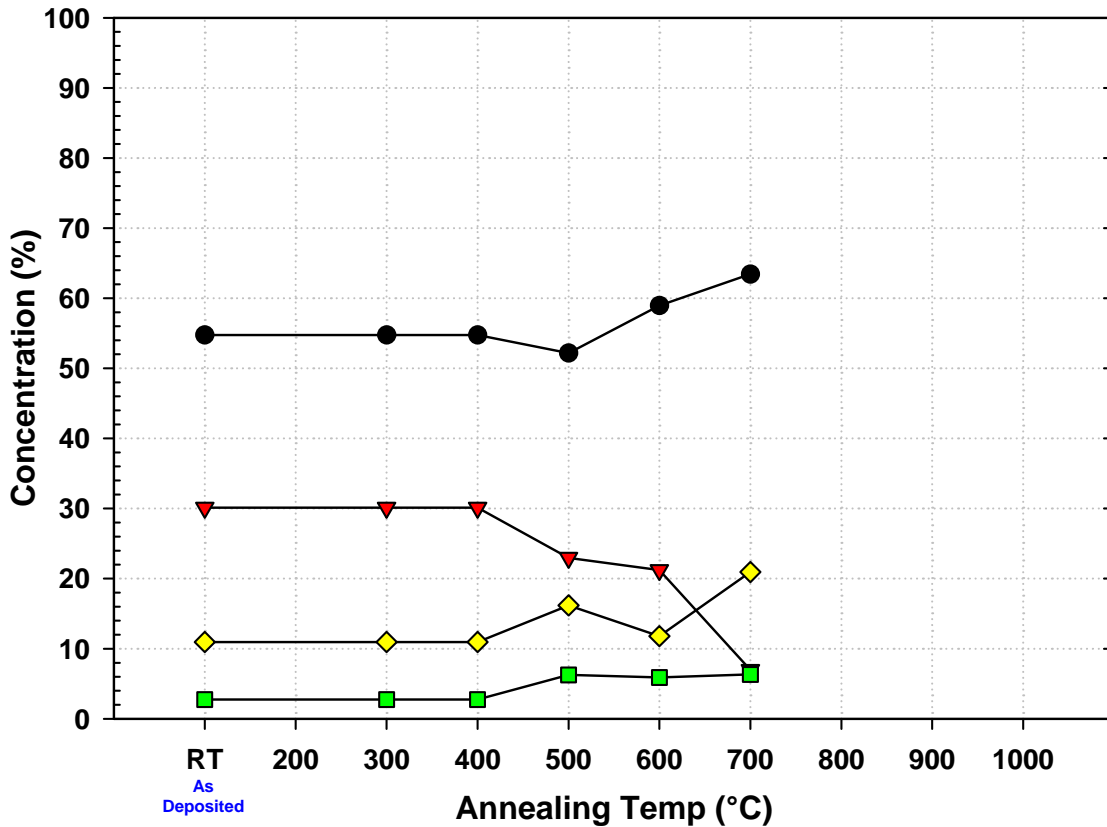
**Figure 13. Elemental Composition of Film with 1.23% Hydrogen Concentration.**

Figure 14 is a compositional graph of a sample with 11% hydrogen. The nitrogen concentration in the film for this sample decreased, starting at 400°C. In both graphs the hydrogen concentrations increased as the film compositions changed. A side study into this indicated that hydrogen was diffusing through the quartz tube wall at elevated temperatures and was being absorbed into the film. It is possible that the hydrogen replaced nitrogen in the  $CN_x$  film, induced by thermal energy.

## 5.7 Imaging

### 5.7.1 Optical Microscopy

Table 12 (p. 76) summarizes the results from optical viewing of the samples. The sample images were taken as viewed with a  $\times 10$  magnification lens and with a  $\times 10$  magnification eye piece. Each image was physically viewed, with bright image spots being counted as pinholes and dark image spots being counted as contamination. The total count was then calculated with the total viewing area to yield the resulting values of pinholes/ $mm^2$  and contamination/ $mm^2$ . The resulting values are subjective with regard to the image taken and the physical counting of each image spot. Optical viewing was over the entire sample, and the resulting image obtained was deemed to be representative of the entire sample. Figure 15 is an optical image of Sample 645 Si, showing that the film is relatively pinhole-free and very smooth. Figure 16 is an optical



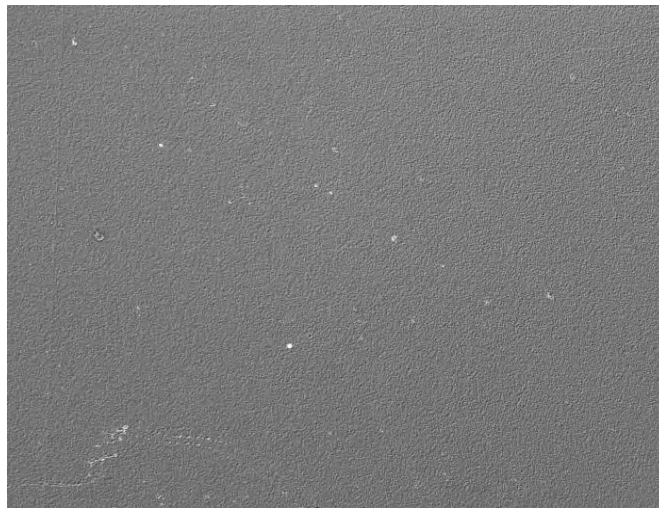
**Figure 14. Elemental Composition of Film with 11% Hydrogen.**

image of Sample 633 AlGI, which shows it to have a higher pinhole count and a rough film surface. Figure 17 is an optical image of Sample 646 CrAlSi. Although the electrical properties of chromium-coated samples were poor, the optical image appears to be relatively smooth and pinhole-free. This image is characteristic of all of the chromium samples.

Table 12 summarizes the pinhole and contamination values, as observed optically, for the various substrates. When comparing the CrAlSi substrates with the other substrates optically, it appears that there is no major difference in the pinhole and contamination count. Likewise, in a comparison of the total film thickness of the various substrates, tabulated in Table 11 (p. 73), it appears that there are no major differences between CrAlSi and the other substrates. Since no apparent physical differences between the CrAlSi-substrate-deposited  $CN_x$  and the other-substrate-deposited  $CN_x$ , the electrical differences are thought to be due to the microstructure or morphology of the films.



**Figure 15. Optical Image of Sample 645 Si.**



**Figure 16. Optical Image of Sample 633 AlG.**



**Figure 17. Optical Image of Sample 646 CrAlSi.**

### **5.8 Film Composition**

Compositional analysis of the deposited  $\text{CN}_x$  films was performed at Ohio University utilizing RBS, X-ray Photoelectron Spectroscopy (XPS), and ERS. RBS and XPS can detect the elemental composition within a film for most elements. However, they are not sufficiently sensitive for detecting hydrogen. ERS is incorporated to detect hydrogen concentrations within the films.

XPS was performed using a  $1484 \text{ k}\alpha\text{Al}$  x-ray source and a 125-mm hemispherical analyzer with an 80-eV pass energy in the fixed-analyzer-transmission (fat) mode. RBS and ERS were performed simultaneously with alpha particles from a 2.2-MeV  $^4\text{He}$  ion beam generated from the 4.5-MV tandem accelerator located at the Edwards Accelerator Laboratory at Ohio University. Samples were loaded into a high-vacuum chamber that was pumped to less than  $5 \times 10^{-6}$  torr and were analyzed with the ion beam at normal incidence to the target. Analysis was also performed with samples tilted so that the helium ion beam was incident at  $75^\circ$  to the sample normal. The 2.2-MeV alpha particles were scattered through  $168^\circ$  for the RBS detector, while the protons were forward recoiled at  $30^\circ$  through a 13- $\mu\text{m}$ -thick Mylar foil into a solid state barrier detector for ERS detection. Energy of 2.2 MeV was used to avoid problems due to non-Rutherford scattering from carbon and nitrogen, which occurs at higher energies. The cross section used to determine the hydrogen concentration from ERS data was that of Keay and Ingram.<sup>14</sup>

Initially, samples were deposited onto silicon single crystals. This substrate leads to two problems in ion-beam analysis. First, the signal from the substrate interferes with that from the carbon and nitrogen associated with the  $\text{CN}_x$  film. Second, the single-crystal nature of the substrates can lead to channeling into the crystal lattice by the ion beam. Because of this, the

---

<sup>14</sup>J. C. Keay, D. C. Ingram, Nucl. Instr. Meth. Phys. Res. B 211 (2003) 305.

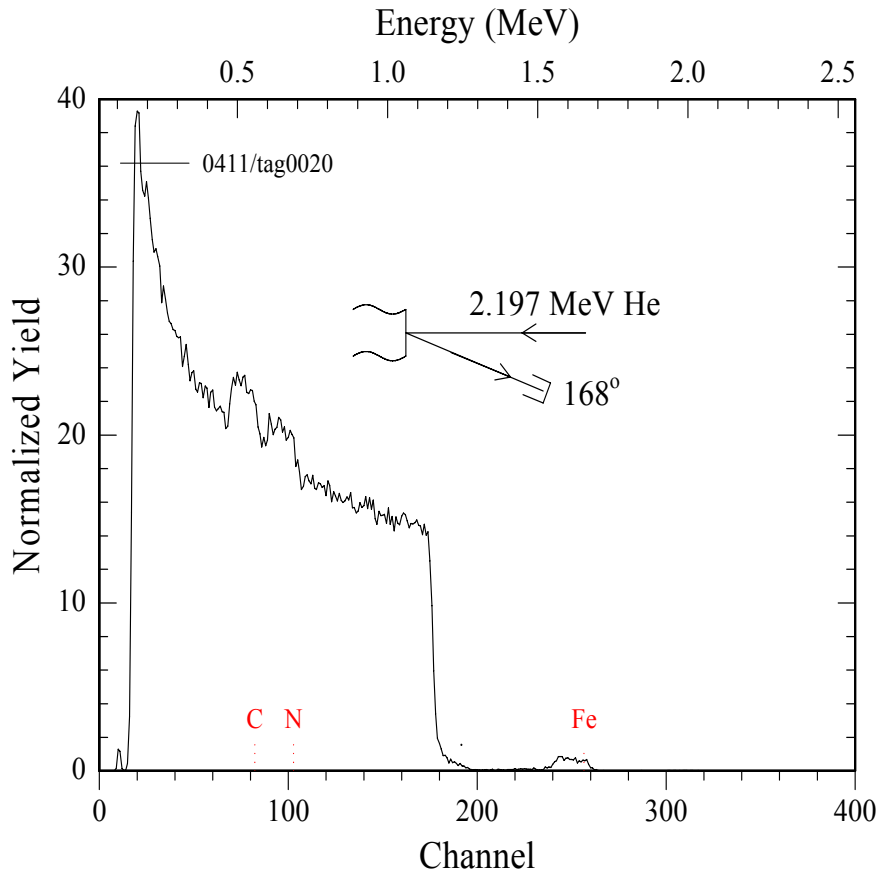
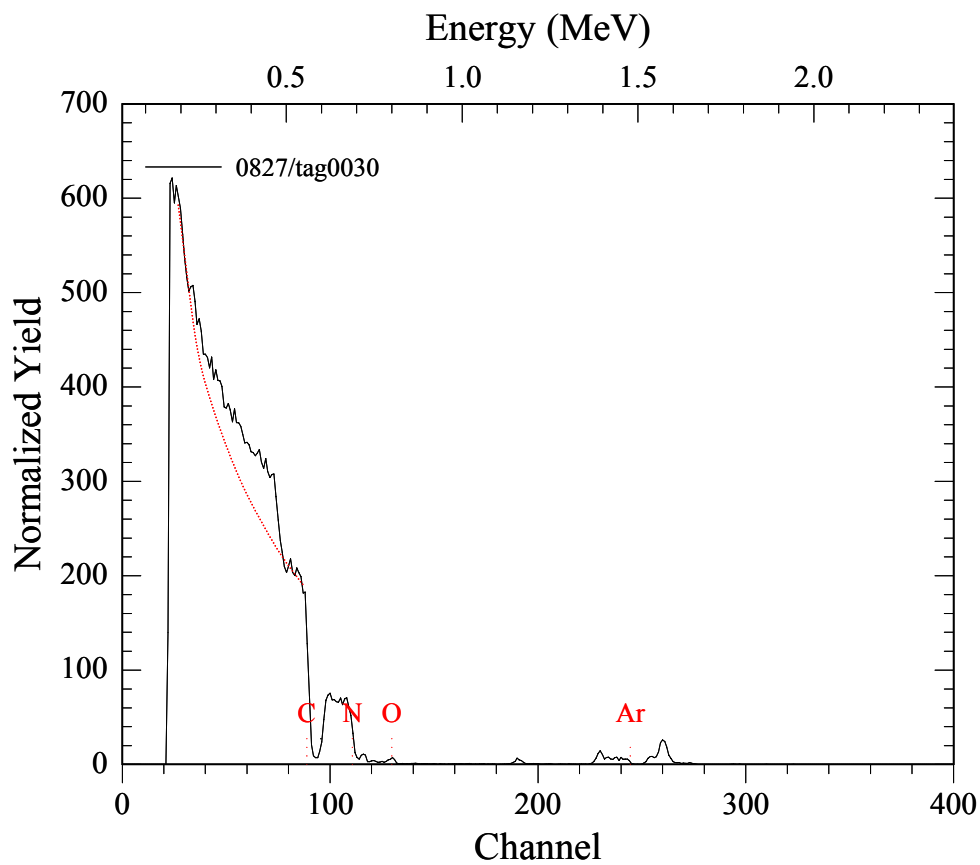


**Figure 18. RBS Spectrum from Sample 491 Using Silicon Substrate.**

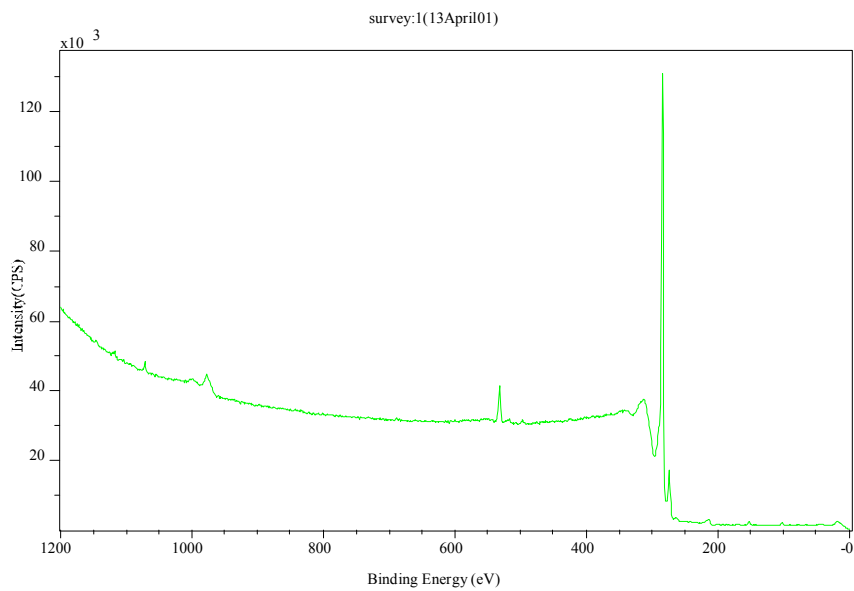
usual method of normalizing RBS data with respect to the substrate background is not possible, since the detection height of the substrate in the spectrum may be lower than expected because of channeling. To avoid these problems, silicon substrates used for RBS and ERS analysis were replaced with glassy carbon. The carbon background from this substrate does not overlay the nitrogen peak, and the amorphous nature of glassy carbon does not create channeling problems during analysis of the carbon peak associated with the film.

Figure 18 contains a typical spectrum from an RBS-analyzed  $CN_x$  film using a silicon substrate. Figure 19 displays an RBS-analyzed  $CN_x$  film using glassy carbon for a substrate, which improves the detection of elements heavier than carbon. Comparison of these two figures shows the larger signal due to silicon as compared to glassy carbon. The dashed line in Figure 19 indicates the estimation for the background, which is then subtracted to obtain the concentration of carbon associated with the  $CN_x$  film. The same process was used in Figure 18 to reduce the detection sensitivity for all elements lighter than silicon. With the glassy carbon, background from a typical silicon sample, as in previous spectra, is not present. Thus, the nitrogen and oxygen peaks are clearly visible, and a step is present in the carbon background where the carbon is in the film.

Figure 20 shows an XPS spectrum of sample #505 with a glassy carbon substrate. The largest peak is from carbon, located at 285 eV. The next highest peak is from oxygen at 520 eV. This spectrum is typical for a pure carbon sample. The oxygen is from exposure to the air and is always present at the substrate surface. This was used as an XPS background reference spectrum for deposited  $CN_x$  films onto glassy carbon.



**Figure 19. RBS Data from Sample 505 with Glassy Carbon**



**Figure 20. XPS Spectrum of Glassy-Carbon Substrate.**

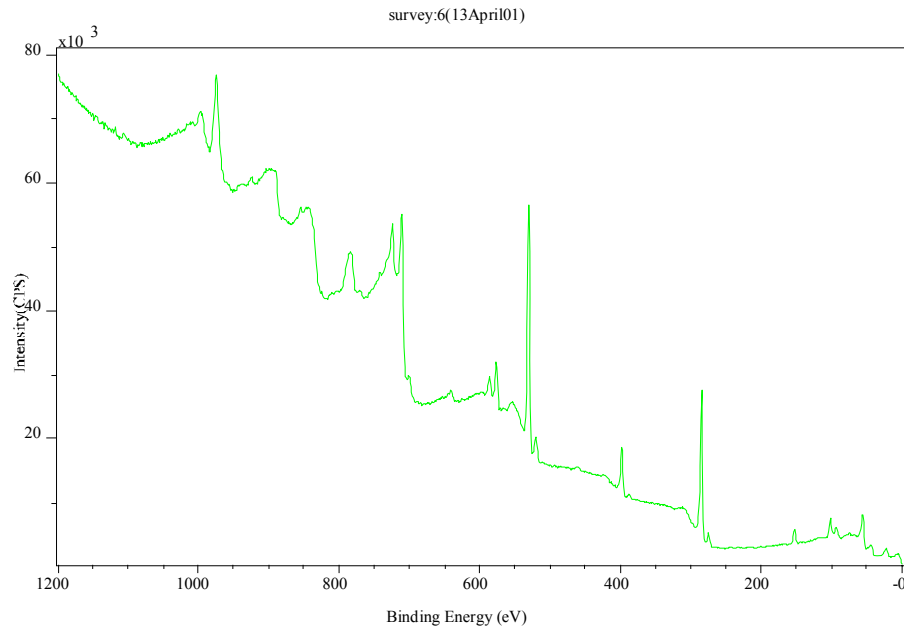


**Figure 21. XPS Spectrum of Sample No. 487 Prior to Sputter Cleaning Top Surface Layer.**

### 5.8.1 XPS Analysis

Figure 21 displays an XPS spectrum of Sample No. 487, which shows carbon (C) at 285 eV, nitrogen (N) at 400 eV, oxygen (O) at 520 eV, chromium (Cr) at 580 eV, and iron (Fe) at 710 eV. The relative amounts are 0.474 C, 0.096 N, 0.286 O, 0.114 Fe, and 0.03 Cr. Iron and chromium are contaminants within the film--a result of sputtering from the aperture plate mounted between the ion beam and the sample. XPS does not measure the hydrogen content in the films, which is known to exist in the films in significantly large quantities. Therefore, the relative concentrations of the above elements provide only a general ratio among those elements.

Figure 22 is the XPS spectrum from Sample No. 487 after sputter cleaning for 10 min. The grey regions indicate where the indicated electrons from the particular elements appear. The relative amounts are 0.56 C, 0.118 N, 0.14 O, 0.145 Fe, and 0.037 Cr. Comparison to the amounts present in Figure 21 shows some removal of oxygen contamination, an indication that oxygen is absorbed only on the surface of the sample. The relative concentrations of iron and chromium did not change, indicating that these elements are present throughout this film in a uniform concentration.

### 5.8.2 RBS and ERS Analysis

RBS and ERS were performed on as-deposited (non-heat-treated) as well as heat-treated GIC and Si samples (see Table 13 on p. 79). RBS was used to determine the elemental composition of carbon and heavier elements, while ERS was utilized to determine the hydrogen content in the films. For calculating the number of carbon and nitrogen atoms in each film, the ratio of C:N was taken from the RBS data, and then the carbon and nitrogen atoms were added in that ratio until the energy of the edge of a simulated spectrum matched the energy of the edge in these data. An inherent or systematic error is associated with not knowing the stopping power of

the film. However, the associated error is less than 10%. The error due to statistical fluctuations in the nitrogen data is slightly greater than this, particularly when the nitrogen content is significantly less than the carbon content. For hydrogen, the number of hydrogen atoms can be determined by measuring the area under the peak for protons in the ERS spectrum. The error associated with this number is less than 10%. Figure 23 is a typical RBS spectrum of a sample and the estimated quadratic fit utilized to subtract the background from film analysis. The area of the resulting peaks is then calculated and the ratio of C:N determined.

Figure 25 depicts an RBS spectrum performed on Sample No. 487, in direct contrast with an XPS spectrum displayed earlier.

The RBS spectrum in Figure 19 typifies a sample with a median film thickness, determined to be

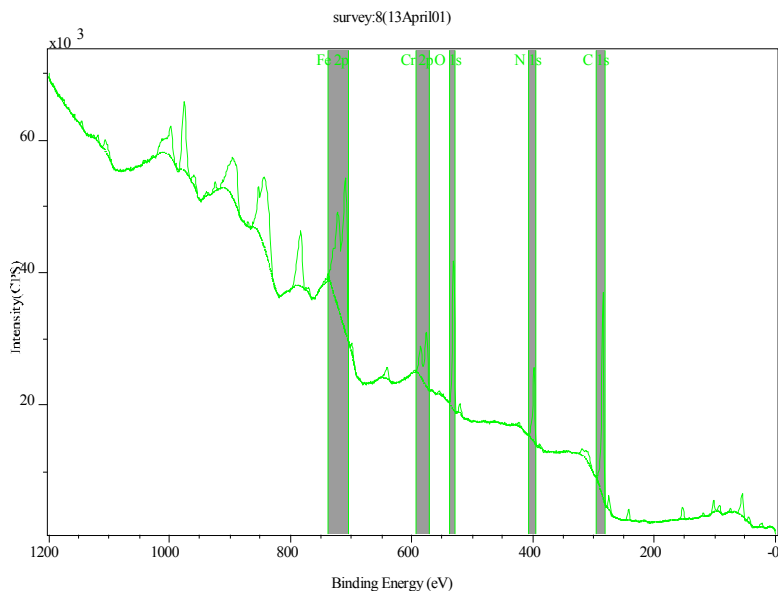


**Figure 22. XPS Spectrum of Sample No. 487 after Sputter Cleaning for 10 min.**

$1.93 \times 10^{18}$  atoms/cm<sup>2</sup>. Argon is visible in this film; and at a slightly higher energy, evidence of some iron contamination can be observed. Shown in Figure 24 is the RBS spectrum for Sample No. 515, which at  $8.96 \times 10^{18}$  atoms/cm<sup>2</sup> is significantly thicker than Sample No. 505. Because of the thickness, the peaks for each element are broader, and the nitrogen peak clearly overlaps the carbon peak. Shown in Figure 26 is the RBS data from Sample No. 517, which is typical of the thinnest samples, with a thickness of  $2.02 \times 10^{17}$  atoms/cm<sup>2</sup>. For this spectrum the width of the elemental peaks is equal to the resolution of the system. In other words, the film is so thin that a negligible energy loss occurs as the alpha particles pass through. However, the range of thicknesses was not important, and the films appear to be uniform as a function of depth, as determined by RBS.

### 5.8.2.1 Film Density

From the total number of carbon, nitrogen and hydrogen atoms in the films, it is possible to calculate an areal and volumetric density for the films. The accuracy of the volumetric density is poor and may contain as much as a 50% error since the region where film thickness was measured does not correspond with the exact location where the number of atoms was measured. However, volumetric densities of approximately 2 g/cc are typical for hydrogenated DLC films. Therefore, volumetric densities calculated for  $CN_x$  films can be assumed to be comparable. The accuracy of areal densities and the fractions of carbon, nitrogen and hydrogen are reliable to within 20%, with nitrogen being the least reliable measurement.

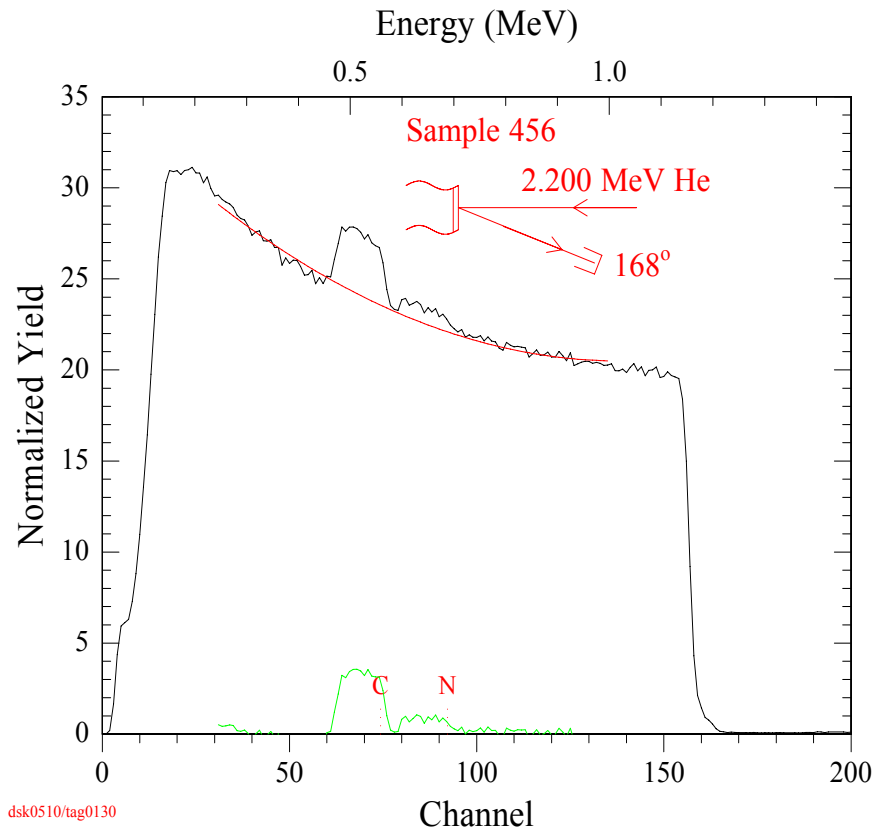


**Figure 23. RBS Data from Sample No. 456. The black line is the data and the red line is a quadratic fit to the background under the carbon and nitrogen peaks. This is then subtracted from the data, and the result is in green.**

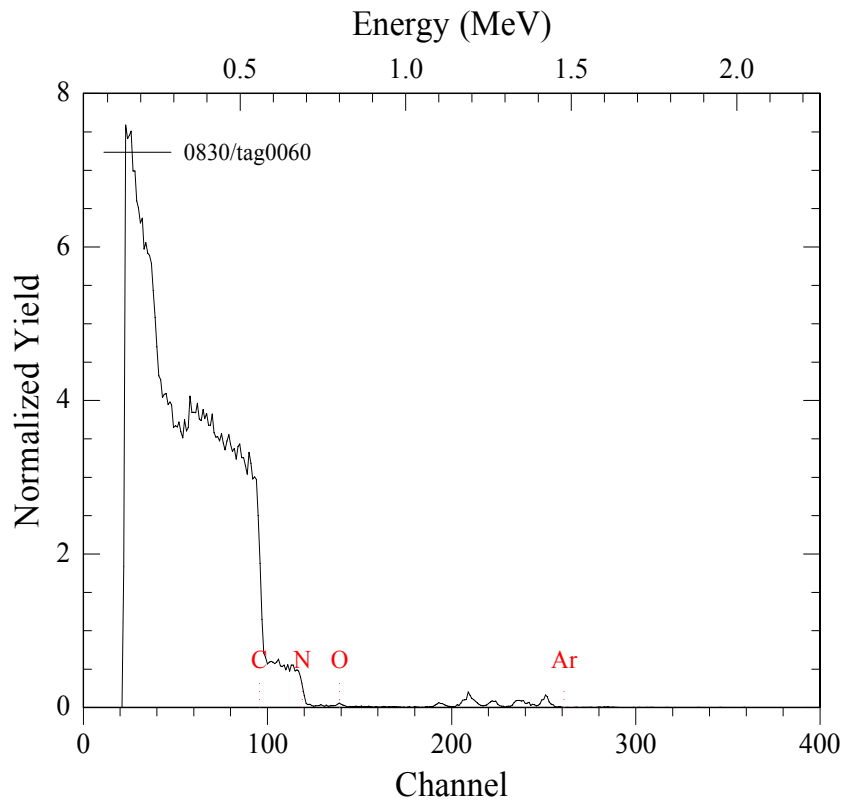


**Figure 24. RBS Data from Sample No. 515, Demonstrating Thick Film.**

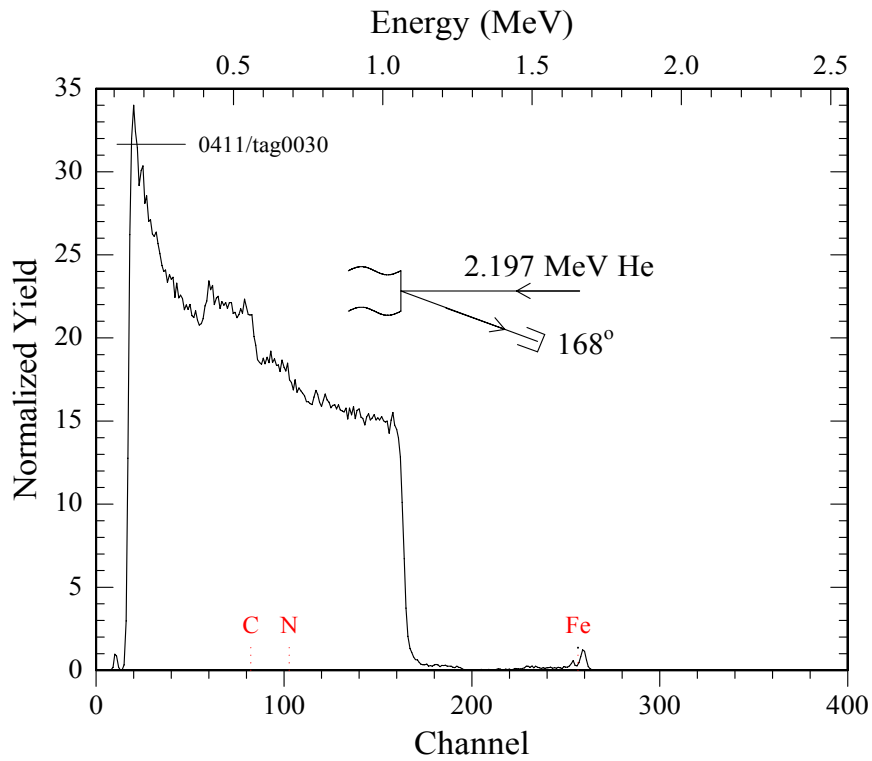


**Figure 25. RBS Spectrum of Sample No. 487.**

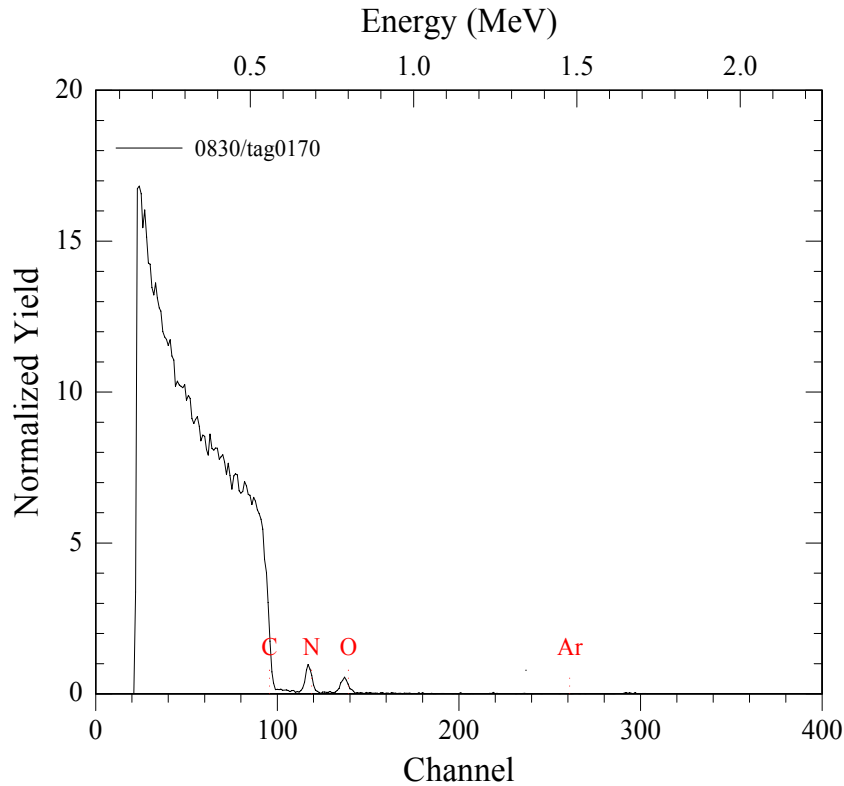


**Figure 26. RBS Data from Sample No. 517, Demonstrating Thin Film.**

### 5.8.2.2 *Single-Ion-Beam Film Composition*

For single-ion-beam deposition of  $CN_x$  film, various methane and nitrogen gas mixtures were utilized. This resulted in  $CN_x$  films with hydrogen concentrations as high as 35% and low nitrogen concentrations. Figure 27 graphically depicts the nitrogen concentration of single-ion-beam deposited films as a function of the  $N_2/CH_4$  gas ratio for three different ion-source parameters and illustrates nitrogen concentrations maximizing at 15% for three deposition conditions. The concentration of nitrogen appears to be almost independent of ion-source conditions, which is typical for film-growth conditions when a single-ion-beam configuration is utilized.

**Figure 28** shows the concentration of hydrogen in the films. The effect of ion energy on the hydrogen concentration appears to be dramatic at low nitrogen fractions of the input gas mixture. Comparing Figure 27 and Figure 28 shows that at the point where the nitrogen concentration peaks, the hydrogen level for the 500 V films reaches a minimum. However, it reaches a maximum for the 100-V films. Clearly, the energy of the arriving ions is playing a major role in trapping hydrogen but is not influencing the trapping of nitrogen to the same extent or by the same mechanism. The likely mechanism for trapping hydrogen is that at higher acceleration energies and low nitrogen concentrations (corresponding to higher methane concentrations), the molecules fragment on impact and the energy carried by hydrogen ions/atoms is sufficient to penetrate to a depth where it can be trapped. As the nitrogen concentration increases, the energy

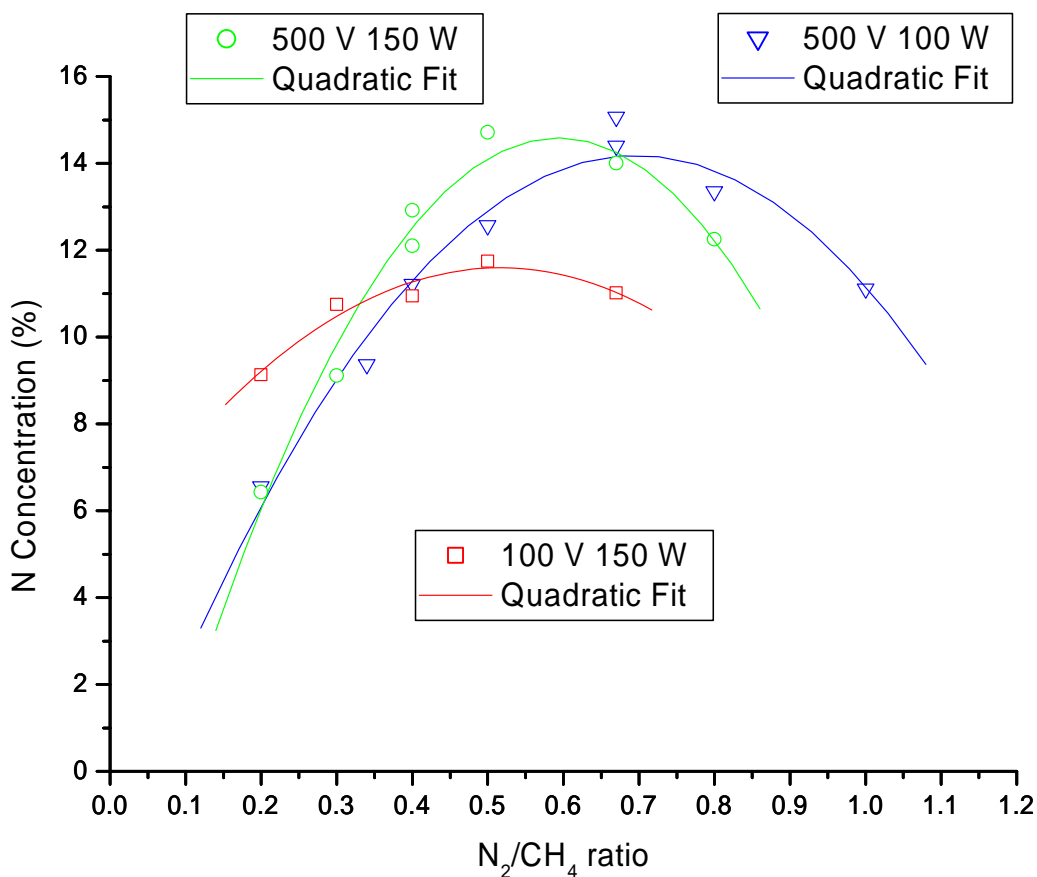


**Figure 27. Nitrogen Concentration in Films as Function of Input Gas Mixture for Three Ion-Source Operating Conditions.**

of the nitrogen ions/atoms reduces the quantity of trapped hydrogen atoms. At low acceleration energies, the molecules have less energy and are less likely to fragment on impact. As the nitrogen-methane ratio increases, the film growth rate peaks, increasing the hydrogen concentration. As this ratio is further increased, etching occurs and the hydrogen concentration is reduced by fragmentation induced from the energy imparted from the excess of nitrogen ions/atoms.

**Figure 29** shows that the amount of material deposited in each film varies with ion-source energy and is weakly dependent on the rf power in the source. This, combined with the concentration of nitrogen and hydrogen in the films, indicates that a  $N_2/CH_4$  ratio higher than 0.6 is not effective at either depositing thick films or adding more nitrogen.

For this set of runs (Nos. 505-524), the carbon concentration ranged from 49.5 to 64.5%, nitrogen from 6.4 to 15%, hydrogen from 22.6 to 33%, and oxygen from 0.2 to 5.8%. The nitrogen to carbon (N/C) ratio ranged from 0.1 to 0.26. The hydrogen-to-carbon (H/C) and hydrogen-to-nitrogen (H/N) ratios ranged from 0.35 to 0.7 and 1.7 to 5, respectively.

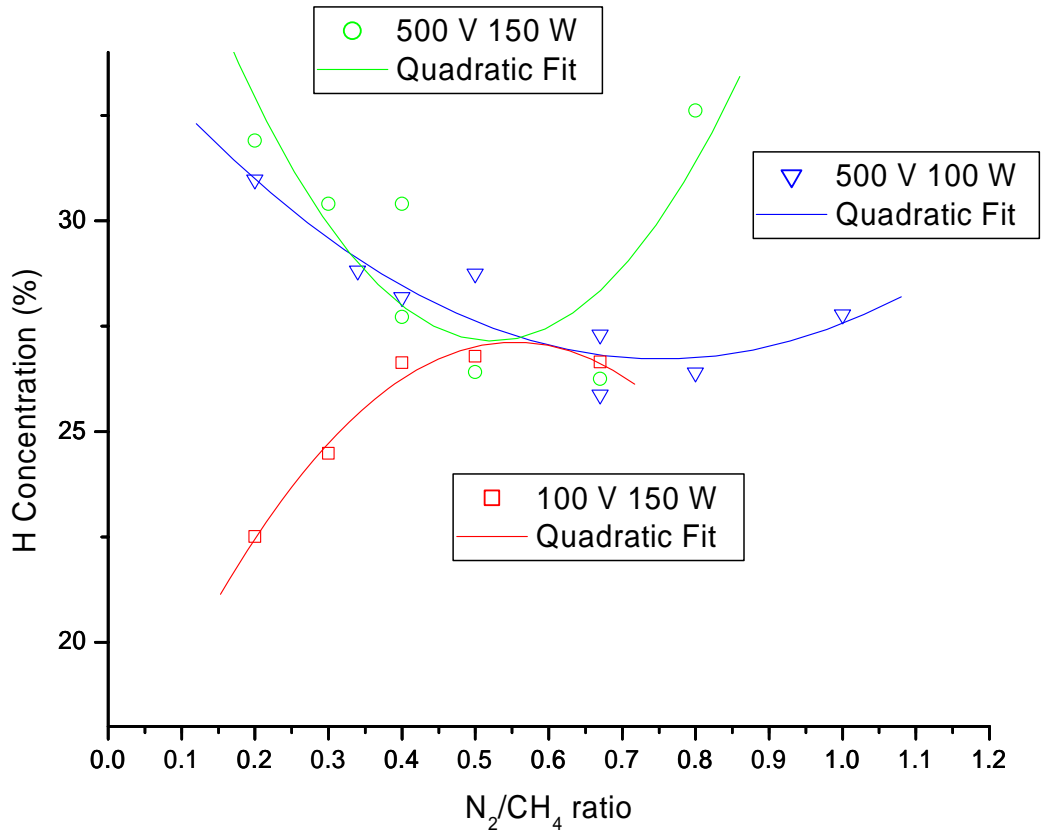


**Figure 28. Hydrogen Concentration as Function of Input Gas Mixture and Three Ion-Source Operating Conditions.**

A conclusion that may be drawn from the analysis of single-ion-beam deposition is that the films contain very little nitrogen and high concentrations of hydrogen, which is not surprising since the source-gas mixture is almost all hydrogen and films of DLC contain similar amounts of hydrogen when deposited from pure methane. The amount of nitrogen in the mix does appear to affect the nitrogen content. However, based on data on the deposition rate as a function of nitrogen fraction of the input gas mixture, it is not possible to achieve films with nitrogen concentrations greater than 20%, as evidenced by the deposition rate of  $CN_x$  falling to zero when the mixture reaches 50%  $N_2$ . The effect of rf power on the film composition does not appear to play a major role.

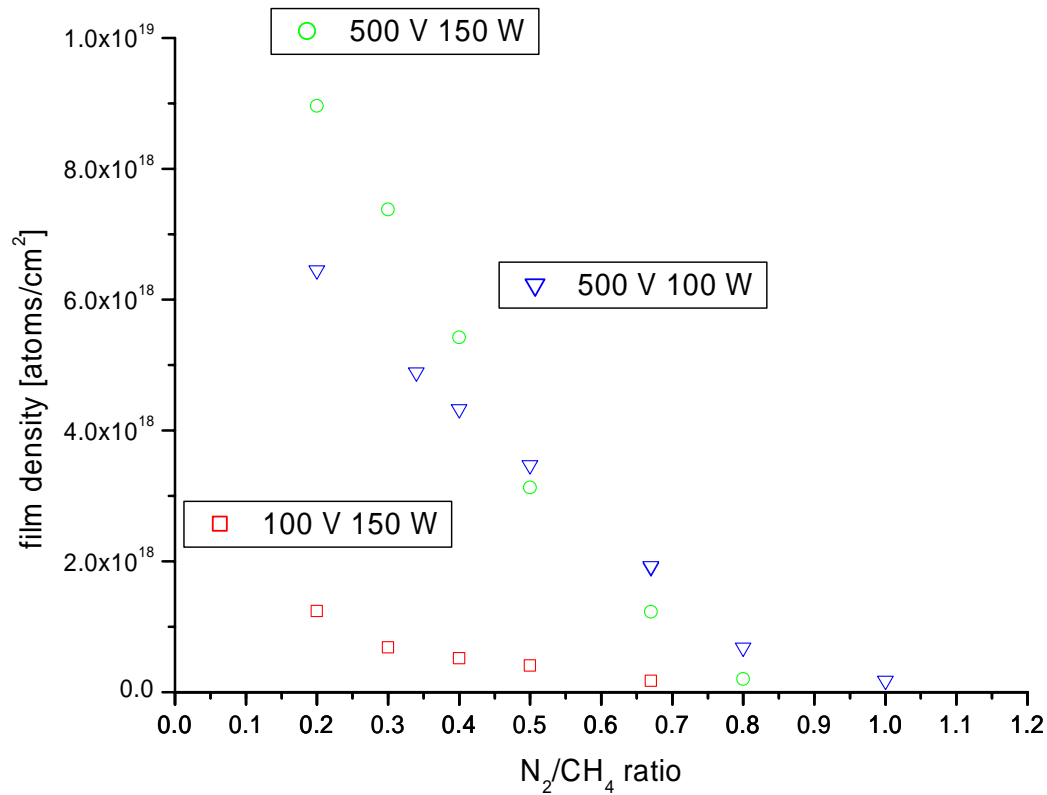


**Figure 29. Density of Films as Function of Input Gas Mixture for Three Ion-Source Operating Conditions.**

### 5.8.2.3 Dual-Ion-Beam Film Composition

A 3-cm ion source was installed to sputter a carbon target, while the 20-cm ion source was used as a nitrogen-ion-beam assist. Initial films (Run Nos.573-583) were grown using the 3-cm ion source with argon as the feed gas. These deposited films consisted of carbon (C) in the range 50-77%, hydrogen (H<sub>2</sub>) 13-38%, oxygen (O<sub>2</sub>) 3-6%, argon (Ar) 0.3-2.7%, iron (Fe) 0.1-2.9%, and traces of aluminum (Al), chromium (Cr), and tungsten (W). The H/C ratio ranged from 0.17 to 0.74. Trapped argon in the films comes from the source gas to the 3-cm ion source. The iron and chromium originate from the stainless steel anode and the tungsten from the cathode filament. These carbon-sputtered films ranged from a hard carbon film (H/C = 0.17) to standard DLC samples, whose composition consists of carbon in the range 60-65% and hydrogen in the range 40-35%, respectively.

A second set of conditions was employed with the 3-cm ion source operated with a feed gas of argon, and the 20-cm ion source was added as an ion assist with a feed gas of nitrogen (Run Nos. 584-593). For this deposition set, carbon (C) was in the range 40-59%, nitrogen (N) 17-25%, hydrogen (H) 9-22.3%, oxygen (O<sub>2</sub>) 1.6-9.1%, argon (Ar) 0-1.5%, iron (Fe) 0.05-3.5%, and traces of aluminum (Al), chromium (Cr), and tungsten (W) 0.04-1%. The H/C ratio for these samples ranged from 0.15 to 0.55. The N/C ratio ranged from 0.15 to 0.65, and the H/N ratio

ranged from 0.32 to 3.33. By enhancing the film growth with the 2-cm nitrogen-fed ion assist, the N/C ratio was increased from the range of 0.15 to 0.25 for single-ion-beam depositions to a range of 0.15 to 0.65 for dual-ion-beam depositions using argon-ion-beam-sputtered carbon with a nitrogen-ion-beam assist. This results in a 2.6 increase in the upper range of nitrogen concentration within the film.

Figure 30 shows the elemental concentrations for a third set of samples where nitrogen gas was fed into the 3-cm ion source for reactive sputtering of carbon and nitrogen was fed into the 2-cm ion source for ion-beam-assisted deposition. For this deposition set, carbon (C) was in the range 35-64.5%, nitrogen (N) 23-38%, hydrogen (H) 0.8-17%, oxygen (O<sub>2</sub>) 0-21%, argon (Ar) 0%, and negligible impurities of iron (Fe), aluminum (Al), chromium (Cr), and tungsten (W) 0.0-0.1%. The H/C ratio for these samples ranged from 0.01 to 0.49. The N/C ratio ranged from 0.49 to 0.75, and the H/N ratio ranged from 0.02 to 0.73. Discarding samples with oxygen concentrations greater than 10% narrowed the bands further. For this case, carbon (C) was in the range 48-64.5%, nitrogen (N) 29.5-38%, hydrogen (H) at 0.8-16.4%, oxygen (O<sub>2</sub>) 0-5%, argon (Ar) 0%, and negligible impurities of iron (Fe), aluminum (Al), chromium (Cr), and tungsten (W). The N/C ratio remained the same at 0.49 to 0.75, but the H/C and H/N ratios were reduced to 0.01 to 0.32 and 0.02 to 0.55, respectively.

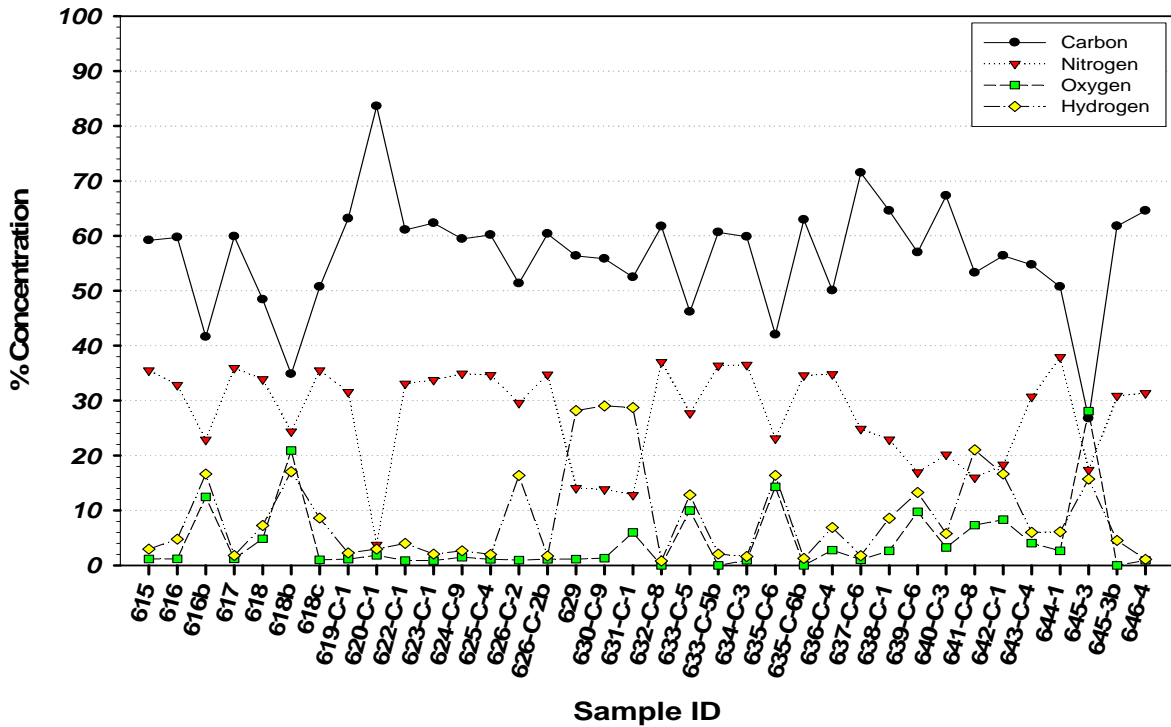


Figure 30. Elemental Composition for Each Run Condition.

Figure 30 also contains compositional elements for samples not included in the above analysis. In Run No. 620, the source was set up to sputter only carbon with argon gas. Run Nos. 629-631 were conducted using the 20-cm ion source for direct deposition and vapors from liquid acetonitrile ( $\text{CH}_3\text{CN}$ ) instead of methane ( $\text{CH}_4$ ) gas. Run Nos. 618b and 645-3 are similar. For Sample No. 618b, the glassy-carbon sample was extremely thin--a typical representation of the film at the surface. Sample No. 645-3 represents the surface of the film, and Sample No. 645-3b is the bulk film. Run Nos. 618 and 618c are thicker films and more characteristic of bulk material, which shows that absorption still occurs at the surface.

Figure 31 shows the N/C, H/C, and H/N ratios for each of these runs. Again, Run Nos. 629-631 are clearly different, as indicated above. Run Nos. 638-642 also show higher concentrations of hydrogen. These runs operated with excessive beam currents, resulting in excessive sputtering of the films. Thus, the films were very thin, showing higher concentrations of hydrogen than are typical in the surface layers of the films.

Table 5 on the following page summarizes the results of single-ion-beam deposition using  $\text{N}_2/\text{CH}_4$  gas mixtures and dual-ion-beam depositions using  $\text{N}_2$  gas for both reactive sputtering and ion-beam assist. For comparison purposes, equivalent properties for  $\beta\text{-C}_3\text{N}_4$  are also shown. The top value indicates the median values for these data, and bracketed numbers indicate the minimum-to-maximum ranges. The carbon-concentration range was not altered significantly; however, the nitrogen content is significantly increased, and the hydrogen content is drastically decreased. For the dual-ion-beam deposition, the film is approaching a composite ratio equivalent to  $\text{C}_3\text{N}_2$ .

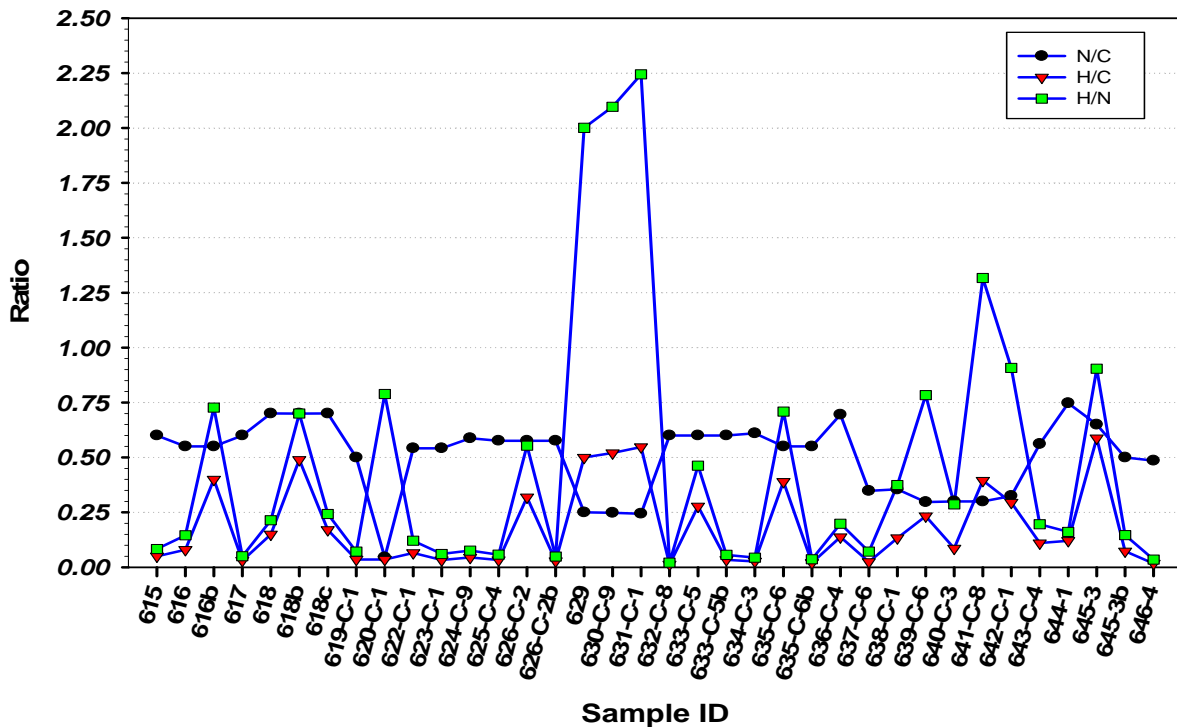


Figure 31. Elemental-Composition Ratios for Each Run Condition.

**Table 5. Compositional Summary for CN<sub>x</sub> Deposition**

	Single Ion Beam (N <sub>2</sub> /CH <sub>4</sub> Deposition)	Dual Ion Beam (N <sub>2</sub> Sputter/N <sub>2</sub> Assist)	β-C <sub>3</sub> N <sub>4</sub>
Carbon Content	58.3% (49.5 – 64.5)	59.9% (48.4 – 64.5)	43%
Nitrogen Content	11.5% (6.4 – 15)	34.7% (29.5 – 38)	57%
Hydrogen Content	27.5% (22.6 – 33)	2.6% (0.8 – 16.4)	0%
N/C Ratio	0.2 (0.1 – 0.26)	0.58 (0.49 – 0.75)	1.33
H/C Ratio	0.47 (0.35 – 0.7)	0.04 (0.01 – 0.32)	0%
H/N Ratio	2.4 (1.7 – 5)	0.08 (0.02 – 0.55)	0%

Both cases indicate that a median of 2.75% is still associated with additional film contaminants. These trace elements arise as a result of several factors. Oxygen in the film occurs either during the deposition from H<sub>2</sub>O fragments or from absorption at the surface upon exposure to air. Moly was found in initial sputtered films, which was associated with the use of moly grids on the 3-cm ion source. Once the grids were replaced with graphite grids, this contaminate disappeared. The silicon (Si), iron (Fe), and chromium (Cr) contamination is suspected to be a result of sputtering from the anode within the 3-cm ion source. Likewise, tungsten (W) originates from the filament associated with the 3-cm ion source.

Hellgren et al. report that growth of CN<sub>x</sub> films with more than 40% nitrogen using chemical vapor deposition (CVD) and physical vapor deposition (PVD) methods is difficult to achieve.<sup>15</sup> As shown in Table 5 above, by using the dual ion-beam-assisted, ion-beam sputter process and controlling the vacuum environment and ion energy, CN<sub>x</sub> films can be created with nitrogen concentrations up to 38% of the total film composition. Assuming no contamination, this would result in carbon at 62% concentration, for an N/C ratio of 0.61. With nitrogen at 38% and an N/C ratio at the maximum of 0.75, this would result in carbon concentrations at 50.7%, leaving a remaining balance of 11.3% associated with other constituents. A similar analysis with N/C at 0.70 results in a carbon concentration of 54.3% and a remaining balance of 7.7% associated with other constituents. As will be discussed in the Electrical Section, it was shown that promising electrical properties occur when hydrogen concentrations in the film are around 8%. This may

<sup>15</sup>N. Hellgren, M. P. Johansson, B. Hjorvarsson, E. Broitman, M. Ostblom, B. Liedberg, L. Hultman, J.-E. Sundgren, "Growth, Structure, and Mechanical Properties of CN<sub>x</sub>H<sub>y</sub> Films Deposited by DC Magnetron Sputtering in N<sub>2</sub>/Ar/H<sub>2</sub> Discharges," J. Vac. Sci. Technol. A 18(5) (Sep/Oct 2000) 2349-2358.

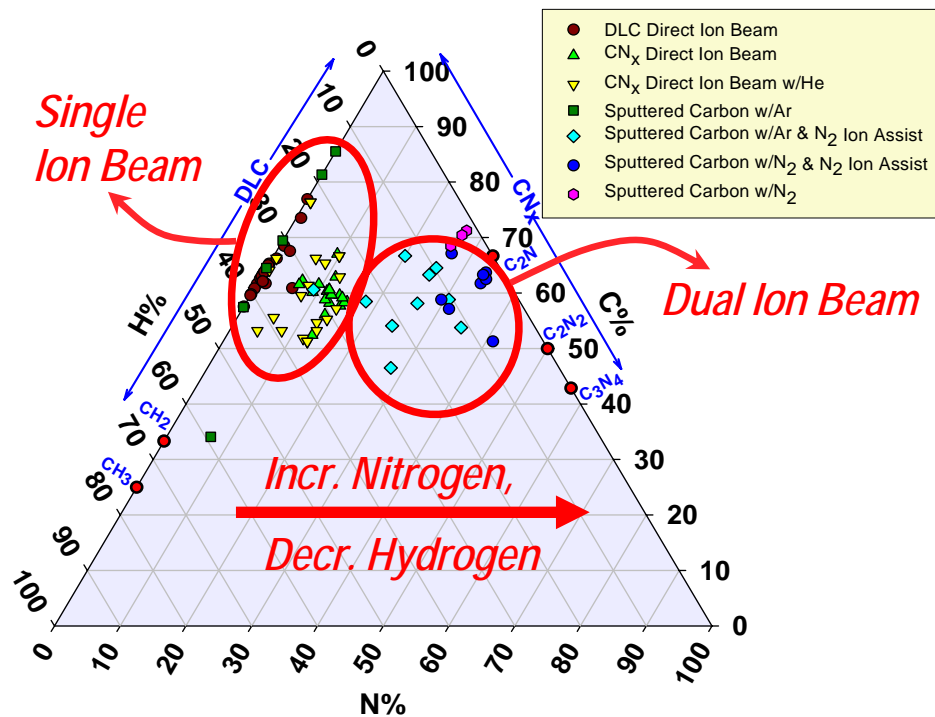


**Figure 32. Three-Axis Compositional Phase Diagram Showing Experimental Results Ranging from DLC to Recently Formed  $CN_x$ .**

indicate that promising films will exhibit elemental concentrations of nitrogen near 38%, carbon near 54.3%, and hydrogen near 7.7%, which would result in a film with a composition near  $C_7N_5H$ . However, this is theoretical since these are amorphous films and defined as containing multiple and random orientations with predominantly  $sp^2$  or  $sp^3$  bonded carbon.

Hellgren et al.<sup>16</sup> reported that a small concentration of hydrogen can have a positive influence on low-temperature-deposited  $CN_x$  films. They note that hydrogen does not appear to promote the formation of crystalline structures or increase the nitrogen concentration. However, it does appear to enhance the film growth rate slightly for low-temperature  $CN_x$  films as well as enhance the density and uniformity of the amorphous structure. They postulate that this is due to enhanced chemical sputtering reactions. They also observed evidence of an increase of  $-C\equiv N$  bonds and think that this bond is providing a disordered disruption to graphitic basal-plane growth, thus minimizing the growth of  $sp^2$  bonded structures.

<sup>16</sup>N. Hellgren, M. P. Johansson, B. Hjorvarsson, E. Broitman, M. Ostblom, B. Liedberg, L. Hultman, J.-E. Sundgren, "Growth, Structure, and Mechanical Properties of  $CN_xH_y$  Films Deposited by DC Magnetron Sputtering in  $N_2/Ar/H_2$  Discharges," J. Vac. Sci. Technol. A 18(5) (Sep/Oct 2000) 2349-2358.

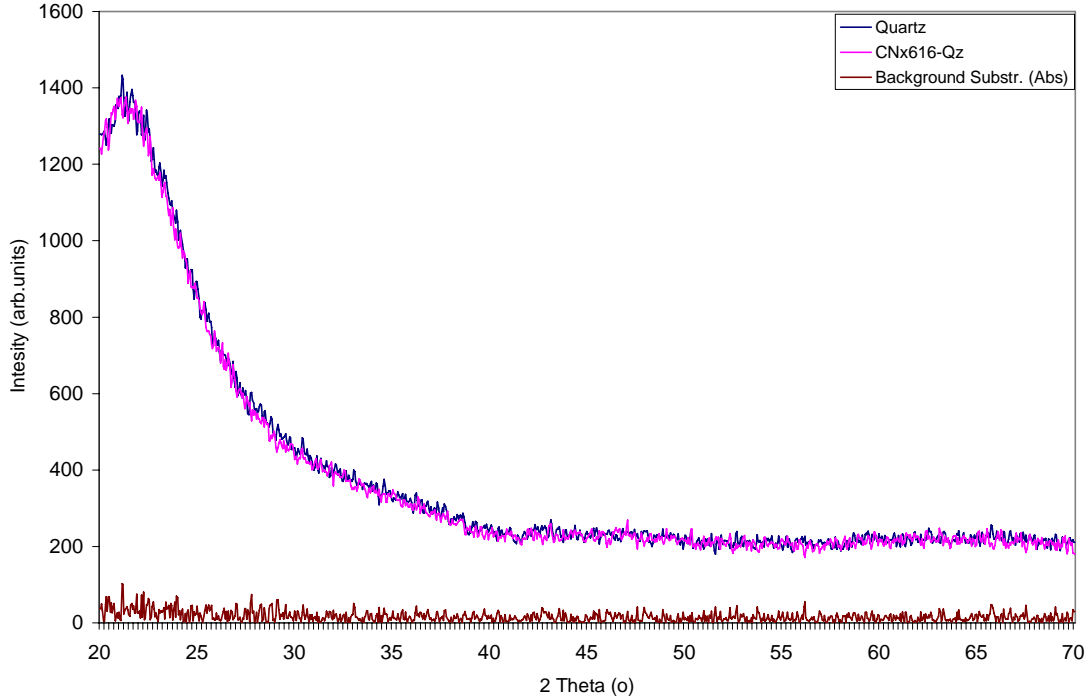


**Figure 33. XRD Data for Sample No. 40210616 on Quartz Substrate. Bare quartz is overlaid for comparison.**

**Figure 32** is a ternary compositional phase diagram for material deposited using various configurations of the system. Previous studies performed on growing DLC material are indicated by experimental results located on the left-hand axis of the graph, as marked. This axis exhibits conditions for DLC with ranges from 0% to 60% for both hydrogen and carbon. The data shifts to the right as nitrogen is incorporated into the film. As indicated, single-ion-beam deposition experiments on growing  $CN_x$  are displayed immediately to the right of the hydrogen axis that displays DLC.

On the right-hand axis, various carbon and nitrogen ratios are displayed for  $CN_x$  films containing no hydrogen. Various crystalline forms of  $CN_x$  are indicated along this axis, with  $C_3N_4$  indicated for the theoretically determined ideal conditions. As the data move from left to right in this diagram, more nitrogen and less hydrogen are incorporated into the film. In the right-hand area of the diagram near the right-hand axis, current dual ion beam experimental conditions are indicated. This diagram shows that improvements in the experimental deposition conditions have created films with compositional properties approaching those of the theoretically determined  $\beta$ - $C_3N_4$ . By increasing the nitrogen and reducing the hydrogen composition, the performance of the  $CN_x$  film is greatly enhanced, bringing it closer to the theoretical properties of  $\beta$ - $C_3N_4$ .

### 5.8.3 X-Ray Diffraction (XRD)

XRD is utilized to determine the crystalline structure of a sample. If the structure is crystalline, then the inter-atomic distance and angles can be calculated. Only one sample was measured.

For this sample, No.616 on a quartz substrate, no evidence was found of any crystalline structure in the film, which would be indicated with peaks located at various angles along the lower curve in Figure 33 (curve is the absolute value of the background subtracted from the sample signal).

### 5.9 IR Transmission

A scan of a  $CN_x$  film deposited on to a NaCl salt crystal shows that  $CN_x$  films can be useful as a hard coating for soft IR transmission optics. NaCl was chosen as the substrate since no absorption peaks in the scanned range are associated with NaCl. This eliminates complications from absorption peaks while scanning the  $CN_x$  film. **Figure 34** shows the transmission characteristics for a bare NaCl salt crystal (top line) and the IR transmission for  $CN_x$  film deposited onto NaCl (middle curve). Various deposition conditions of  $CN_x$  films exhibit slightly different transmission characteristics; however, this graph depicts the general transmission properties. The bottom curve is the percent transmission loss for the  $CN_x$  film only. This curve is the difference between the top two curves. This shows that less than 4% transmission loss occurs due to the  $CN_x$  film.

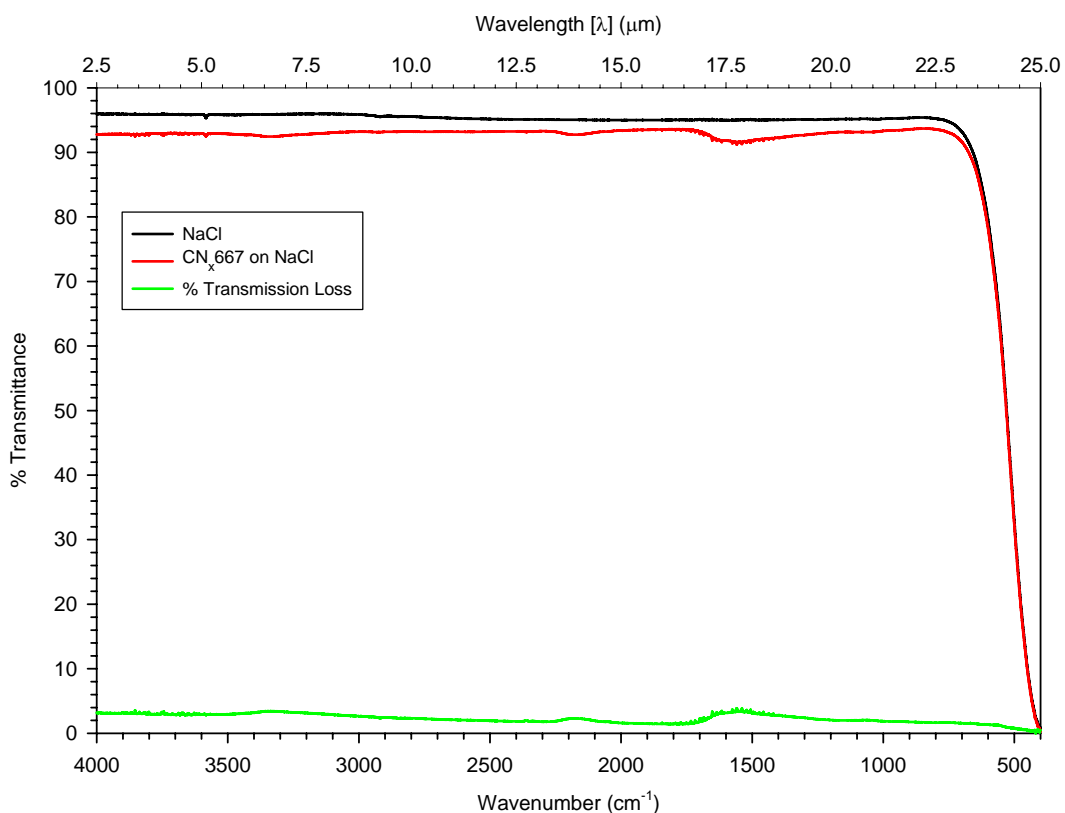


**Figure 34. FTIR Spectrum of NaCl Salt Crystal and  $CN_x$  Film Deposited on NaCl.**

## 5.10 Mass Spectroscopy

Mass spectroscopy was performed in situ during  $CN_x$  film depositions. Figure 35 shows multiple mass spectrum scans that are typical for various runs of  $CN_x$  films. Run Nos. 602, 615, 617, and 618 are dual ion beam deposited  $CN_x$  films, and Run No. 612 is a typical spectrum from a single-ion-beam deposition using  $CH_4$  and  $N_2$ . The largest peak at mass 28 is  $N_2^+$ . The peak at Mass 14 is  $N^+$ . The grouping around Mass 15 is the various fragments associated with  $CH_4$ . Figure 36 shows a zoomed-in view of these same spectra. The point to be made is that for Mass 52, a significant increase is associated with Run No. 618 compared with the other deposition runs. Similarly, Run No. 615, while not so significant as Run No. 618, is also more prominent compared with the other runs. Mass 52 is suspected to be  $C_2N_2$ . It is still uncertain whether this mass makes any contribution to the development of  $CN_x$ ; however, it is noted that Run No. 618 did provide a film with the best electrical properties compared with all other runs. Likewise, Run No. 615 provided electrical properties that were also promising. Table 6 (p. 53) summarizes the run parameters for this data set. The parameters of Run Nos. 602 and 615 are equivalent. For Run No. 618, the rf power was increased from 150 W to 600 W, resulting in an equivalent increase in the ion-beam current. It is possible that the increase in rf power is associated with the increase in Mass 52. These runs were duplicated; however, the electrical properties were not repeatable, indicating that further work is required and that development of quality dielectric films involves elements other than ion-beam-deposition parameters.

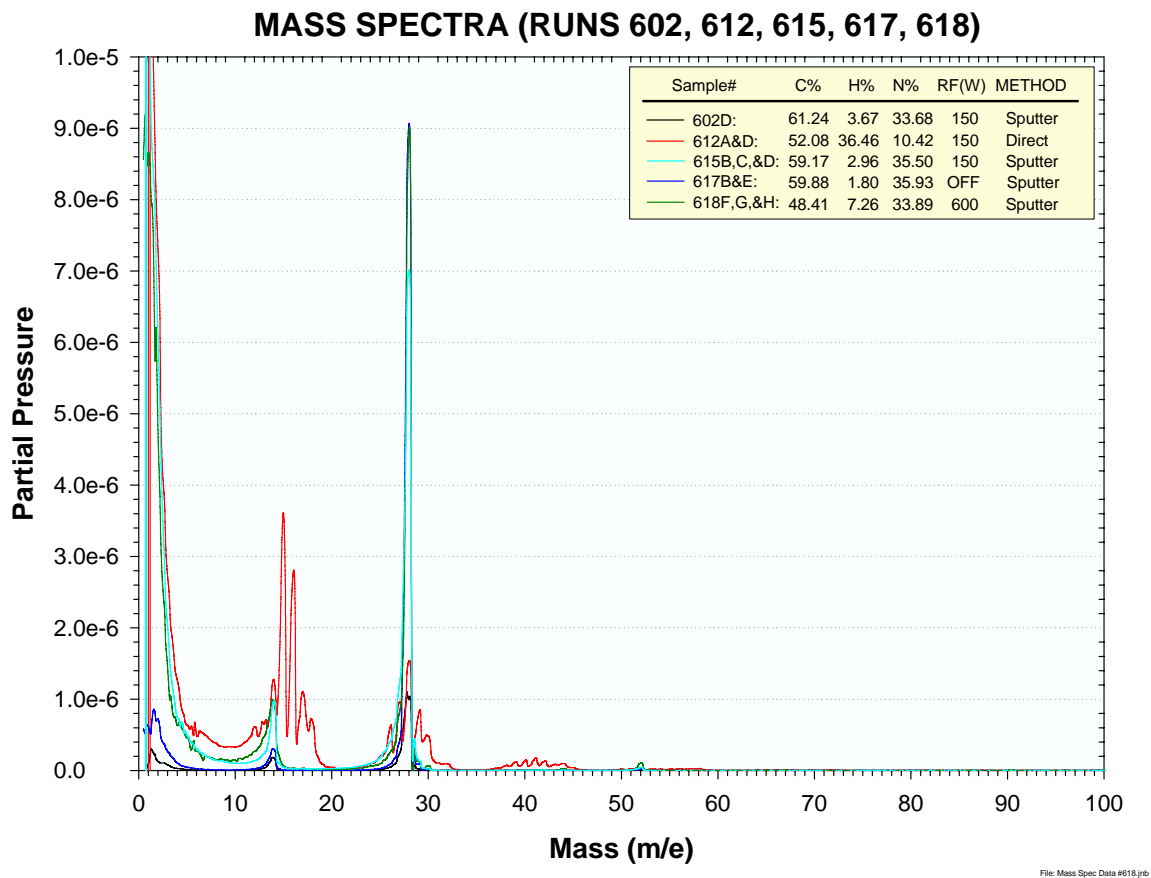
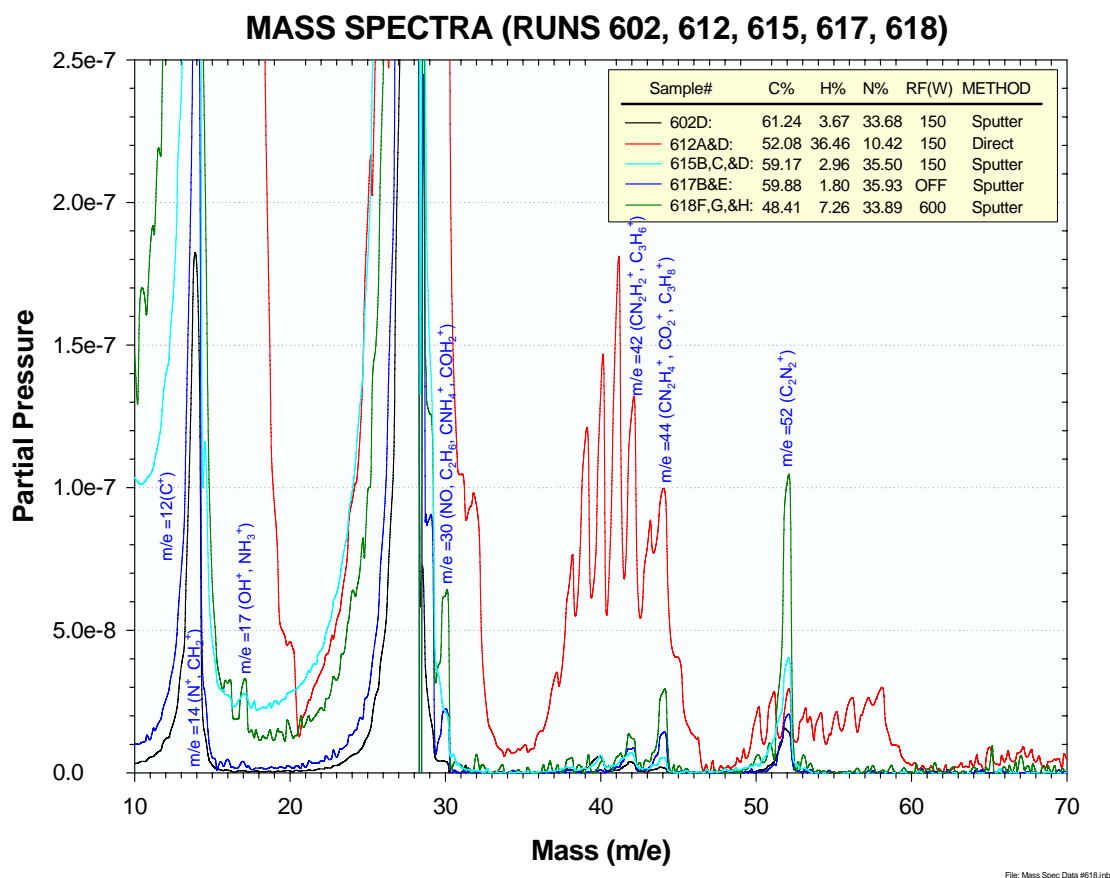


Figure 35. FTIR Spectra of Run Nos. 602, 612, 615, 617, and 618.



**Figure 36. Zoomed-In View of FTIR Spectra for Run Nos. 602, 612, 615, 617, and 618.**

**Table 6. Run Parameters for Mass-Spectrum Graph**

Sample No.	RF Power (W)	Ion Accel. (eV)	Ion Current (mA)
602	150	50	30
615	150	50	30
617	Off	0	0
618	600	50	120

### 5.11 Optical Band Gap

Visible absorption was performed on single-ion-beam deposited samples (Nos. 505-524) to determine the optical band gap of the films using Tauc plots. Table 7 on the following page summarizes the results. The values for these samples range from 0.8 to 3.6, with a median of 2.3 for all samples listed. For comparison, Table 8 on the following page contains the band gap for various common materials. For conductive materials, the band gap is essentially zero. For insulating materials, the band gap is usually defined as being greater than three. Semiconductors lie between these ranges. Several of these samples have a measured optical band gap near and greater than three. One sample measured at 0.8, indicating that this sample would be more conductive.

**Table 7. Optical Band-Gap Measurements**

Sample No.	Optical Band Gap [eV]	Comments
505	2.8	
506	-	Bad Film
507	1.8	
508	2.2	
509	2.8	
510	2.4	
511	-	Bad film
512	3.6	
513	-	Bad film
514	-	Bad film
515		Too much secondary interference in the data. Sample is too thick for UV/VIS
516	3.2	Secondary interference
517	2.4	
518	-	Bad film
519	2.7	
520	1.5	
521	2.1	
522	1.7	
523	0.8	
524	1.2	

**Table 8. Optical Band Gap for Common Materials**

Material	Optical Band Gap [eV]
Diamond	5.2 – 6.4
Silicon	1.14
Silicon Dioxide	8.9
Silicon Carbide	3.03 – 3.28

### 5.12 Electrical Characteristics

Development of  $CN_x$  film for use as a high-temperature dielectric is desired to advance the creation of high-power capacitors. Current capacitor designs are limited by the dielectric. Specifically, commonly used dielectrics are limited to operating temperatures less than 125°C. These capacitor dielectrics are also very poor thermal conductors, which leads to excessive heat build-up within the capacitor as it is being used. To create capacitors capable of delivering large power surges and operating in extremely harsh environments, the dielectric must be able to withstand higher temperatures and conduct the internal heat build-up out to prevent destruction.

The electrical characteristics of the films were determined by developing the flat-plate capacitors mentioned above. These capacitors were tested for 1) capacitance; parallel, series, and equivalent-series resistances, and loss tangent ( $\delta$ ) [dissipation factor,  $D_f$ ] as a function of frequency, and 2) d.c. insulation resistance and breakdown voltage by measuring the d.c. current as a function of voltage ( $I$ - $V$  curves). From these data the dielectric constant ( $\epsilon_r$ ), resistivity ( $\rho$ ), and dielectric strength ( $E_b$ ) were calculated.

Electrical measurements were performed on the majority of the samples; results are tabulated in Table 14 (p. 83) and Table 11 (p. 73) for single- and dual-ion-beam depositions, respectively. Dissipation values ranged from a low of 0.032 to a median of 0.7. Median resistivity values are in the  $10^7$  -  $10^8$   $\Omega$ -cm range, which is considered to be a relatively low range, with a few samples ranging at a high of  $10^{11}$  -  $10^{12}$   $\Omega$ -cm. Dielectric constants are very erratic, ranging from 1.9 to greater than 200. A median range of those samples posted is near 40. The maximum measured dielectric strength was 393 kV/mm, with a median range of all posted samples at 26.5 kV/mm.

Electrical properties were poor for films deposited using single-ion-beam deposition. These films exhibit poor electrical properties, possibly due to the high concentrations of hydrogen displacing the nitrogen by terminating bonds with carbon, thus resulting in films with nitrogen concentrations less than 15%.  $CN_x$  films with low nitrogen concentrations were suspected of exhibiting characteristics comparable to a nitrogen doped DLC film (N-DLC). According to Hoffsass et al.<sup>17</sup> this results in a film that performs poorly as a high-resistivity film. Memming et al., on the other hand, report that nitrogen is not an effective dopant in DLC films.<sup>18</sup> J. Wei et al. report that for  $CN_x$  films with N/C ratios less than 0.40, the electrical properties were mixed.<sup>19</sup> Likewise, Cameron has pointed out that there are “many conflicting conclusions about the effect of nitrogen in the carbon matrix.”<sup>20</sup>

Very few research results have been published on the electrical characteristics of  $CN_x$  films, and only recently have papers on this subject appeared. As evidenced with both single- and dual-ion-beam deposited  $CN_x$  films, electrical analysis to date has been relatively elusive, with conflicting results. Even in papers that do present electrical results, wildly varying data are published, confirming the confounding results. In these papers electrical-resistivity results have ranged from being low<sup>21,22,23</sup> to as high as  $10^{18}$   $\Omega$ -cm<sup>24</sup> and values in between.<sup>25</sup>

---

<sup>17</sup> H. Hoffsass, in “Amorphous Carbon: State of the Art,” ed. S.R.P. Silva et al. (World Scientific 1998), p. 296.

<sup>18</sup> R. Memming, “Properties of Polymeric Layers of Amorphous Hydrogenated Carbon Produced by Plasma-Activated Chemical Vapor Deposition Process I: Spectroscopic Investigations,” *Thin Solid Films* 143 (1986) 279.

<sup>19</sup> J. Wei, “Electrical Properties of Reactively-Sputtered Hydrogenated Carbon Nitride Films,” *Int. J. Nanoscience* 3 (4,5) (2004) 555-562.

<sup>20</sup> D.C. Cameron, “Optical and Electronic Properties of Carbon Nitride,” *Surface Coatings Technol.* 169-170 (2003) 245.

<sup>21</sup> E. Broitman, N. Hellgren, K. Järrendahl, M.P. Johanson, S. Olafsson, J.-E. Sungren, L. Hultman, “Electrical and Optical Properties of  $CN_x$  ( $0 \leq x \leq 0.25$ ) Films Deposited by Reactive Magnetron Sputtering,” *J. Appl. Phys.*, 89(2) (2001) 1184-1190.

<sup>22</sup> V. Hajek, K. Rusnak, J. Vlcek, L. Martinu, S.C. Gujrathi, “Influence of Substrate Bias Voltage on the Properties of  $CN_x$  Films Prepared by Reactive Magnetron Sputtering,” *J. Vac. Sci. Technol. A* 17(3) (May/Jun 1999) 899-908.

<sup>23</sup> E. Broitman, N. Hellgren, J. Neidhardt, I. Brunell, L. Hultman, “Electrical Properties of Carbon Nitride Thin Films: Role of Morphology and Hydrogen Content,” *J. Elec. Mat.* 31(9) (2002) L11-L15.

### 5.12.1 n-Type Dopants

One of the objectives of the Ph.D. study that was conducted by Asghar Kayani, a graduate student at Ohio University, was to investigate the effect of adding nitrogen to DLC films to determine whether small quantities could dope these films, comparable with other members of Group 15 (old Group 5) of the periodic table, which can be utilized as n-type dopants for amorphous or polycrystalline silicon or germanium. The result of this work was that as soon as nitrogen was added in significant amounts (>1%) to DLC films, the band gap fell, as shown in Figure 37. The graph shows the compensating effect of hydrogen as found in most semi-conducting materials. It also shows that the presence of nitrogen introduces traps in the band gap, shown by the increasing width of the Urbach tail.

Thus, the general result appears to be that adding nitrogen leads to a conducting material--but not through a simple doping mechanism in which there is a defined activation energy but through the insertion of states into the gap at many different levels. The underlying message is that the C-N bonds are not in the form needed for the insulating material predicted by the theory of Liu and Cohen,<sup>26</sup> and that some other parameter need to be changed before those bonds can be created-- either the precursor material or the temperature of the substrate during the deposition. These could be avenues for future work.

These effects are noticed with the  $CN_x$  films deposited with low nitrogen concentrations from single-ion-beam deposition. Based on this, the effects of nitrogen-doped DLC films (n-DLC) exhibit similar effects to nitrogen-doped silicon (n-Si). However, Liu and Cohen's theory for  $\beta-C_3N_4$  is based on a substitution model that is derived by replacing silicon with carbon in a  $Si_3N_4$  ceramic lattice. Just as the properties of  $Si_3N_4$  are insulating, as opposed to conductive n-Si, the same can be inferred for  $CN_x$ . It is anticipated that a transitional phase occurs, converting from a low-nitrogen conductive phase to a higher nitrogen insulating phase. The point where the nitrogen concentration is sufficiently increased to convert to this phase is still undetermined because of the extreme complexities of  $CN_x$  films.

---

<sup>24</sup> M.i Aono, S.i Nitta, "High Resistivity and Low Dielectric Constant Amorphous Carbon Nitride Films: Application to Low-k Materials for ULSI," *Diam. Rel. Mat.* 11 (2002) 1219-1222.

<sup>25</sup> C. Popov, L.M Zambov, M.F. Plass, W. Kulisch, "Optical, Electrical and Mechanical Properties of Nitrogen-Rich Carbon Nitride Films Deposited by Inductively Coupled Plasma Chemical Vapor Deposition," *Thin Sol. Films* 377-378 (2000) 156-162.

<sup>26</sup> A. Y. Liu, M. L. Cohen, "Structural Properties and Electronic Structure of Low-Compressibility Materials:  $\beta-C_3N_4$ ," *Phys. Rev. B* 41 (1990) 10727.

### 5.12.2 Hydrogen Concentration

As shown earlier, single-ion-beam deposited samples contain higher concentrations than samples deposited using dual-ion-beam deposition. The resistivity of the original CN<sub>x</sub> films deposited using the single-ion-beam method were relatively low. The thermal stability for these films was, however, improved over that of DLC samples. But RBS and ERS studies showed that the degradation of the films beyond 400°C was due to hydrogen liberation. To combat these problems, the dual-ion-beam deposition method was utilized to increase the nitrogen concentration. This method also resulted in a significant reduction in the hydrogen concentration. CN<sub>x</sub> films were produced with hydrogen concentrations as low as 1%. The thermal stability of these films was improved from 400°C to 600°C. The electrical properties of these films, however, did not improve significantly.

A comparison of a few samples is shown in Table 9 below, where Run No. 618 is compared with select runs of dual-ion-beam-deposited samples. This chart indicates that complete removal of hydrogen from the CN<sub>x</sub> composite may not be desirable. High hydrogen concentrations also show lower values of resistivity, which possibly indicates that a hydrogen concentration between 5 and 10% may be required to enhance the resistivity of CN<sub>x</sub> films. It is currently unknown whether this hydrogen is needed to passivate the film surface by terminating dangling bonds or whether it is uniformly dispersed throughout the CN<sub>x</sub> matrix, terminating graphitic chains and enhancing *sp*<sup>3</sup> bonding.

As indicated by this table, the best film is achieved with a high N/C ratio (0.70) and a hydrogen concentration around 8.6%. Once development of CN<sub>x</sub> film can be predictably controlled, it may be possible to fine tune the dielectric constant to a suitable range, as indicated by comparing Run Nos. 615 and 618. Both samples exhibited suitable resistivities. The variances in hydrogen between these films may result in the observed variance with the dielectric constant. The shortfall is the equivalent reduction in the dielectric strength (*E<sub>B</sub>*).

**Table 9. Hydrogen Concentrations and Properties of Select CN<sub>x</sub> Depositions**

Sample No.	H%	N%	C%	N/C	D <sub>f</sub>	Resistivity (Ω-cm)	<i>E<sub>B</sub></i> (kV/mm)	ε <sub>r</sub>
618	8.62	35.51	50.72	0.70	0.09	5.27x10 <sup>11</sup>	393	2.34
615	2.96	35.50	59.17	0.60	0.08	1.17x10 <sup>11</sup>	123	10.70
617	1.80	35.93	59.88	0.60	0.13	4.92x10 <sup>7</sup>	11.17	73.65
605	3.57	23.57	71.43	0.33	-	-	-	-

### 5.12.3 Capacitance

An LCR HP4284A capacitance meter with Signatone micro-positioner probes, M/N S-725, was used to measure through-the-film capacitance, parallel resistance, equivalent series resistance (ESR), and the dissipation factor (D<sub>f</sub>) of developed capacitors as a function of frequency.

As indicated earlier in the Capacitor Development Section, each capacitor device has 16

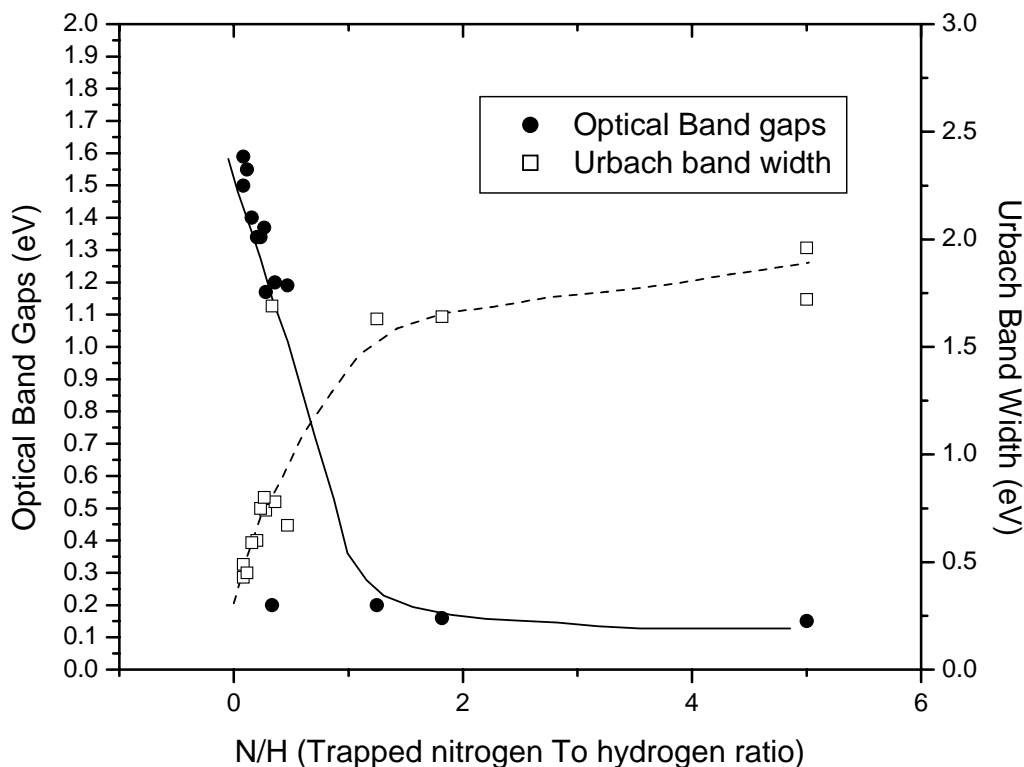


**Figure 37. UV-visible Optical Band-Gap Data as Function of Nitrogen-to-Hydrogen Ratio.**

individual capacitor pads (3 mm in diameter) for testing. Problems due to shorts from pinholes, contamination, etc., can cause failure on some or all of the pads. Therefore, not every pad is suitable for testing. The electrical-data tables indicate the values measured from each pad and the number of pads that could be electrically tested.

Capacitors were originally tested with and without a dark shroud to determine whether films were photosensitive. These tests were also performed in both open-air and argon environments to determine whether environmental interactions are taking place. No improvements were noted in capacitance measurements using either the dark shroud or an argon environment.

All capacitance tests were performed on as-deposited  $CN_x$  substrates at room temperature. Further studies are required to observe the effects of capacitance on heat-treated substrates at elevated temperatures.

Each capacitor in the array of 16 was initially tested at 1 kHz for a quick check of the device. Capacitors that were not shorted and with dissipation factors less than 5 were then scanned from 20 Hz through 1 MHz, measuring the capacitance, dissipation factor, parallel resistance, and equivalent series resistance (ESR).

#### 5.12.4 Dissipation

The dissipation factor ( $D_f$ ) or loss tan ( $\delta$ ) is the ratio of the resistance to the net reactance of a capacitor. High  $D_f$  values indicate a dielectric with large power absorption. This can be defined as the ratio of the power loss within the dielectric material to the total power transmitted through the dielectric, i.e., the fraction of energy lost to the dielectric that occurs when the capacitor is charged. Power absorption within the dielectric can result from energy lost to polarization or to resistance leakage. In either case, this absorbed power results in heat being generated within the capacitor. An ideal capacitor would have a  $D_f$  of zero, but this is not possible in a real device. In a.c. power capacitors, dissipation losses can result in very high temperatures.

Another characteristic of the  $D_f$  is that as the value increases, the capacitance of the device increases. It is usually very desirable to have a capacitor with as large a capacitance value as possible. Therefore, in real devices the tradeoff is between maximizing the  $D_f$  to increase the capacitance and minimizing the  $D_f$  to diminish dielectric losses and subsequent heating.

The dissipation factor varies relative to the applied frequency; therefore, normally the dissipation factor is specified at the fixed frequency of 1 kHz. For reference, capacitors with dielectrics made with Teflon have a dissipation factor around  $2e-4$ , and for ceramic capacitors it is around 0.005. The best DLC films to date had a dissipation factor in the range 0.1 - 0.001.

Normally  $D_f$  is the first-look guide in determining whether the dielectric film is good, since a high dissipation factor would indicate that a considerable amount of energy is lost to resistances in the film and device; this would cause excessive heating of the device and premature failure.

It would be desirable to have  $D_f$  values that are less than 0.01. However, because of the low quality of capacitor devices tested, capacitors with  $D_f$  values less than or equal to 5.0 were chosen as an initial starting point during film development. Table 14 summarizes the measured electrical properties for single-ion-beam-deposited  $CN_x$ . The values vary widely from a high of 4360 to a low of 0.02. For Run Nos. 505-572, the low was only 0.31. Run Nos. 609-614 optimized the best run conditions from previous depositions. Clearly the results for these runs show improvement over those for the initial parameter set.

Table 11 (p. 73) summarizes the various electrical properties obtained for dual-ion-beam deposited samples. This table indicates the number of capacitor pads per sample with  $D_f$  values that are less than 1.0, along with low and median values for the dissipation and calculated dielectric constant. As shown, capacitor pads for the majority of these samples have  $D_f$  values that are less than 1.0.

A few of these samples exhibit  $D_f$  values that are much greater than 1.0. These samples are thought to exhibit pinholes, contamination, or a graphitic microstructure rather than a random amorphous structure within the dielectric.

Figure 38 is a plot of the median range of  $D_f$  for the majority of sample substrates. Most of these samples have a  $D_f$  value less than 0.4, with only two samples having a  $D_f$  value greater than 1.0. In Table 10 on the following page the low, median, and high values for each of the four substrate types are tabulated. This table clearly shows that AlSi, AlGI, and Si substrates produced samples

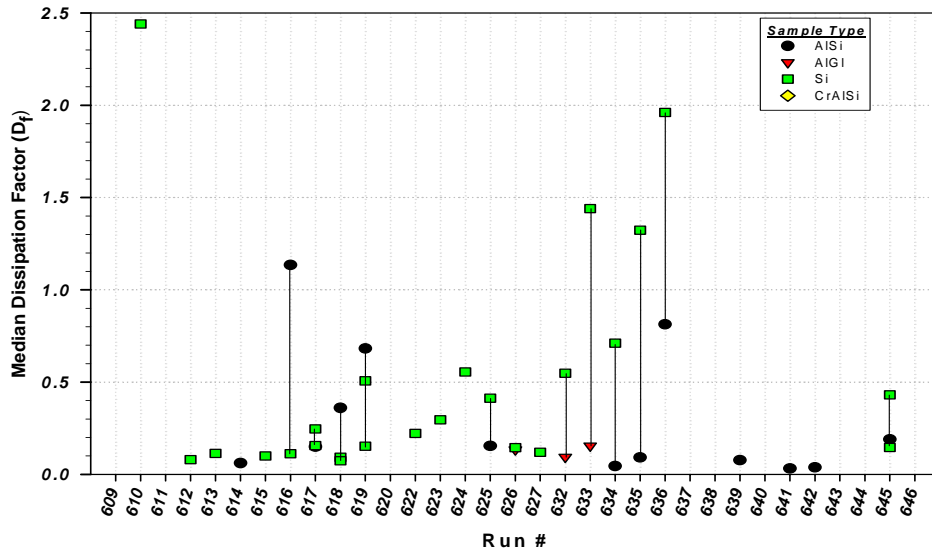


**Figure 38. Median  $D_f$  Values for Various Substrate Materials.**

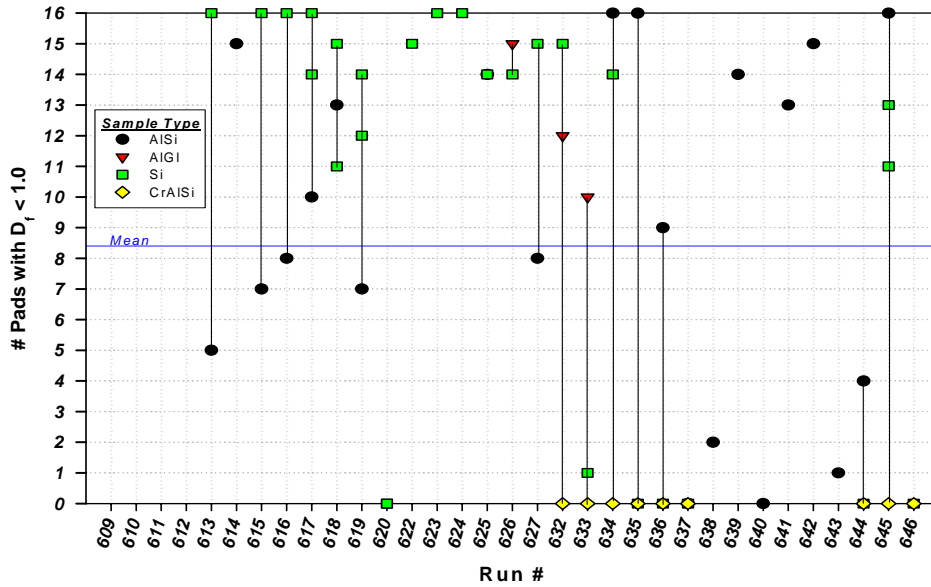
with acceptable low and median  $D_f$  values. There were no acceptable  $D_f$  values for CrAlSi substrates. Adhesion properties on CrAlSi substrates were excellent; however, it appears that the  $CN_x$  film microstructure is unacceptably altered when deposited onto chromium.

Figure 39 shows the total number of capacitor pads per sample for this same set of samples with  $D_f$  values less than 1.0. The maximum number of capacitor pads per sample is 16. Again, this is separation into the four substrate types clearly shows that none of the CrAlSi samples had  $D_f$  values less than 1.0, while most of the AISi, AlGI, and Si substrates had  $D_f$  values less than 1.0. The mean of this set is slightly more than one-half of the total number of capacitor pads. This improvement in the total number of acceptable capacitors over original film development indicated that even though  $CN_x$ -film electrical properties were currently poor, improvements were being made in stabilizing the growth conditions.

In summary, the dissipation values indicated in Figure 38 for dual-ion-beam deposition are generally better than those indicated in Table 14 for single-ion-beam deposition. However, the subset from Run Nos. 609-614 shows that dissipation factors are comparable with those achieved using dual ion beam deposition. However, hydrogen concentrations in these films are greater than that from dual ion beam deposition. If all other factors are equal, the dual ion beam process yields dielectrics that are more thermally stable than those for the single-ion-beam process.

**Table 10. Dissipation-Factor Summary**

	AISi	AlGI	Si	CrAlSi
Low	0.03	0.09	0.07	333.30
Median	0.75	0.16	0.41	969.72
High	2450.00	699.75	680.40	1890.00



**Figure 39. Capacitor Pads with  $D_f$  Values Less Than 1.0.**

### 5.12.5 Resistivity

The resistance of a capacitor is dependent upon its geometry and the dielectric material. It is defined as:

$$R = \rho \frac{L}{A} \quad (1)$$

where  $R$  is the resistance,  $\rho$  is a unit of proportionality called the resistivity,  $L$  is the length of the resistor (in this case the thickness of the film), and  $A$  is the area of the capacitor.

Additionally, from Ohm's law, we have:

$$V = I \cdot R \quad (2)$$

where  $V$  is the applied voltage,  $I$  is the current, and  $R$  is the resistance. With this, we can calculate the resistivity of the dielectric from:

$$\rho = \frac{V \cdot A}{I \cdot L} = \frac{V \cdot A}{I_{(\text{leakagecurrent})} \cdot d_{(\text{dielectricthickness})}} \quad (3)$$

If the dissipation factor of a capacitor was sufficient to continue measurements, then an IR measurement was performed and a capacitance check performed as a function of frequency.

Resistance of a dielectric film is dependent upon thickness, capacitor area, the dielectric, and temperature. Resistivity is used as a standard-unit measurement that is calculated from the d.c. resistance of a material, the film thickness, and the cross-sectional area. This is used as a

standard value for comparisons since it is independent of the geometry of the capacitor.

The insulation resistance (IR) measurement involves placing a fixed voltage on the capacitor, measuring its resistance (R) and leakage current as a function of time, and checking for stability (commonly referred to as *I-V curves*). This leakage current is used along with the applied voltage to calculate the resistivity of the dielectric.

A Keithley 6517A high-resistance meter was used to measure current as a function of voltage (*I-V curves*) to determine the d.c. insulation resistance ( $R_{ir}$ ) and the breakdown voltage ( $V_b$ ) of samples with acceptable  $D_f$  values.

Ideally, no leakage current would be present, which would result in an infinite amount of resistance; this is impossible in the case of real devices. However, the higher the resistance and the corresponding resistivity, the better the dielectric, resulting in less current leakage and corresponding heat generation through the dielectric.

For practical applications, the resistivity value must be considered. For capacitors that are designed for long-term power storage, this value should be as high as possible. However, for pulse-power applications, lower resistivity dielectrics can be considered, but the losses due to lower film resistivities must be insignificant compared to the power extraction of the device. This ensures that heating due to those losses will be minimal compared to that due to power conduction.

Table 11 summarizes the low, median, and high resistivities of the various depositions for dual-ion-beam deposition. The median resistivity values are in the  $10^7 - 10^8 \Omega\text{-cm}$  range, with those samples exhibiting reasonable electrical properties and achieving resistivities in the  $10^{11} - 10^{12} \Omega\text{-cm}$  range. Figure 40 displays the highest resistivity achieved during each sample run for the four types of substrates coated. The mean value achieved was  $2 \times 10^9 \Omega\text{-cm}$ , with a median of  $2 \times 10^8 \Omega\text{-cm}$ . Although these values are lower than desired, they do show that a dielectric can be formed. While those samples in the  $10^7 - 10^8 \Omega\text{-cm}$  range would be considered low-quality films, they are sufficiently reasonable to permit initial development for use as an a.c. pulse-power dielectric. These low values--the result of contamination, microstructure, or morphology of the film--indicate that additional effort is required to improve the quality of the films. Since a capacitance value for these capacitor devices was obtained, pinholes in the film are assumed to be very minimal or sufficiently small that direct shorting of the capacitor plates is not occurring. However, microscopic pinholes or pinholes that were subsequently coated can create localized voltage field effects, which can lead to weak spots in the dielectric and can reduce the resistance and corresponding resistivity of the film. This effect can occur when microscopic graphite contamination particles are embedded in the film during the growth process. Surface contamination, which is coated over during metal-plate deposition or removed prior to metallization and leaves a depression in the dielectric, can also create localized voltage field effects.

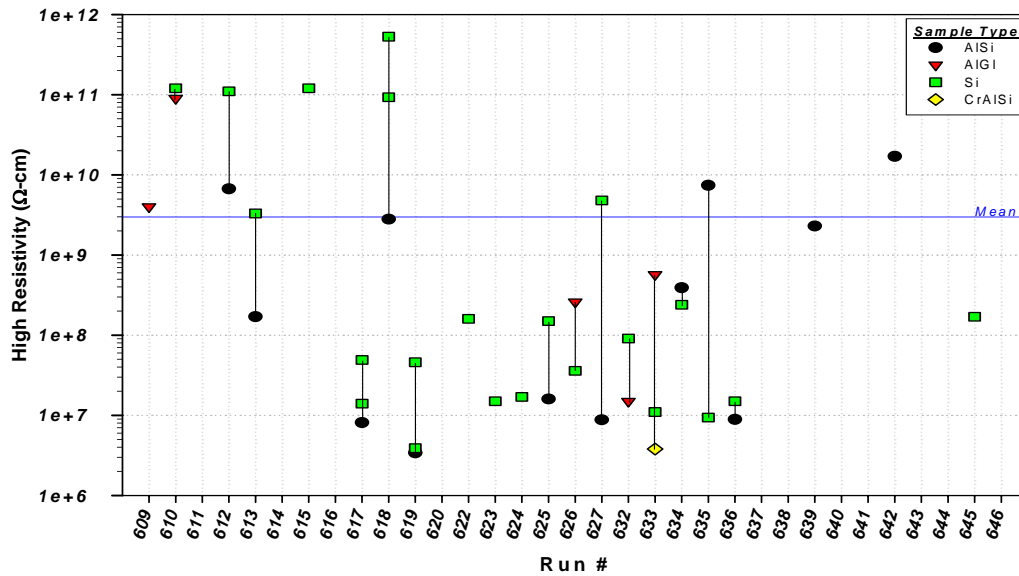


**Figure 40. Highest Resistivities Achieved under Each Run Condition.**

Resistance can also be low because of the microstructure of the film. Indications are that the ideal growth boundary conditions are in a narrow range. Outside this range, conditions appear to be more conducive to growing a graphitic structure with a greater number of  $sp^2$  bonds. This bonding structure is more conductive than  $sp^3$  bonding.

The morphology (surface-roughness characteristics) of the film evolves, in part, from the microstructure of the film. The greater the surface roughness of the dielectric, the greater the quantity of localized discharge points to induce breakdown within the dielectric. Film-growth conditions must be such that the surface roughness of the dielectric is minimized.

Baker et al.<sup>27</sup> reported that deposition temperature is a critical parameter when trying to achieve high-resistivity material, and they went as low as 80°K to achieve insulating-like material and went down to 140°K to exceed  $10^9 \Omega\text{-cm}$ . While it does appear that deposition temperature is a factor, it is evident from the data reported here that a fair number of samples were measured to be in the  $10^9 \Omega\text{-cm}$  range. The temperatures for these depositions ranged from 50 to 100°C (323 to 373°K).

Hellgren et al.<sup>28</sup> suggest that differences in growth conditions drastically affect the microstructure of the  $CN_x$  films. While the conditions under which these samples are grown should produce an amorphous  $CN_x$  structure, it is possible that a rather large percentage is graphitic structure, which creates lower resistivity values. Therefore, fine tuning of the growth parameters while maintaining tighter control of the film growth may reduce the amount of  $sp^2$ -bonded graphitic crystallization within the amorphous  $CN_x$  matrix.

<sup>27</sup>M. A. Baker, P. Hammer, C. Lenardi, J. Haupt, W. Gissler, "Low-Temperature Sputter Deposition and Characterisation of Carbon Nitride Films," *Surface and Coatings Technology* 97 (1997) 544.

<sup>28</sup>N. Hellgren, M. P. Johansson, B. Hjorvarsson, E. Broitman, M. Ostblom, B. Liedberg, L. Hultman, J.-E. Sundgren, "Growth, Structure, and Mechanical Properties of  $CN_xH_y$  Films Deposited by DC Magnetron Sputtering in  $N_2/Ar/H_2$  Discharges," *J. Vac. Sci. Technol. A* 18(5) (Sept/Oct 2000) 2349-2358.

### 5.12.6 Voltage Breakdown

In a capacitor, the energy is stored in the electric field across the insulating or dielectric layer between the plates of the capacitor. This dependence can be seen from the equation for the energy density (energy per unit volume) in the dielectric of a capacitor which is given by:

$$u = \frac{1}{2} \epsilon_r \epsilon_o E^2 \quad (4)$$

where  $\epsilon_r$  is the dielectric constant or relative permittivity of the dielectric material,  $\epsilon_o$  is the permittivity of free space, and  $E$  is the electric-field strength in the dielectric. To achieve a high-energy-density capacitor for pulsed-power applications, the energy storage of the capacitor must be maximized. This can be accomplished by either increasing the dielectric constant or increasing the electric breakdown strength. It is more desirable to have a dielectric material with a high electric-breakdown strength than a material with a high dielectric constant because of the dependence of the energy density on the square of the electric field. Additionally, materials with a high dielectric constant tend to have lower electric-breakdown strengths and, hence, support lower electric fields than materials with low dielectric constants.<sup>29</sup>

Voltage-breakdown measurements are utilized to determine the maximum voltage that can be applied to the dielectric without creating a cascading breakdown effect within the film. To accomplish this, voltage is increased over time, and the corresponding leakage current is measured, resulting in an  $I$ - $V$  curve. The voltage-breakdown point is considered to occur at the inflection point where the leakage current increases dramatically--commonly referred to as the “knee”-point voltage in the  $I$ - $V$  curve. As in the case of resistance, this value is dependent upon the separation between the two conductive plates. To standardize this value, independent of the separation distance, dielectric strength ( $E_b$ ) is usually reported. This value is

$$E_b = \frac{V_{\max}}{L} \quad (5)$$

where  $V_{\max}$  is the maximum voltage (breakdown voltage or “knee”-point voltage), and  $L$  is the separation distance between the conductors--in this case, the film thickness. The maximum energy density ( $u_{\max}$ ) of a capacitor is determined from  $E_b$ , the dielectric strength calculated at the breakdown voltage point.

As stated previously, Table 11 summarizes the dielectric strength of the samples measured for dual ion beam deposition. Values for the single-ion-beam depositions for Run Nos. 609-614 are also included in this table. The three samples in Figure 41, Figure 42, and Figure 43 display  $I$ - $V$  curves with various voltage-breakdown results. Each curve represents an individual capacitor device that passed all other tests performed on the total of 16 capacitor devices on the sample. Figure 41 shows  $I$ - $V$  curves that would be desirable. For this sample,  $V_b$  was 41 V for the best capacitor device. With a film thickness of 1763 Å for this sample, the breakdown voltage results

---

<sup>29</sup> M. Rabuffi, G. Picci, “Status Quo and Future Prospects for Metallized Polypropylene Energy Storage Capacitors,” IEEE Trans. Plasma Sci. 30 (2002) 1939.

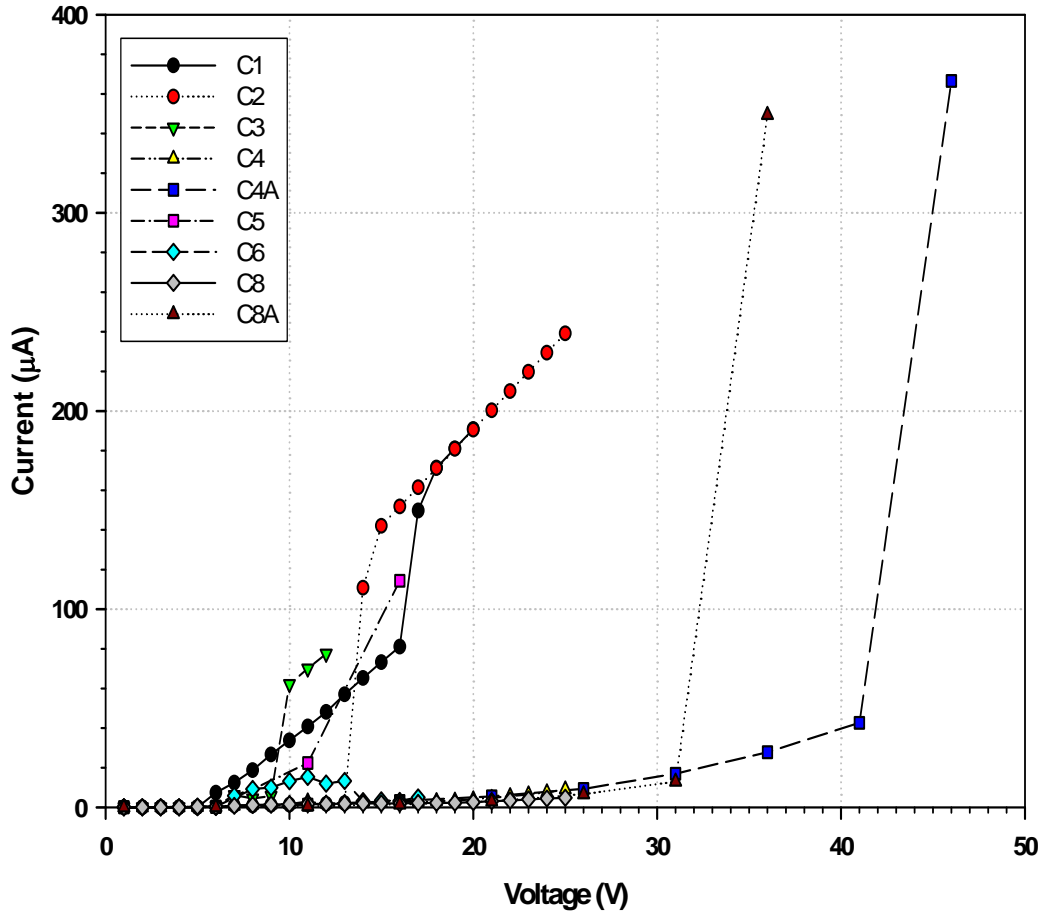


**Figure 41. Voltage-Breakdown Graph. Sample film thickness of 1763 Å, with maximum voltage breakdown of 41V, which yields dielectric strength of 233 kV/mm.**

in an  $E_b$  of 232.6 kV/mm. Figure 42 shows a sample with linear I-V curves. This indicates a resistive dielectric, which is undesirable and not suited for use as a dielectric. Figure 43 displays a sample with a mixture of resistive dielectrics and dielectrics with lower losses. These curves indicate two inflection points. At the second inflection point, the leakage current did not drop, which would indicate a “clearing” of the dielectric. However, the rate of increase in current was reduced, while the voltage increased. This is a possible indication that voltage “stressing” of the device may clear small local imperfections, allowing the capacitor device to achieve a higher voltage breakdown. All of these tests were performed using a single I-V cycle. By repeating the I-V cycle, it is possible that a noticeable improvement may occur in the voltage-breakdown strength of the samples. With this sample  $V_b$  was 26.6 V, and the film thickness was 1978 Å, resulting in an  $E_b$  of 134.5 kV/mm.

The best voltage breakdown strength was measured to be 393 kV/mm. The median of all high values was 26.5 kV/mm. As seen in the table, the values have very broad range, again indicative that further research is required to develop a set of samples with a more defined range.

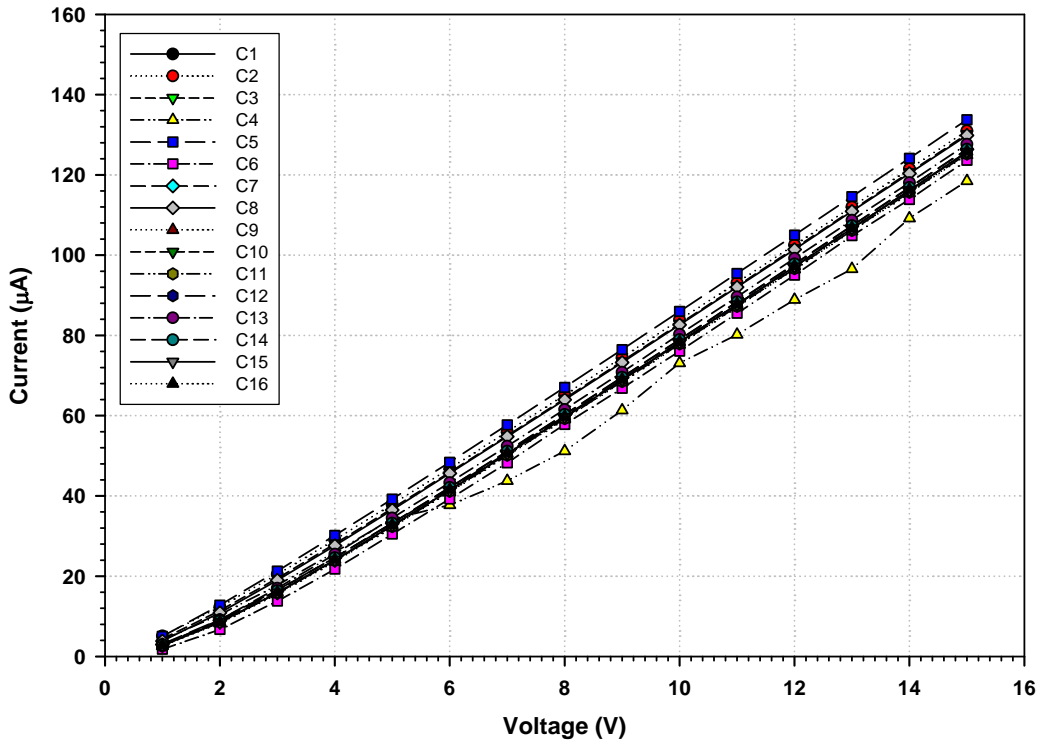


Figure 42. Sample Displaying Linear I-V Curve--Characteristic of Resistor.

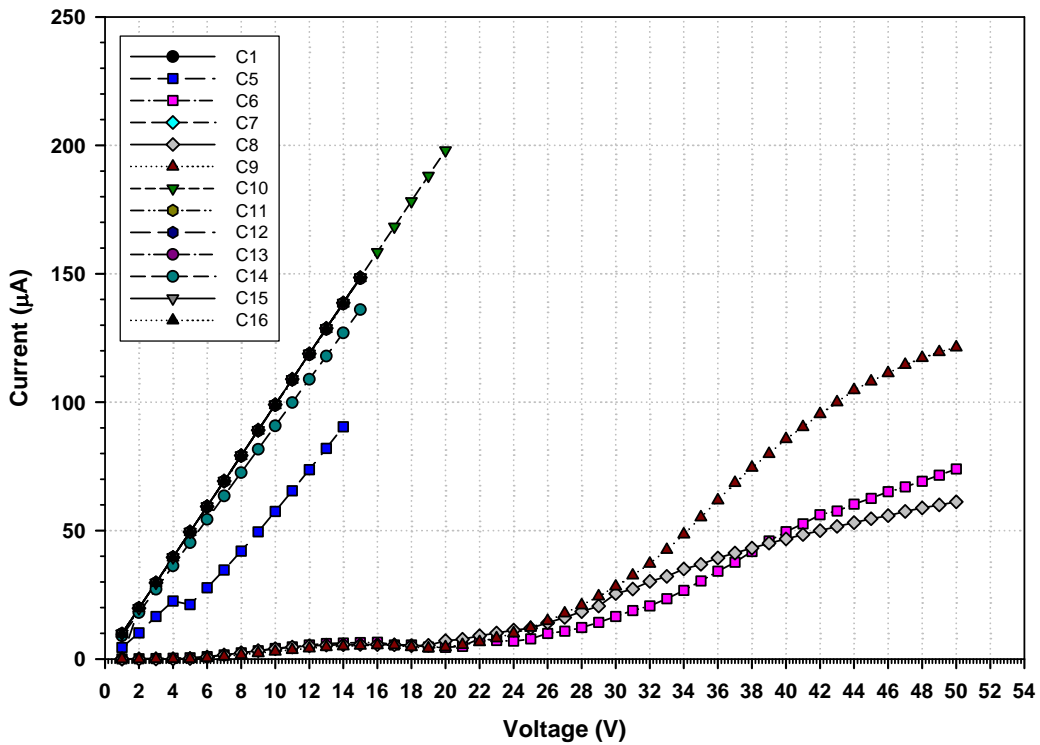


Figure 43. Sample Demonstrating Plateau in Breakdown, Indicating Possible Clearing Effect. Voltage breakdown is near 26 V with film thickness of 1978 Å;  $E_b$  is 131.4 kV/mm.

### 5.12.7 Dielectric Constant

The dielectric constant of a material is calculated from the capacitance equation

$$C = \frac{\epsilon_o \epsilon_r A}{d} \quad (6)$$

where  $C$  is the capacitance,  $\epsilon_o$  is the permittivity constant of free space ( $8.854 \times 10^{-12}$  F/m),  $\epsilon_r$  is the relative dielectric constant of the material,  $A$  is the area of a capacitor plate, and  $d$  is the separation distance between plates (in this case, the film thickness).

Looking at the equation with regard to capacitance, it can be seen that for a fixed geometry on a capacitor, the greater the dielectric constant, the greater the capacitance value. The benefit would be to create a capacitor with a very large capacitance value in a physically small package. However, as mentioned earlier in the Voltage Breakdown Section, extremely high dielectric materials, in general, are not able to withstand so intense an electrostatic field as a low dielectric material, resulting in lower voltage breakdown strengths. Therefore, for high-powered pulse capacitors, it is more desirable to have a low dielectric, even though higher dielectrics result in higher capacitor values.

Additionally, materials with high-valued dielectrics are ionically bonded--polarized. On the other hand, most low-valued dielectrics are covalently bonded. Highly polarized films lose a great deal of energy in aligning these polarized molecules. Therefore, ionic bonding results in films being more susceptible to dielectric absorption, where long-term polarizations or interfacial effects of the material absorb energy. Once polarized, these molecules prefer to remain in that orientation. Therefore, after a capacitor is discharged, residual energy remains within the dielectric, making extraction of all of the energy required for a high-powered pulse capacitor more difficult.

Table 11 contains a summary of the calculated dielectric constants for the various dual-ion-beam depositions performed along with Sample Nos. 609-614, which were deposited using the direct single-ion-beam method. This table shows that the calculated dielectric constants ( $\epsilon_r$ ) range from 0.1 to greater than 200. Predicted values for the theoretically determined crystalline forms are 3.2 for  $\beta$ - $C_3N_4$ <sup>30</sup> and 7.7 for  $c$ - $C_3N_4$ <sup>31</sup>. The few values published for amorphous  $CN_x$  have dielectric constants ranging from 1.9 to 11.0.<sup>32,33,34</sup> For the values in Table 11, approximately 25% of the median dielectric values are less than 11.0. Nearly one-half of the low dielectric values are less than 11.

Based on assumptions derived from diamond and diamond-like carbon (DLC), the dielectric value for carbon nitride is anticipated to be in the range 1.5 - 6.0. Approximately 12% of those

---

<sup>30</sup> H. Yao, W. Y. Ching, Phys. Rev. B 50 (1994) 11231.

<sup>31</sup> S.-D. No, L. Ouyang, W. Y. Ching, I. Tanaka, Y. Koyama, and R. Riedel, Phys. Rev. Lett. 83 (1999) 5046.

<sup>32</sup> M. Aono, S. Nitta, Diamond Related Mat. 11 (2002) 1219-1222.

<sup>33</sup> W. Kulisch, C. Popov, and L. Zambov, New Diamond Frontier Carbon Technol. 11(1) (2001) 53-76.

<sup>34</sup> M. Aono, T. Katsuno, S. Nitta, T. Itoh, S. Nonomura, Mat. Res. Soc. Symp. Proc. 593 (2000) 493-498.

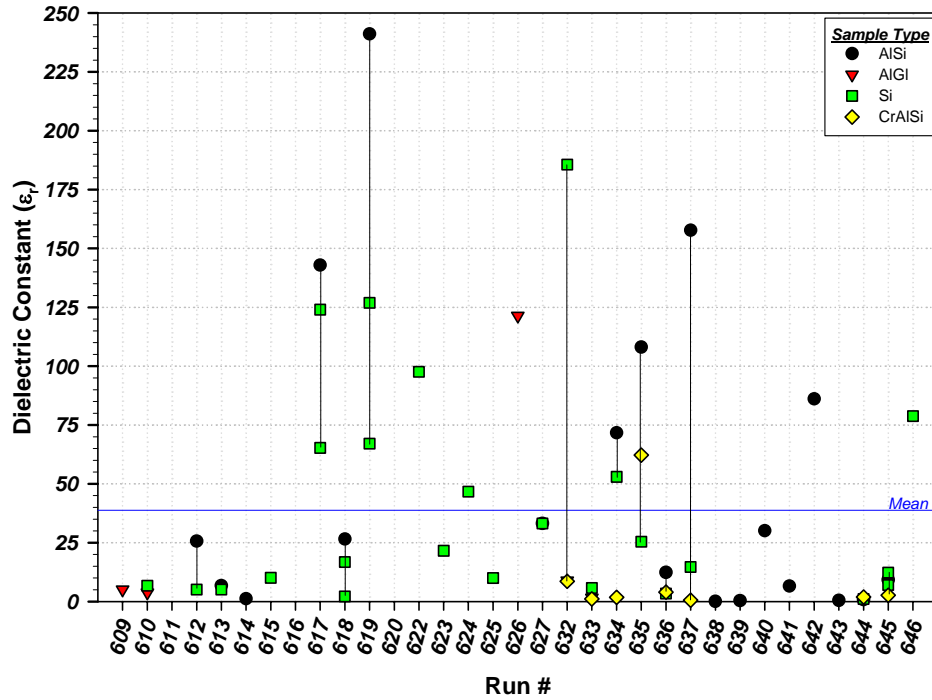


**Figure 44. Values of  $\epsilon_r$  for Each Sample Condition and Substrate Type.**

values posted for median dielectric constant are less than 6.0, and nearly one-third of the posted low dielectric values are less than 6.0.

The value of  $\epsilon_r$  for the samples developed is difficult to calculate accurately because of the variances in measured capacitance values. Figure 44 contains plots of  $\epsilon_r$  for the various dual-ion-beam-deposited  $CN_x$  substrates. While the first indicator of poor values would be the dissipation factor, it is clear from the previous discussion that a fair number of samples had acceptable  $D_f$  values. Again, the variance in capacitance values could result from several factors: 1) film microstructure and bonding, 2) film morphology, 3) surface conduction across the device, 4) poor electrical contact, and 5) film pinholes and contamination (thought to be the least significant problem since these conditions would contribute to higher  $D_f$  values).

For the dielectric-constant values that were determined (as shown in Table 11), a fair number were within the published 1.9 - 11 range, with the median of the low values being 10.1. Sample No. 618 is the optimum overall sample that was created, displaying a breakdown voltage of 393 kV/mm and a median  $\epsilon_r$  of 2.34.

According to the above equation, the variables to this value are the area of the capacitor, the film thickness, and the capacitance. The error in determining the area of the capacitor is less than 5%. Film-thickness errors in the worst case could be 100% because of sensitivities and difficulties in accurately measuring thin films. However, this error is typically less than 25%. These errors would result in an equivalent percentage increase or decrease in the calculated

dielectric-constant values. While it is possible that the film-thickness values are in error, this would not create a significant change in the calculated dielectric values.

In the case of the capacitance measurement value, the same type of relationship holds--if the capacitance value is doubled, the dielectric constant is doubled, assuming all other values to be constant. But the error in measuring capacitance arises from the  $D_f$  and parallel resistance determined within the film. As the resistance through the film is lowered, the measured capacitance of the film increases dramatically. This leads to the conclusion that a fair number of the  $CN_x$  capacitor devices created had a rather low dielectric resistance, as evident from the resistivity values. The  $D_f$  measurements, however, do not clearly indicate this, with more than one-half of the median  $D_f$  values and nearly 75% of the low  $D_f$  values being less than 1.0.

## 6.0 CONCLUSIONS

Development of  $CN_x$  film is possible using either single ion beam or dual-ion-beam deposition arrangements. RBS and ERS elemental analyses have shown that films can be consistently reproduced with high concentrations of nitrogen and with less than 10.0 at.% concentration of hydrogen using the dual-ion-beam method. For single-ion-beam deposition, nitrogen concentrations peak at 15 at.%, and hydrogen concentrations can range up to 43 at.%--much higher than in the dual ion beam arrangement.

RBS and ERS have revealed a higher concentration of hydrogen at the surface of the film, which is the result of contamination from exposure to the atmosphere. The effects of this contamination on the electrical properties of  $CN_x$  film are unknown. The overall quality of capacitor devices could be improved by performing the complete development of the capacitor under a vacuum environment, without exposing intermediate steps to the atmosphere.

The film-growth rate utilizing the dual-ion-beam arrangement is low, with a mean value of 3.8 Å/min for all samples. Single-ion-beam deposition is more rapid but is still not sufficient for production growth rates and has additional problems associated with low nitrogen and high hydrogen concentrations. Improvements with the system layout and equipment should improve this rate. Deposition rates can be further enhanced by investigating various gases and gas mixtures.

Film adhesion on all substrates utilized (glassy carbon, silicon, aluminum, nickel, chromium, quartz, and 7059 glass) was excellent. While film adhesion and visual quality of  $CN_x$  on chromium were excellent, the electrical properties for this material were very poor. The electrical properties of  $CN_x$  film on aluminum, nickel, and silicon provided a higher level of acceptable values. Nickel is reported to be compatible with  $CN_x$  and warrants further investigation.

Only a limited amount of data has been published on the electrical properties of  $CN_x$ . For amorphous  $CN_x$ , published dielectric values range from 1.9 to 11.0, and resistivities range from conductive to highly resistive. The films created have electrical properties with widely varying values, indicating a current lack of consistent reproducibility. Nevertheless, the devices developed do show promise and further basic research into the development of the film is expected to result in the proper parameters and techniques required to advance  $CN_x$  film development for commercial and military applications.

An initial indicator of electrical quality was the dissipation factor. Values achieved were as low as 0.032, with a median range of all measured capacitors of 0.7. However, large variances in the dissipation factor for all samples indicate that further research is required. Resistivity was not so high as desired, with the median of all measured samples at  $2 \times 10^8 \Omega\text{-cm}$ . For those samples with acceptable electrical properties, the resistivity was as high as  $3.5 \times 10^{12} \Omega\text{-cm}$ . Voltage-breakdown strength for the samples measured has a median range of 26.5 kV/mm, with a maximum obtained value of 393 kV/mm. The dielectric constant values also varied drastically. For those samples that produced optimum electrical properties, the values were near 2. The optimum film resulted in a dielectric constant of 2.34. The median value of all samples created

was 10.1. These values fall within the anticipated range.

To date, Sample Nos. 615, 618, and 645 represent the optimum electrical characteristics among the samples developed using the dual-ion-beam deposition process. For the single-ion-beam process, Sample Nos. 609-614 produced the best results. Sample No. 614 was unique, with a composite layer consisting of the initial and final layer deposited using the dual ion process, while the center layer utilized the single-ion-beam process.

RBS and ERS analysis on post annealed samples demonstrated that  $CN_x$  film remains compositionally stable up to a maximum of 600°C for samples using the dual ion beam process. These same samples were also shown to remain intact, with no evidence of spallation, peeling, or cracking up to 900°C, although changes in film composition did occur.  $CN_x$  films developed using the single-ion-beam deposition method remained thermally stable up to 400°C before evidence of compositional change. This is due to the higher concentrations of hydrogen that are easily liberated at elevated temperatures. Although these single-ion-beam-deposited films contain hydrogen at concentrations near that for DLC, they are thermally more stable, with DLC being stable only up to 250°C.

## 7.0 FURTHER RESEARCH

Collaborative work provided a method of acquiring some tribological data on single-ion-beam-deposited DLC and nitrided DLC. This limited amount of data showed promising results. Further testing in this area using current  $CN_x$  film-deposition conditions is anticipated to reveal exceptional properties.

Development of  $CN_x$  film for various applications is complex, as shown in this report and as reported by others. Further basic research on the development and overall growth of  $CN_x$  film is needed to gain an understanding of the underlying molecular and bonding structures associated with this film. Morphology, elemental bonding, and microstructure of  $CN_x$  film should be investigated for further enhancement of film quality and further reduction of the amount of  $sp^2$  bonding dispersed through the amorphous matrix. Substrate deposition temperature, i-beam parameters, gas mixtures, and gas types should be studied in relation to the  $sp^2$  and  $sp^3$  bonding of the film. Concurrently, these relationships must also be compared with the associated electrical, thermal, and tribological properties of the film.

Further improvements in the system layout and additional enhancements to the equipment are expected to improve growth rate and quality.

Capacitance testing should be performed to study the effects on  $CN_x$  films at elevated temperatures. Whether electrical properties will remain the same, change as a function of temperature, or permanently degrade has not been determined.

## 8.0 PUBLICATIONS AND PRESENTATIONS

The following is a list of the papers, journal articles, and oral and poster presentations accomplished or scheduled during this contractual period.

1. "Microstructure, Morphology and Electrical Properties of Carbon Nitride (CN<sub>x</sub>) Thin Films for Use as a High Temperature Dielectric," W.C. Lanter, B.A. Tolson, D.C. Ingram, and C.A. DeJoseph, SAE Power Systems Conf., Nov. 2006, Presentation.
2. "Development of Carbon Nitride (CN<sub>x</sub>) for use as a Flexible, Thermally-Conductive, High Temperature Dielectric," W.C. Lanter, B.A. Tolson, D.C. Ingram, and C.A. DeJoseph, Matl. Sci. Technol. Conf., Oct. 2006, Presentation.
3. "Single vs. Dual Ion Beam Growth of CN<sub>x</sub>," W.C. Lanter, B.A. Tolson, D.C. Ingram, and C.A. DeJoseph, Int. Conf. of Plasma Science (ICOPS) June 2006, Poster Presentation.
4. "Amorphous Carbon Nitride for High Temperature Capacitor Dielectric," W.C. Lanter, D.C. Ingram, and C.A. DeJoseph, Diam. Rel. Mat. 15(2-3), 2006, pp. 259-263.
5. "Trapping of hydrogen in carbon nitride films during or after high temperature heat treatment." D.C. Ingram, A. Kayani, W.C. Lanter, and C.A. DeJoseph, Fall MRS Meeting 2004, Presentation.
6. "Thermal Stability of Ion-Beam Deposited CN<sub>x</sub> Thin Films," W.C. Lanter, D.C. Ingram, A. Kayani, and C.A. DeJoseph, High Temperature Electronics Conference (HiTec), May 2004, Presentation.
7. "Thermal Stability of Thin Films of Ion Beam Deposited CN<sub>x</sub>," D.C. Ingram, A.N. Kayani, W.C. Lanter, and C.A. DeJoseph, Fall MRS Meeting 2003, Presentation.
8. "Growth of Carbon-Nitrogen Films with a Broad Beam rf Ion Source," D.C. Ingram, W.C. Lanter, C.A. DeJoseph, and A. Kayani, Materials Research Society Symposium Proceedings 693, 2001, p. 55.
9. "Large Area Surface Treatment by Ion Beam Technique," R.L.C. Wu, W.C. Lanter, J.D. Wrbanek, and C.A. DeJoseph, Prog. Organic Coating/Surface Coating Technol. 140(1), 2001, pp. 35-43.
10. "Synthesis and Dielectric Properties of Carbon Nitride Thin Films," W.C. Lanter, D.C. Ingram, C.A. DeJoseph, and R.L.C. Wu, Advanced Diamond Conf. and Frontiers of Carbon Technol. (ADC-FCT), Auburn University, 2001, Presentation.
11. "Processing Effects on Electrical Properties of Diamond-Like Carbon," R.L.C. Wu, W.C. Lanter, J. Wrbanek, P.B. Kosel, and C.A. DeJoseph, New Diamond Frontier Technol., Vol. 10, No. 6, 2000, pp. 383-396.
12. "A New Manufacturing Technology for Producing High Energy Density Diamond-Like Carbon Capacitors," R.L.C. Wu, J. Wrbanek, W.C. Lanter, P.B. Kosel, S. Fries-Carr, and J. Weimer, Proceeding 20th Capacitor and Resistor Technology Symposium (CARTS), 2000, pp. 111-116.
13. "Ion Beam Processing of Carbon Nitride Thin Films," R.L.C. Wu, W.C. Lanter, J. Wrbanek, P.B. Kosel, and C.A. DeJoseph, Materials Research Society Symposium Proceedings, Vol. 585, 2000.

**Table 11 Electrical Summary of CN<sub>x</sub> Capacitors**

Sample ID	No. Pads D <sub>r</sub> <1.0	Capacitance (F)	Dissipation Factor (D <sub>i</sub> )		Thickness (Å)	Resistivity (Ω-cm)			Dielectric Const. (ε <sub>r</sub> )		Dielectric Strength (E <sub>b</sub> ) (kV/mm)			Run Time (min)	Dep. Rate (Å/min)
		Median	Low	Median		Low	Median	High	Low	Median	Low	Median	High		
646_CrAlSi	0	1.24E-07	-0.021	889.623										838	
646_Si	0	2.69E-08	164.757	366.578	4860				78.8	214.7				838	5.80
645_CrAlSi	0	2.20E-09	238.651	1890.000	2605				2.7	13.4				562	4.64
645_SiCap	13	3.06E-09	0.306	0.431	1568	6.2E+06	2.3E+07	1.7E+08	7.0	7.7			24.23	562	2.79
645_Si	11	2.56E-09	0.092	0.146	4477	4.8E-04	2.6E+07	1.4E+12	12.3	18.4			22.56	562	7.97
645_AlSi	16	3.05E-09	0.171	0.190	1978	1.1E-03	5.1E+07	3.5E+12	9.2	9.7			134.48	562	3.52
644_AlSi	4	1.77E-08	0.043	1250.000	602				0.8	17.0				768	0.78
644_CrAlSi	0	3.73E-09	205.172	454.579	1236				1.9	7.8				768	1.61
644_Si	0	4.39E-09	112.422	169.490	2741				1.1	19.7				768	3.57
643_AlSi	1	3.63E-08	0.040	867.285	108				0.5	6.3				464	0.23
642_AlSi	15	2.63E-08	0.026	0.038	2083	3.7E+06	7.0E+06	1.7E+10	86.1	87.5			28.80	453	4.60
641_AlSi	13	2.94E-08	0.024	0.032	2470	2.9E+06	5.5E+06	2.8E+39	6.6	116.2			17.00	464	5.32
640_AlSi	0	6.62E-08	520.055	744.893	682				30.1	72.1				711	0.96
639_AlSi	14	2.51E-08	0.035	0.077	1384	5.2E+06	1.9E+07	2.3E+09	0.4	55.6				425	3.26
638_AlSi	2	8.70E-09	-0.011	1200.000	820				0.1	15.9				321	2.55
637_AlSi	0	9.90E+37	55.520	9.9E+37	4626				157.7	7.3E+47				733	6.31
637_CrAlSi	0	2.04E-09	336.589	1090.000	1207				0.6	4.1				733	1.65
637_Si	0	2.87E-08	197.539	680.396	3012				14.7	138.4				733	4.11
636_CrAlSi	0	3.29E-08	1160.000	1770.000	872				4.0	45.8				878	0.99
636_Si	0	9.56E-09	1.243	1.961	862	9.6E+06	1.1E+07	1.5E+07	3.4	13.2				878	0.98
636_AlSi	9	2.61E-08	0.484	0.813	1287	5.6E+06	8.3E+06	8.9E+06	12.4	53.8				878	1.47
635_AlSi	16	1.54E-08	0.077	0.092	4997	1.5E+06	1.2E+07	7.4E+09	108.1	123.4			11.01	980	5.10
635_CrAlSi	0	1.39E-08	150.006	477.988	4194				62.2	93.3				980	4.28
635_Si	0	1.38E-08	1.000	1.323	4602	1.8E+06	2.9E+06	9.4E+06	25.4	101.9				980	4.70
634_AlSi	16	2.37E-08	0.037	0.045	2015	3.6E+06	2.2E+07	3.9E+08	71.7	76.3			30.27	468	4.31
634_CrAlSi	0	5.92E-08	876.335	1160.000	924				1.8	87.4				468	1.97
634_Si	14	4.28E-08	0.321	0.711	1239	9.1E+06	1.2E+07	2.4E+08	53.0	84.8				468	2.65
633_AlGI	10	1.38E-08	0.107	0.155	2602	2.8E+06	2.7E+07	5.7E+08	1.6	74.5				555	4.69
633_CrAlSi	0	1.52E+08	6.609	333.302	1903	3.8E+06	3.8E+06	3.8E+06	1.1	46.1				555	3.43
633_Si	1	4.57E-09	0.870	1.440	2783	3.5E+06	4.9E+06	1.1E+07	5.8	20.4			11.50	555	5.01

**Table 11 Electrical Summary of CN<sub>x</sub> Capacitors**

Sample ID	No. Pads D <sub>r</sub> <1.0	Capacitance (F)	Dissipation Factor (D <sub>i</sub> )		Thickness (Å)	Resistivity (Ω-cm)			Dielectric Const. (ε <sub>r</sub> )		Dielectric Strength (E <sub>b</sub> ) (kV/mm)			Run Time (min)	Dep. Rate (Å/min)
			Low	Median		Low	Median	High	Low	Median	Low	Median	High		
632_AIGI	12	2.46E-08	0.055	0.094	2892	2.5E+06	2.8E+06	1.5E+07	8.9	113.6			13.14	750	3.86
632_CrAlSi	0	1.56E-09	149.640	969.720	2192				8.6	56.7				750	2.92
632_SiCap	15	4.95E-08	0.271	0.548	2777	5.4E+06	8.9E+06	9.1E+07	185.6	218.6				750	3.70
627A_AlSi	8	2.36E-08	0.129	333.020	808	8.8E+06	8.8E+06	8.8E+06	33.2	33.5				515	1.57
627_Si	15	1.74E-08	0.055	0.120	980	5.9E+07	1.4E+08	4.8E+09	19.7	27.2	10.20	22.45	30.61	515	1.90
626A_Si	14	1.49E-08	0.073	0.145	721	9.9E+06	2.9E+07	3.6E+07	8.8	17.1	41.61	81.14	99.86	608	1.19
626_AIGI	15	1.99E-08	0.092	0.134	3848	2.6E+06	1.0E+08	2.6E+08	121.4	124.6	2.60	2.60	3.90	608	6.33
625_AlSi	14	1.98E-08	0.100	0.154	2330	3.1E+06	6.5E+06	1.6E+07			4.29	4.29	8.58	670	3.48
625_Si	14	1.60E-08	0.125	0.413	457	1.7E+07	9.9E+07	1.5E+08	10.0	11.7	21.88	54.70	76.59	670	0.68
624_Si	16	3.53E-08	0.406	0.555	616	1.5E+07	1.6E+09	1.7E+07	46.7	55.0	16.23	16.23	16.23	370	1.66
623_Si	16	2.39E-08	0.188	0.296	757	1.1E+07	1.3E+07	1.5E+07	21.6	26.6	13.21	13.21	13.21	Unk	
622_Si	15	5.61E-08	0.179	0.222	1175	1.1E+07	1.2E+07	1.6E+08	97.6	101.2	8.51	8.51	8.51	270	4.35
620_1_Si	0	1.41E-08	11.683	22.494	938									926	1.01
620_2_Si	0	3.59E-08	18.773	40.647										926	
619_AlSi	7	4.25E-08	0.236	0.682	3470	2.1E+06	3.2E+06	3.4E+06	241.1	290.4	2.88	2.88	2.88	1310	2.65
619_Si1	14	1.66E-08	0.333	0.507	5113	2.7E+06	2.9E+06	3.9E+06	126.9	137.7	1.96	1.96	1.96	1310	3.90
619_Si2	12	1.87E-08	0.101	0.153	2280	4.3E+06	1.6E+07	4.6E+07	67.1	68.3	4.39	4.39	8.77	1310	1.74
618A_Si2	15	2.85E-09	0.087	0.093	509	7.3E+07	1.5E+11	5.3E+11	2.2	2.3	19.65	216.11	392.93	1275	0.40
618B_Si1	11	6.66E-09	0.065	0.074	1763	8.1E+06	3.2E+10	9.3E+10	16.8	18.8	28.36	56.72	232.56	1275	1.38
618_AlSi	13	8.18E+09	0.279	0.360	1621	6.1E+08	2.1E+09	2.8E+09	26.6	27.4	6.17	24.68	30.85	1275	1.27
617B_Si1	14	1.81E-08	0.187	0.246	4336	4.5E+06	5.5E+06	1.4E+07	124.0	126.0	3.46	3.46	3.46	Unk	
617_AlSi	10	2.19E-08	0.142	0.150	4185	3.2E+06	5.4E+06	8.1E+06	142.9	149.7	2.39	2.39	2.39	Unk	
617_Si	16	1.30E-08	0.133	0.156	3582	1.1E+00	1.8E+07	4.9E+07	65.3	73.7				Unk	
616_AlSi	8	2.19E-09	-0.033	1.135	2374									Unk	
616_Si	16	8.82E-13	0.031	0.112	1535									Unk	
615_AlSi	7	1.41E-08	0.042	225.179	794									750	1.06
615_Si	16	1.03E-08	0.085	0.100	649	2.0E+07	2.3E+10	1.2E+11	10.1	10.7	46.22	114.02	123.27	750	0.87
614_AlSi	15	2.73E-10	0.055	0.061	7504	1.7E+09	5.2E+09	6.9E+12	1.2	3.3	26.65	57.30	103.94	590	12.72
613_AlSi	5	2.62E-09	0.214	2450.000	2515	2.8E+07	6.5E+07	1.7E+08	6.8	7.1	15.90	19.88	55.67	150	16.77
613_Si	16	1.26E-09	0.109	0.114	2547	4.7E+06	2.6E+09	3.3E+09	5.1	5.3	31.41	35.34	43.19	150	16.98

**Table 11 Electrical Summary of CN<sub>x</sub> Capacitors**

Sample ID	No. Pads D <sub>r</sub> <1.0	Capacitance (F)	Dissipation Factor (D <sub>f</sub> )		Thickness (Å)	Resistivity (Ω-cm)			Dielectric Const. (ε <sub>r</sub> )		Dielectric Strength (E <sub>b</sub> ) (kV/mm)			Run Time (min)	Dep. Rate (Å/min)
			Low	Median		Low	Median	High	Low	Median	Low	Median	High		
612_AISi		6.35E-09	0.090	1580.000		6.4E+09	6.6E+09	6.7E+09	25.7	25.7	157.58	157.58	157.58	180	
612_Si		1.97E-09	0.070	0.080		6.9E+06	1.7E+10	1.1E+11	5.1	5.8	10.91	76.34	118.32	180	
611_AISi		7.57E-08	597.833	1260.000	1438									180	7.99
610_AIGI		9.74E-10	0.020	699.750		4.8E+00	1.1E+10	9.0E+10	3.8	4.2	11.21	16.68	67.26	300	
610_Si		1.04E-09	0.000	2.440		2.7E+06	9.2E+10	1.2E+11	6.7	7.0	11.83	18.93	21.30	300	
609_AIGI		1.71E-09	0.030	656.160		8.5E+07	4.7E+08	4.0E+09	5.1	5.3	10.25	48.67	81.97	160	
Low	0	8.82E-13	-0.033	0.032	108	4.8E-04	2.8E+06	3.4E+06	0.1	2.3	1.96	1.96	1.96	150	0.23
Median	10.5	1.63E-08	0.1375	0.6965	1978	4.9E+06	2.0E+07	2.1E+08	10.1	39.7	11.21	19.88	26.5	639	3.26
Max	16	9.9E+37	1160	9.9E+37	7504	6.4E+09	1.5E+11	2.8E+39	241.1	7.3E+47	157.58	216.11	392.93	1310	16.98

**Table 12. Optical-Imaging Summary**

Sample No.	Sample Type	Magnification	Field of View (mm <sup>2</sup> )	Comments	Pinhole Count	Contaminant Count	Pinholes/mm <sup>2</sup>	Contaminant/mm <sup>2</sup>
646	CrAlSi	10 x 10	1.4	few pinholes; couple black specks; some scratches	5	3	4	2
646	Si Cap	10 x 10	1.4	few pinholes; couple black specks; some scratches	6	2	4	1
646	Si	10 x 10	1.4	1 - 2 pinholes; couple black specks; some scratches	2	4	1	3
645	CrAlSi	10 x 10	1.4	several scratches; moderate surface roughness; moderate pinholes; minimum black spots	16	3	11	2
645	AlSi	10 x 10	1.4	moderate scratches; some rough surface patches; very minimum black spots; light moderate pinholes	12	2	9	1
645	Si Cap	10 x 10	1.4	moderate # & size of pinholes; moderate # black spots	12	11	9	8
645	Si	10 x 10	1.4	minimum pinholes; very few black spots	13	5	9	4
645	CrAlSi	10 x 10	1.4	couple of pinholes; couple of black spots	1	1	1	1
645	Si	10 x 10	1.4	couple of pinholes; couple of black spots (more than 645 CrAlSi)	7	13	5	9
644	AlSi	10 x 10	1.4	moderately rough surface; several very small pinholes; minimum black spots	87	2	62	1
644	CrAlSi	10 x 10	1.4	moderate pinholes & black spots	56	5	40	4
644	Si Cap	10 x 10	1.4	several pinholes (small & large); minimum black spots	75	1	54	1
644	Si	10 x 10	1.4	numerous pinholes; no visible black spots	115	0	82	0

**Table 12. Optical-Imaging Summary**

Sample No.	Sample Type	Magnification	Field of View (mm <sup>2</sup> )	Comments	Pinhole Count	Contaminant Count	Pinholes/mm <sup>2</sup>	Contaminant/mm <sup>2</sup>
644	CrAlSi	10 x 10	1.4	numerous pinholes; no visible black spots	71	0	51	0
643	AlSi	10 x 10	1.4	variety of small and large pinholes, many but spaced	97	0	69	0
642	AlSi	10 x 10	1.4	larger and very numerous pinholes; few black spots	250	1	179	1
641	AlSi	10 x 10	1.4	larger, more spaced out pinholes; some craters	44	2	31	1
640	AlSi	10 x 10	1.4	moderate amount of small pinholes; couple scratches	116	0	83	0
639	AlSi	10 x 10	1.4	many tiny pinholes; rare black spots; otherwise smooth surface	200	1	143	1
638	AlSi	10 x 10	1.4	many tiny pinholes; few scratches; no black spots	160	0	114	0
637	AlSi	10 x 10	1.4	medium # pinholes, relatively smaller, few craters	40	0	29	0
637	CrAlSi	10 x 10	1.4	minimum pinholes; very few black spots	15	3	11	2
637	CrAlSi	10 x 10	1.4	couple pinholes; moderate large black spots	6	16	4	11
637	Si	10 x 10	1.4	no visible pinholes; minimum black holes	~~	~~		
636	AlSi	10 x 10	1.4	more holes at edges; many small pinholes spaced-out; specked with larger holes	87	2	62	1
636	Si	10 x 10	1.4	minimum pinholes; moderate black spots	5	11	4	8
635	Si	10 x 10	1.4	couple pinholes; moderate black spots	4	16	3	11
635	CrAlSi	10 x 10	1.4	couple pinholes; moderate black spots	3	8	2	6

**Table 12. Optical-Imaging Summary**

Sample No.	Sample Type	Magnification	Field of View (mm <sup>2</sup> )	Comments	Pinhole Count	Contaminant Count	Pinholes/mm <sup>2</sup>	Contaminant/mm <sup>2</sup>
634	CrAlSi	10 x 10	1.4	very uniform	19	0	14	0
634	CrAlSi	10 x 10	1.4	very uniform	25	0	18	0
634	Si	10 x 10	1.4	fair # of pinholes and black spots	63	2	45	1
634	AlSi	10 x 10	1.4	few pinholes	44	1	31	1
634	SiCap	10 x 10	1.4	very few pinholes; very few black spots	4	3	3	2
634	CrAlSi	10 x 10	1.4	very few pinholes; very few black spots	16	2	11	1
633	Si Cap	10 x 10	1.4	minimum pinholes	9	2	6	1
633	AlGI	10 x 10	1.4	moderate pinholes; film appears rough	17	0	12	0
633	CrAlSi	10 x 10	1.4	minimum pinholes; moderate black spots	5	5	4	4
633	CrAlSi	10 x 10	1.4	very few pinholes; no visible black spots	6	0	4	0
633	Si	10 x 10	1.4	minimum pinholes; no visible black spots	10	0	7	0
632	CrAlSi	10 x 10	1.4	minimum pinholes; moderate black spots	6	4	4	3
632	Si Cap	10 x 10	1.4	moderate pinholes; minimum black spots	12	6	9	4
632	AlGI	10 x 10	1.4	moderately rough surface; moderate pinholes & black spots	9	4	6	3
632	CrAlSi	10 x 10	1.4	no visible pinholes; very minimum black holes	0	9	0	6
632	Si Cap	10 x 10	1.4	moderate pinholes; no visible black spots	~~	~~		

**Table 13. RBS and ERS Summary**

Sample ID	% C	% N	% H	% O	% Si/Al	% Ar	% Fe etc.	% Mo	% W etc.	Total	N:C	H:C	H:N	Comment
646-4	64.56	31.36	1.11	0.92	0.92		1.07		0.07	5.42E+18	0.486	0.017	0.035	first 10% has about twice the H content. 646-Si same
645-3	26.74	17.38	15.71	28.07	12.10		0.00			1.5E+18	0.65	0.588	0.904	2 layers, ~30% less H in top layer
645-3b	61.76	30.88	4.53		1.40		1.40		0.02	2.43E+18	0.5	0.073	0.147	645-1 similar thickness
644-1	50.72	37.91	6.12	2.65	2.21		0.34		0.04	7.89E+17	0.748	0.121	0.162	644-Si was 2.2 times thicker and had less (50%) H away from the surface
643-C-4	54.72	30.71	6.02	4.04	1.92		2.49		0.10	3.29E+17	0.561	0.11	0.196	quite thin, on Si maybe 105 thicker
642-C-1	56.39	18.33	16.63	8.32					0.34	7.09E+16	0.325	0.295	0.908	really thin and same on Si
641-C-8	53.28	15.99	21.05	7.33	1.33		0.76		0.27	7.51E+16	0.3	0.395	1.317	really thin and same on Si
640-C-3	67.28	20.19	5.79	3.26	1.55		1.82		0.12	2.97E+17	0.3	0.086	0.287	really thin again, film on Si 60% thinner
639-C-6	56.99	16.94	13.27	9.77	1.95		0.90		0.18	1.23E+17	0.297	0.233	0.784	really, really thin, 50% thicker on Si but still too thin for good measurements

**Table 13. RBS and ERS Summary**

Sample ID	% C	% N	% H	% O	% Si/Al	% Ar	% Fe etc.	% Mo	% W etc.	Total	N:C	H:C	H:N	Comment
638-C-1	64.57	22.92	8.59	2.65	0.21		0.97		0.10	3.1E+17	0.355	0.133	0.375	film too thin for useful analysis, same thickness and composition on Si, however, now can see that peak below W is not W but something else, mass-La
637-C-6	71.47	24.86	1.77	1.03	0.41		0.43		0.03	1.26E+18	0.348	0.025	0.071	on Si film about 50% thick and bulk H distinguishable from surface, it is about 50% of mean H on carbon
636-C-4	50.05	34.80	6.91	2.77	4.00		1.35	0.05	0.07	1.3E+18	0.695	0.138	0.198	no obvious layered structure, on Si about 1/3 thicker
635-C-6	42.02	23.11	16.39	14.29	4.20					2.38E+17	0.55	0.39	0.709	
635-C-6b	62.91	34.60	1.26		1.15		0.06		0.01	5.72E+18	0.55	0.02	0.036	
634-C-3	59.84	36.50	1.61	0.92	1.01		0.11		0.01	2.17E+18	0.61	0.027	0.044	has three layers with the top and bottom having about 2x the h in the bulk, which is what is calculated, the other elements did not vary significantly
633-C-5	46.15	27.69	12.82	10.00	3.33				0.01	3.9E+17	0.6	0.278	0.463	a layer on top with lots of H, film on silicon is about 2/3 as thick
633-C-5b	60.62	36.37	2.06	0.00	0.94				0.01	2.67E+18	0.6	0.034	0.057	
632-C-8	61.72	37.03	0.80		0.44				0.01	4.21E+18	0.6	0.013	0.022	a layer with about three times the h is present at the surface

**Table 13. RBS and ERS Summary**

Sample ID	% C	% N	% H	% O	% Si/Al	% Ar	% Fe etc.	% Mo	% W etc.	Total	N:C	H:C	H:N	Comment
631-C-1	52.47	12.80	28.73	6.00						7.62E+17	0.244	0.548	2.244	a thin film with lots of hydrogen, film on Si same.
630-C-9	55.82	13.84	29.02	1.32						4.48E+17	0.248	0.52	2.097	a thin layer, same on Si
629	56.34	14.08	28.17	1.13	0.28						0.250	0.50	2.001	
626-C-2	51.34	29.57	16.38	0.94	1.08		0.67		0.02	1.95E+17	0.576	0.319	0.554	This two layer structure is quite typical of these films.
626-C-2b	60.35	34.76	1.71	1.11	1.27		0.78		0.02	1.66E+18	0.576	0.028	0.049	
625-C-4	60.18	34.66	1.99	1.11	1.26		0.78		0.02	1.66E+18	0.576	0.033	0.057	surface peak of hydrogen very obvious like the above, mean level of H is below surface by about 2/3 average for the film, on Si film is 0.45 as thick.
624-C-9	59.43	34.92	2.64	1.49	1.11		0.38		0.03	1.35E+18	0.588	0.045	0.076	almost identical to 623-C-1 but a little thinner, same H surface peak, on Si 0.35 as thick
623-C-1	62.31	33.75	2.06	0.88	0.68		0.29		0.03	1.93E+18	0.542	0.033	0.061	almost identical to 622-C-1, same H surface peak but about X4 less H in bulk, on Si the same but slightly thinner (<10%)
622-C-1	61.08	33.08	4.00	0.87	0.66		0.31		0.01	1.96E+18	0.542	0.065	0.121	film on Si slightly (<10%) thinner than on carbon
620-C-1	83.59	3.76	2.97	1.84	0.37	2.09	5.35	0.02	0.02	1.2E+18	0.045	0.036	0.789	Ar and Mo clearly visible in this sample therefore not included in Fe or W as for thicker samples

**Table 13. RBS and ERS Summary**

Sample ID	% C	% N	% H	% O	% Si/Al	% Ar	% Fe etc.	% Mo	% W etc.	Total	N:C	H:C	H:N	Comment
619-C-1	63.14	31.57	2.26	1.13	0.95		0.95		0.01	4.43E+18	0.5	0.036	0.071	same composition as C-4 and C-6, but C-4 and C-6 both 15% thicker
618c	50.72	35.51	8.62	1.01	3.55		0.56				0.70	0.17	0.24	
618b	34.83	24.38	17.06	20.90	2.44		0.38				0.70	0.49	0.70	
618a	48.41	33.89	7.26	4.84	4.84		0.73				0.70	0.15	0.21	
617	59.88	35.93	1.80	1.20	0.60		0.60			5.34E+18	0.60	0.03	0.05	
616b	41.58	22.87	16.63	12.47	6.24		0.21			2.41E+17	0.55	0.40	0.73	
616	59.70	32.84	4.78	1.19	1.19		0.30			5.03E+18	0.55	0.08	0.15	
615	59.17	35.50	2.96	1.18	0.59		0.59			2.20E+18	0.60	0.05	0.08	

**Table 14. Electrical Summary for Single-Ion-Beam CN<sub>x</sub> Deposition**

Sample No.	No. in Ave.	Capacitance (F)	Dissipation	Parallel(Rp) (Ω)	Series(Rs) (Ω)	ESR (Ω)
505	all bad	4.6E-09	3370	21	21	41
507	all bad	1.45E-08	3110	4	4	8
508	2	2.11E-08	0.44	17550	2770	5545
510	6	1.23E-11	0.96	13350000	6460000	12916667
511	2	3.03E-08	1.30	4065	2550	5095
513	13	2.97E-09	0.94	59662	27215	54462
515	15	7.16E-09	0.74	31053	10915	21807
516	5	6.87E-10	1.14	6514600	3226820	6441640
517	3	1.49E-11	0.54	24800000	4650000	9306667
519	1	7.65E-09	0.286	72400	5420	10900
520	11	6.05E-09	0.27	102773	6552	13092
542						
543						
544	all bad	2.12E-08	7.39	1070	1040	2080
545						
546	all bad	9.65E-09	3140	20	20	39
547	all bad	3.82E-08	1410	5	5	10
548						
549	all bad	1.13E-08	4360	115	112	224
550	all bad	4.6E-08	353	3830000	2220000	5360000
551	all bad	2.91E-08	4300	13	13	27
552	all bad	6.71E-08	597	46	46	91
553	all bad	1.97E-08	2870	12	12	24
554	all bad	4.76E-08	16.1	288	282	564
555	5	1.66E-08	0.31	36000	2710	5376
556	3	4.58E-08	0.43	9417	1515	3030
557	12	2.68E-08	0.94	9247	4548	9087
558	all bad	3.95E-09	3130	285	285	569
559	8	5.55E-08	0.41	13913	2646	5291
560	12	3.50E-09	1.05	46592	23650	47317
561	9	3.89E-09	1.23	48622	24133	48267
562	14	6.79E-09	0.99	33197	14005	27997
563						
564						
565	9	3.35E-09	0.89	89180	35758	71460
567						
568	5	2.83E-09	1.09	119520	38260	76500
569						
570						
571	14	8.09E-09	1.39	20155	13340	26952

**Table 14. Electrical Summary for Single-Ion-Beam CN<sub>x</sub> Deposition**

<b>Sample No.</b>	<b>No. in Ave.</b>	<b>Capacitance (F)</b>	<b>Dissipation</b>	<b>Parallel(Rp) (Ω)</b>	<b>Series(Rs) (Ω)</b>	<b>ESR (Ω)</b>
572	16	6.82E-10	0.68	577000	104000	209000
609 AlGl	6	1.71E-09	0.04	2.41E+06		6.70E+03
610 AlGl	13	9.74E-10	0.03	6.45E+06		8.26E+03
610 Si	8	1.04E-09	0.02	9.07E+06		5.40E+03
611 AlSi	0	7.57E-08	1.26E+03	1.60		3.19
611 Si	15	2.09E-09	0.03	2.65E+06		4.27E+03
612 AlSi	1	6.35E-09	1.58E+03	8.81		17.68
612 Si	16	1.97E-09	0.08	1.09E+06		1.23E+04
613 AlSi	3	2.62E-09	2.45E+03	16.95		33.85
613 Si	8	1.26E-09	0.11	1.08E+06		2.85E+04
614 AlSi	16	2.73E-10	0.06	9.51E+06		7.11E+04

## TASK 2. ADVANCED PLASMA DIAGNOSTICS

### 1.0 GENERAL OVERVIEW

The primary objective of this task was to perform research on advanced RF plasma diagnostics, with concentration on the development of reliable and accurate characterization methods for both cw and modulated plasmas that are generated by different plasma sources.

Investigation of a high-density plasma source such as inductively coupled plasma (ICP) was of particular interest because it is regarded as one of the powerful tools that is replacing conventional plasma reactors in semiconductor industries. The major advantage of using ICP is that much higher plasma densities than those of conventional reactors are obtainable under very low gas pressures. For example, ICP sources are popular for etching submicrometer features, soft clean for physical-vapor-deposition cluster tools, and plasma-enhanced chemical-vapor deposition. The basic requirements for submicrometer etching include high plasma densities ( $> 10^{11} \text{ cm}^{-3}$ ), a large and highly directional ion flux with low and controllable ion energies, low-pressure operation ( $< 10 \text{ mTorr}$ ), capability to control the ion energy and plasma density independent of each other, and ease of scalability to larger wafer diameters.

Time-modulated (pulsed) excitation of low-pressure radio-frequency (rf) discharges has recently been used to obtain greater control over plasma behavior by manipulation of the pulse period and duty cycle. For example, much higher peak plasma densities can be obtained by selecting an appropriate modulation period than by operating with continuous power while the average input power is kept constant. The plasma density is linearly proportional to the rf power applied, but the thermal runout of the rf window (alumina in the present system) limits the maximum rf power that can be applied for a given system. With pulsed-mode operation, it is possible to avoid overheating of the rf window, and this allows much higher peak rf power to be used on the same system. Based on a global model of a cylindrical plasma discharge,<sup>1</sup> it has been shown that for argon, plasma density more than twice the density of the cw plasma, driven by the same average power, can be obtained by power modulation with square wave at a duty ratio of 25%.<sup>2</sup> Even higher plasma densities can be obtained for shorter duty ratios. Other benefits of using pulsed plasma include inhibiting the formation of charged dust particles that can cause device failure,<sup>3</sup> reducing unwanted side-wall etching/sputtering, limiting damage due to the impact of energetic ions and charge buildup,<sup>4</sup> improving etch selectivity,<sup>5</sup> decreasing radical densities,<sup>5</sup> and

<sup>1</sup> C. Lee, D. B. Graves, M. A. Lieberman, and D. W. Hess, *J. Electrochem. Soc.* **141**, 1546 (1994).

<sup>2</sup> S. Ashida, C. Lee, and M. A. Lieberman, *J. Vac. Sci. Technol.* **A13**(5), 2498 (1995).

<sup>3</sup> Th. Trottenberg, A. Melzer, and A. Piel, *Plasma Sources Sci. Technol.* **A64**, 450 (1995).

<sup>4</sup> S. Samukawa and T. Mieno, *Plasma Sources Sci. Technol.* **5**, 132 (1996).

<sup>5</sup> H. Sugai and K. Nakamura, *J. Vac. Sci. Technol.* **A13**(3), 887 (1995).

avoiding overheating of the substrate. The benefit of reduced side-wall sputtering is very important to an ICP system because if the rf coupling efficiency is to be improved, the rf window in an ICP system must be cleaned periodically to remove the surface coatings that result from the side-wall sputtering. Thus, pulsed-mode operation will ease the demand on the rf window maintenance. Additionally, pulsing has been found to reduce film stresses when depositing thin films<sup>6</sup> as well. Operating under pulsed mode, it becomes possible to measure the time evolution of plasma parameters; thus, insight regarding reaction paths in processing plasmas can be obtained. Pulsed plasmas have also been used to study basic phenomena such as plasma formation during breakdown, many aspects of which are still poorly understood in rf systems.<sup>7</sup>

The Air Force Research Laboratory is interested in generating plasma with a relatively high fractional ionization rate under very low pressures ( $< 1$  mTorr),<sup>8</sup> which makes ICP an ideal candidate as a possible source. Combined with the time-modulated (pulsed) excitation technique, ICP allows higher peak plasma density to be obtained than that under cw operation for the same average rf power and permits the background plasma to be synchronized with highly bunched electron beams in a high-power microwave tube such that the background plasma is present only when the electron beam is present in the microwave tube. This will, for example, reduce charge buildup, the production of neutral radicals due to overheating of the electrons, and system contamination resulting from unnecessary etching/sputtering. As the result, the lifetime of some of the crucial components such as the vacuum windows and even the cathode itself in an electron gun can be increased.

## **2.0 MEASUREMENTS IN ARGON PULSED ICP**

### **2.1 Pulsed ICP Plasma Generation and Characterization**

Modulated rf power at 13.56 MHz was applied to a planar coil to generate pulsed, low-pressure, argon ICPs. The modulation was realized by applying a rectangular window function in time to the output of an rf generator, with modulation frequencies between 100 Hz and 30 kHz and duty cycles between 10% and 90%. Current and voltage measurements at the coil were used to measure the peak power. A scanning Langmuir probe and a heterodyne microwave interferometer were used to measure plasma density during the pulse. In addition to these diagnostics, a miniature fiber-optic spectrometer was used for spectral characterization of the light output from the plasma, and a photomultiplier tube with narrow band filters was used to monitor the time dependence of the plasma emission. As expected, much higher peak plasma densities could be produced without damaging the rf window. Also, a reduced surface-charging effect was observed by performing Langmuir probe measurements on the plasma body. Because

---

<sup>6</sup> C. Charles, R. W. Boswell, and H. Kuwahara, *J. Appl. Phys.* **67**, 40 (1995).

<sup>7</sup> R. W. Boswell and D. Vender, *Plasma Sources Sci. Technol.* **4**, 534 (1995).

<sup>8</sup> L. D. Moreland, E. Schamiloglu, R. W. Lemke, S. D. Korovin, V. V. Rostov, A. M. Roitman, K. J. Hendricks, and T. A. Spencer, IEEE Trans. Plasma Sci. **22**(5), 554 (1994).

of the non-linearity of the plasma impedance, excessive rf power reflections and harmonic components of the fundamental rf frequency (13.56 MHz) exist between the ICP antenna and the rf generator that complicate rf power measurements.

The results of this study were documented by Wei Guo (ISSI) and Charles DeJoseph, Jr. (AFRL) in a paper that was presented at the 27<sup>th</sup> IEEE International Conference on Plasma Science, 2000.

## **2.2 Time-Resolved Current and Voltage Measurements on Pulsed RF ICP**

Time-resolved current and voltage measurements were made on a pulsed rf ICP at 13.56 MHz in argon. Measurements were made on the rf coil using a high-voltage probe, a Rogowski current probe, and a high-performance digital oscilloscope. Relative phase information was also obtained to permit time-resolved rf power measurements to be made. Because of the inductive nature of the load, measurement of the phase had to be better than 0.6 mrad at 13.56 MHz to ensure that the power measurements would be accurate to 10%. This accuracy in phase measurement was achieved by careful positioning of the probes and by establishing accurate phase-calibration procedures. The power was calculated by three methods: discrete Fourier transform, integral of the current-voltage product over N periods, and least-squares fits of a sine wave to the measured data. Time-resolved measurements of the system complex impedance, power loss in the ICP planar coil, and the actual amount of rf power delivered to the plasma were made. These measurements yielded details during plasma breakdown and showed the transition from capacitive to inductive discharge. The results were compared with both time-resolved plasma-emission and time-resolved Langmuir-probe measurements.

The results of this effort were documented in a paper by Wei Guo (ISSI) and Charles DeJoseph, Jr. (AFRL), which was published in Plasma Sources Science and Technology (Vol. 10, pp. 43-51, 2001). A reprint of this paper is included on subsequent pages.

# Time-resolved current and voltage measurements on a pulsed rf inductively coupled plasma†

Wei Guo<sup>1</sup> and Charles A DeJoseph Jr<sup>2</sup>

<sup>1</sup> Innovative Scientific Solutions Inc, 2766 Indian Ripple Road, Dayton, OH 45440, USA

<sup>2</sup> Air Force Research Laboratory, Wright-Patterson AFB, OH 45433-7919, USA

Received 5 September 2000, in final form 9 November 2000

## Abstract

Time resolved current and voltage measurements have been made on a pulsed radio frequency (rf) inductively coupled plasma (ICP) at 13.56 MHz in argon. Measurements were made on the rf coil using a high-voltage probe, a Rogowski current probe, and a high-performance digital oscilloscope. Relative phase information was also obtained so that time resolved rf power measurements could be made. Due to the inductive nature of the load, measurement of the phase had to be better than 0.6 mrad at 13.56 MHz in order that the power measurements were accurate to 10%. This accuracy in phase measurement was achieved by careful positioning of the probes and by establishing accurate phase calibration procedures. The power was calculated by three methods: discrete Fourier transform, integral of the current voltage product over  $N$  periods, and least-squares fits of a sine wave to the measured data. Time-resolved measurements of the system complex impedance, power loss in the ICP planar coil, and the actual amount of rf power delivered to the plasma were made. These measurements give details during plasma breakdown and show the transition from capacitive to inductive discharge. The results are compared with both time-resolved plasma emission and time-resolved Langmuir probe measurements.

## 1. Introduction

The inductively coupled plasma (ICP) technique was first patented by Coultas and Keller of the IBM Corporation [1] and by Ogle of the Lam Research Corporation [2] in 1990. Since then, a number of experiments have been conducted to characterize this type of plasma source when operated under continuous wave (cw) conditions. For example, in the case of an ICP source with a planar coil operated at 13.56 MHz, Hopwood *et al* examined electromagnetic fields [3], the uniformity of the ion density [4], and the ion energy distribution functions [5]. Mahoney *et al* [6] used rf-filtered Langmuir probes to measure the electron density and the energy distributions in argon plasmas. Based on the spatial probe data, they further estimated the local plasma conductivity and ionization rate. Wainman *et al* [7] characterized such argon plasmas generated with different aspect ratios (the ratio of the chamber radius  $r$  to height  $l$ ) at various input powers and

pressures. Miller *et al* [8] investigated ICP plasmas formed in a modified GEC rf reference cell with a voltage probe, Langmuir probe, and an 80 GHz microwave interferometer. In recent years, pulsed ICP plasma research has gained momentum since there are a number of potential benefits [9–15] from this excitation technique. So far, research on pulsed ICPs has concentrated mainly on the temporal characteristics of the plasma density and electron temperature. Overall, while research on ICPs has been extensive and fruitful, there is still a pressing need for a reliable method to accurately gauge the power to the plasma, since it is a very important parameter in determining the degree of plasma reproducibility for a given system and in comparing experimental results in parallel from system to system.

Conventionally, total rf power applied is usually measured before the matching network with either an in-line or an on-panel power meter. In the case of the cw ICPs, the power readings from those meters are relatively accurate and widely accepted as the power level used in generating the plasmas, assuming that the power losses in the matching network and the rf coil coupling structures are small and that most of the

† This paper is declared a work of the US Government and is not subject to copyright protection in the United States.

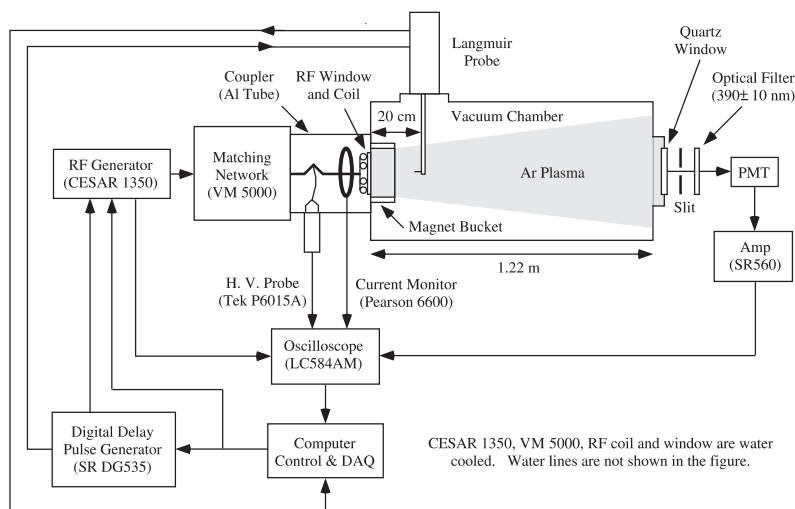


**Figure 1.** Schematic diagram of the experimental set-up.

rf power is absorbed by the plasma. In the case of pulsed ICPs, rf power measurements are complicated by the time response of the system, including the matching network and the rf coil supporting structure. The power level set at the rf generator front panel usually does not represent the actual power delivered to the load. Furthermore, the readings from either the on-panel or in-line power meters do not reveal any details of the plasma loading during the pulse. It should be pointed out that Sobolewski [16] has investigated the electrical characteristics of cw rf capacitively coupled argon plasmas in a GEC reference cell. In his experiment, a voltage and a current probe were positioned near the powered electrode after the matching network, with a variable shunt between the electrode and the ground. After characterizing the cell's stray capacitances, he was able to determine the impedance and power of the discharge from the current and voltage waveforms from the probes. With the same technique, Sobolewski has measured the ion current at a semiconductor wafer that is undergoing ICP plasma processing with variable wafer rf bias frequencies between 0.1 and 10 MHz [17].

This paper describes a time-resolved technique that can be applied in general to characterize pulsed rf ICP plasmas. The method is a straightforward application of current and voltage measurements similar to Sobolewski's [16], with special consideration for the inductive nature of the load. With careful hardware design and phase calibration, the total rf power, complex impedance of the system, the amount of power consumed by the rf coil itself, and the net rf power used in generating the pulsed plasma can be measured during a plasma modulation period with accuracy of better than 10%.

## 2. Experiment

A schematic of the experiment is shown in figure 1. The ICP system is a modified commercial ion-beam system built by Nordiko. Modifications include a new rf power supply and matching network, a new coil, and a new coupling section which mates the matching network to the coil and incorporates both current and voltage probes. In addition,

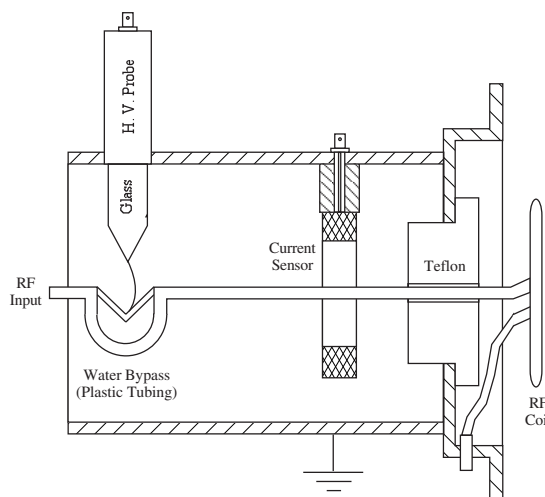


**Figure 2.** Schematic diagram of the rf coupling section between the matching network and the coil.

the system is operated without extraction grids hence the plasma diffuses freely from the source. A Dressler rf generator (CESAR 1350) with matching network (VM 5000) was used to supply power (0–5 kW variable) to a four-turn planar inductor coil at a fixed rf frequency of 13.56 MHz. Power could be 100% modulated using either an internal square-wave modulation or driven by an external pulse. The rf coil is coupled both mechanically and electrically to the matching network as shown in figures 1 and 2. This coupling section consists of a 6 mm diameter brass tubing with a spring and water bypass section at one end, which serves as the central support shaft for the rf coil, surrounded by a large outer aluminium cylinder of 16.2 cm diameter which serves as the rf shielding and mechanical support between the matching network housing and the vacuum chamber. The 'V'-shaped spring section welded onto the shaft near the matching network housing is made with 13 mm wide brass strips and supplies spring loading of the planar rf coil to ensure better surface contact, and hence cooling, between the coil and the alumina rf window. A section

of 6 mm diameter plastic tubing is connected to the brass tubing with compression-type fittings and serves as a water bypass around the spring section. Thus, current flows on the surface of the shaft through the spring section to the rf coil while water flows down the centre of the shaft and the coil to cool both the rf window and the coil. A Rogowski coil (Pearson model 6600 current monitor) is placed around the central shaft inside the coupling section near the coil to measure the total rf current. The current monitor is rigidly mounted to the inner wall of the aluminium cylinder of the coupling section. To minimize rf pickup, the aluminium cylinder is machined so the output connector on the side of the current monitor is directly passed through a hole on the wall of the coupling section. The hole is machined so that the outer shield of the mating connector makes an rf seal to the unit. In this way no part of the coaxial cable from the current probe lies inside the coupling section. Near the current monitor, a high-voltage probe (Tektronix model P6015A) is inserted through a tightly matched hole in the wall of the coupling section and is in contact with the central shaft for voltage measurements. A short 'U'-shaped section of 6 mm brass strip is used as the tip of the high-voltage probe and contacts the central shaft at the valley of the 'V'-shaped spring section. Once inserted and tightened down with an external clamp, the spring force from the brass strip ensures a reliable electrical contact between the high-voltage probe and the central shaft. The position of the high-voltage probe is such that the bottom edge of the grounded outer shield of the probe is flush with the inner wall of the aluminium cylinder so that only the glass section of the probe extends into the housing. An rf seal between the probe shield and the coupling section is made by holding tight tolerances between the hole diameter and the outside diameter of the probe. Instrumental control and data acquisition is by a 200 MHz Windows-based PC. Signals from the voltage and current probes are recorded on two channels of a four-channel digital oscilloscope (LeCroy model LC584AM). During pulsed rf data acquisition, the oscilloscope is triggered by two signals in 'AND' mode when the amplitudes of both signals are 'high'. One of the trigger signals is supplied by the 13.56 MHz on-board oscillator in the rf generator, which remains at constant amplitude during pulsed-rf operation. The second trigger signal is derived from the zero-delay channel of a digital delay and pulse generator (SRS model DG535). The DG535 is triggered by a computer board (Omega DaqBoard 200A) which supplies a rectangular pulse train that is also used to modulate the rf power. With this trigger arrangement, repetitive rf pulses are in-phase at the 13.56 MHz frequency thus allowing signal averaging of both current and voltage waveforms. A third channel of the oscilloscope records the signal from a photomultiplier tube (PMT) with a narrow-band filter ( $390 \pm 10$  nm) mounted at the far end of the vacuum chamber and facing the ICP source through a quartz window. The PMT is connected to a 1 k $\Omega$  load resistor and a low-noise preamplifier (SRS model SR560) is used to amplify the voltage across the resistor. A Langmuir probe (Scientific Systems' Smart Probe) with boxcar averaging capability is triggered by a delayed pulse from the DG535 so that by sweeping the time delay, time-dependent probe data can be acquired. The Langmuir probe is installed on top of the vacuum chamber near the plasma source with a tungsten wire tip, 7.8 mm in length and 0.38 mm

in diameter, parallel to the direction of the plasma flow. The distance between the probe tip and the core of the plasma source along the axis of the cylindrical vacuum chamber is approximately 10 cm. Finally, a low-resolution miniature fibre optic spectrometer (Ocean Optics model S2000-UV-VIS) is used to measure time-averaged emission spectra from the plasmas. The cylindrical stainless-steel vacuum chamber, 122 cm long and 61 cm in diameter, is customer designed and manufactured by Huntington Mechanical Laboratories, Inc. An oil-free dry scroll pump (Varian model 600DS) and a turbo pump (Varian model V1000HT) are used to pump the chamber down to a base pressure of  $2 \times 10^{-8}$  Torr. A high-accuracy capacitance manometer (MKS type 390HA, 1 Torr full scale) is used to monitor the system pressure. In operation, a throttle valve (MeiVac model Vari-Q) with controller (MKS type 153E) and pressure control system (MKS type 146) is used to maintain the chamber pressure around a preset value based on feedback from the capacitance manometer. The pressure in the chamber is maintained at 5 mTorr during an experiment.

### 3. Theory

Based on ac circuit theory, the instantaneous power in a circuit is given by the product of the time-dependent current and voltage. The average power over a period  $T$  is then given by

$$P = \frac{1}{T} \int_0^T V(t)I(t) dt. \quad (1)$$

For a sinusoidal current and voltage, equation (1) can be written as

$$P = \frac{V_P I_P}{2} \cos(\phi) \quad (2)$$

where  $V_P$  and  $I_P$  are the peak voltage and current and  $\phi$  is the relative phase between the two. Three methods were used to calculate average power in this experiment. Equation (1) was numerically integrated directly, while both discrete Fourier transform (DFT) and least-squares fitting were used to determine  $V_P$ ,  $I_P$ , and  $\phi$  in equation (2). For all three methods, the frequency was fixed at 13.56 MHz. While this approach is, in principle, straightforward it is made difficult by the inductive nature of the load. This leads to stringent requirements on the accuracy of the relative phase measurement between the current and voltage waveforms. The phase shift in equation (2) for an inductor can be written as

$$\phi = \tan^{-1} \left( \frac{\omega L}{R} \right) \quad (3)$$

where  $L$  and  $R$  are the inductance and resistance of the coil and  $\omega = 2\pi f$  is the rf angular frequency. For coils typically used in ICP systems, equation (3) is such that the current and voltage are close to  $90^\circ$  out of phase so let the phase  $\phi$  be written as

$$\phi = \frac{\pi}{2} - \delta \quad (4)$$

where  $\delta$  is generally much less than one. In our experiment, the values of  $R$  and  $L$  for the coil (with leads) were determined to be 0.42  $\Omega$  and 0.86  $\mu\text{H}$ . Thus, from equations (3) and (4) and for  $f = 13.56$  MHz, one obtains the value of  $\delta = 5.7 \times 10^{-3}$  rad.

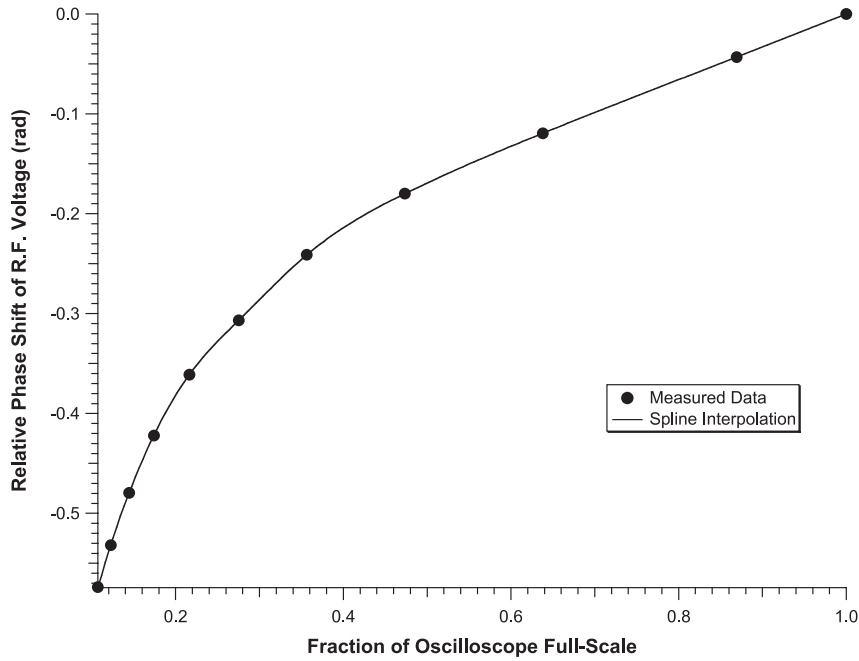


**Figure 3.** The measured voltage phase shift against the amplitude normalized to the full-scale amplitude. The sign of the phase is defined as  $f(t - \varphi)$ .

Substituting equation (4) into equation (2) and assuming  $\delta \ll 1$  gives

$$P = \frac{V_P I_P}{2} \sin(\delta) \approx \frac{V_P I_P}{2} \delta. \quad (5)$$

Differentiating equation (5) one finds that the uncertainty in the power measurement due to uncertainties in the relative phase measurement is given by

$$\frac{\Delta P}{P} \approx \frac{\Delta \delta}{\delta}. \quad (6)$$

Thus equation (6) dictates the requirements on the accuracy of phase measurement for a given uncertainty in rf power measurement. For this experiment with the  $\delta$  given above, one finds, from equation (6) for  $\Delta P/P = 10\%$ ,  $\Delta \delta \approx 0.6$  mrad. At a frequency of 13.56 MHz this translates into a timing accuracy of approximately 7 ps. Thus the relative timing accuracy between the measured voltage and current must be on the order of 7 ps to achieve an accuracy of 10% in the power measurements. This places stringent requirements on the probe mounting, cabling, and the oscilloscope along with accurate calibration of the relative phase measurement between the current and the voltage.

#### 4. Calibration

For accurate power measurements, both the amplitude response and phase delay of the various probes and cables had to be calibrated. The current and voltage amplitudes measured by the probes were calibrated based on procedures and data supplied by the manufacturers. Due to phase delays in the probes, cable length variations, and even variations in the propagation delays among the cables, the relative phase measured by the probes had to be calibrated *in situ*. This was done using cw rf power levels under the condition of

‘no plasma’ (no gas flow in the vacuum chamber). Based on the assumption that all the applied power goes into the coil, readings from an in-line power meter (Bird model 4391A) installed between the matching network and the generator were used in the calibration. Initially, we assumed the measured phase shift between the current and voltage signals differed from the true phase shift by a constant. Because the scope bandwidth (1 GHz) greatly exceeds the rf frequency (13.56 MHz) we felt that the signals should only be skewed in time as a result of cable delays, etc. What was found was that the phase calibration actually consisted of two parts: (1) a constant correction due to delays by the cables, probes, and residual stray capacitance in the rf circuit and (2) a ‘variable’ correction which depended on the scope gain and the amplitude of the waveforms. This variable correction shows up in two ways. There is a relatively large shift in phase of both the recorded current and voltage waveforms as a function of the amplitude when measured with respect to the trigger signal. As discussed above, the trigger is derived from the power supply local oscillator. This shift is most likely due to slew rate effects in the rf power supply. In addition, there is a much smaller relative phase shift between the current and voltage waveforms that is also amplitude dependent. This smaller phase shift appears to be related to slew rate effects in the probe/scope combination. The variable correction meant that for each gain setting used in the measurements, the phase had to be calibrated as a function of the amplitude of the signal. In phase calibration runs, 0.5  $\mu$ s segments of current and voltage sinusoidal waveforms were recorded with the two scope channels at fixed gain under various discrete power levels up to the maximum determined by the gain setting.

The signals were averaged to improve signal-to-noise ratio and the scope was operated in interleave sampling mode to increase the sampling frequency to 25 GHz. The measured phase shift (relative to the trigger) of the voltage waveform

as a function of amplitude for a fixed scope gain is shown in figure 3 under ‘no plasma’ conditions. Since the phase shift is dependent on the scope gain, identical *absolute* amplitudes would exhibit different phase shifts if recorded at different gain settings. Both the scope gain and the absolute waveform amplitude must be known to calculate the phase correction. Figure 3 also shows a cubic spline interpolation curve that was used to derive the variable phase correction for values between the calibration points. A similar calibration was performed on the current waveform. Since the gains were fixed, we were initially concerned with waveform fidelity at the lowest settings due to insufficient ‘active bits’ in the scope. As a result of signal averaging, errors due to poor waveform fidelity were much less than those due to residual phase errors. In summary, for the phase calibration a series of ‘no plasma’ runs were taken at fixed cw power levels. Then phase against amplitude (at a fixed gain) calibration curves were constructed for both the current and voltage waveforms. Finally, a constant phase correction was added to the current waveform to match the calculated power with the measured power from the Bird 4391A. Using this approach, the calculated powers were within  $\pm 5\%$  of the measured powers under the ‘no plasma’ condition. The phase calibration curves along with the constant offset were then used to correct the recorded waveforms under pulsed plasma conditions.

## 5. Power measurement

After calibrating the phase under cw conditions, data were recorded under pulsed rf operation. For pulsed power measurements, traces of the current and voltage waveforms were recorded simultaneously in 200  $\mu\text{s}$  long segments at a 2 GHz sampling rate (400 000 points each). For rf pulses longer than 200  $\mu\text{s}$  a series of these waveforms were recorded with appropriate trigger delays. For time-resolved measurements, these long waveforms were broken up into 0.5  $\mu\text{s}$  segments, each segment phase corrected and power calculated by the three previously mentioned methods: (1) DFT with Hanning window; (2) integral of  $I \times V$  over  $N$  periods; (3) LSF to a sinusoidal function. The three methods were used to provide a consistency check on the calculations. Since it was not clear how any one method might be affected by noise, digitizing rate, or behaviour during a transient, the use of three methods allowed a quick ‘sanity check’ on the measurements. While the three methods usually yielded different results, they agreed to within the  $\pm 5\%$  confidence band set by the phase uncertainty. Each method had to be carefully applied to yield consistent results. The DFT method *required* the Hanning window for consistent results. In addition, the error in the DFT calculation increased when one tried to push the time resolution by shortening the length of the waveform segments. The segment length of 0.5  $\mu\text{s}$  was the minimum for the DFT method to achieve the desired confidence limits. The integral of  $I \times V$  over  $N$  periods method required interpolation of the current and voltage waveforms, since the calibration phase shift was not necessarily an integral multiple of the sampling frequency. Linear interpolation was sufficient at the 25 GHz sampling rate used during the calibration runs, but proved inaccurate at the 2 GHz sampling rate used for the time-resolved data. At the lower sampling rate spline

interpolation was used. In the presence of significant noise, a different interpolation method might be necessary. The LSF method worked well, but only if the frequency was fixed in the calculation. If both the frequency and phase were adjusted during the fit, inconsistencies larger than  $\pm 5\%$  occurred. With fixed frequency, the LSF worked very well, even with segments as short as 0.25  $\mu\text{s}$ . In addition to the above three methods, which were applied to all data over all segments, as an option the DFT method could be extended to cover a range of frequencies to look for harmonics. This was an involved calculation and was only applied at selected regions of a current and voltage waveform. We routinely examined the data for harmonic content during regions where the current and voltage were changing rapidly. The harmonic content in these regions never exceeded 1% of the power and in most cases was less than 0.3%. Since these numbers were far below our  $\pm 5\%$  confidence limit on the data, we can only state that the harmonic content was too small to be observed.

## 6. Results

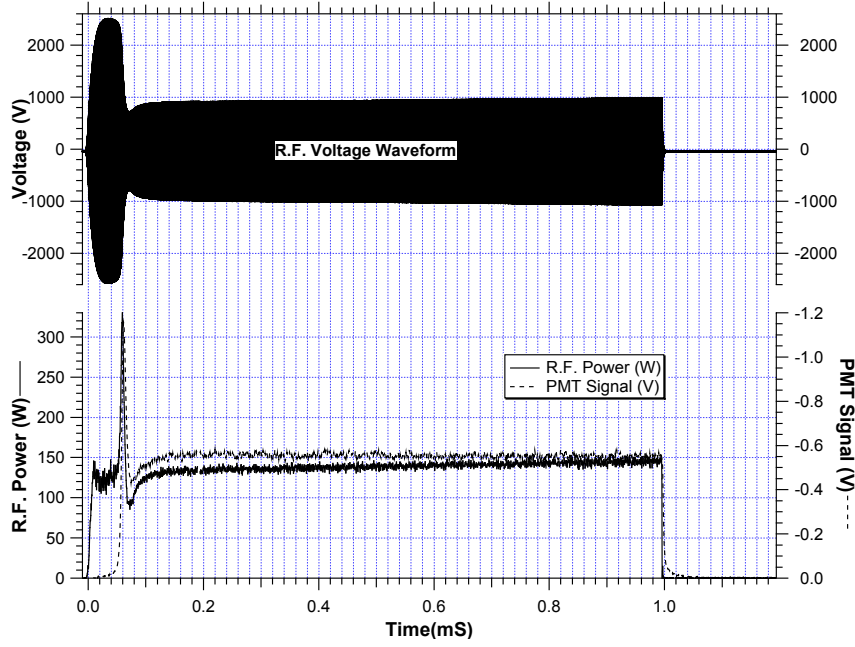
One complete rf voltage pulse at 100 Hz with 10% duty cycle in 5 mTorr of argon is shown on the upper axes of figure 4. The corresponding time-dependent rf power along with the PMT signal is plotted on the lower axes of figure 4. To make comparisons between the PMT signal and the rf power measurements, the recorded PMT waveforms were block-averaged over 0.5  $\mu\text{s}$  segments. Clearly, a region of high power loading of the plasma occurs during the initial stage of the rf pulse. All three curves display a large transient effect and indicate, approximately, the same time of around 50  $\mu\text{s}$  after the pulses are applied to the ICP load. Furthermore, both the rf power and the PMT signal show similar behaviour. The fact that the PMT signal reflects the behaviour of the rf power delivered shows that the power ‘spike’ observed is neither an artifact of the measurement process nor some resonant phenomena associated with the matching network, but instead reflects true increased power to the plasma. The data shown in figure 4 were obtained with the rf power level set to 100 W on the generator front panel controls. It is tempting to draw an analogy between this observed transient and normal breakdown in a glow discharge. However, as will be discussed later, a weakly ionized plasma starts to form within the first 10  $\mu\text{s}$ , thus breakdown in the traditional sense occurs very early in the initiation of the rf pulse.

Figure 5 shows more detail of the early part of the pulse with the rf power level set to 200 W on the generator front panel and the same pulse parameters as those in figure 4. The lower axes of figure 5 show rf power, PMT signal, and rf power delivered to the coil. The rf power delivered to the coil is calculated by

$$P_{coil} = \frac{V_{coil,peak} I_{meas,peak}}{2} \cos(\phi) \quad (7)$$

where  $I_{meas,peak}$  is the peak rf current measured by the probe and  $V_{coil,peak}$  is the peak voltage across the coil. The coil voltage  $V_{coil}$  is given by

$$V_{coil} = R_{coil} I_{meas} + L_{coil} \frac{dI_{meas}}{dt} \quad (8)$$



**Figure 4.** Rf voltage waveform (upper curve), and rf power and PMT signal (lower curves) for a 100 Hz, 10% duty cycle rf pulse in 5 mTorr argon. The rf power supply was set at 100 W.

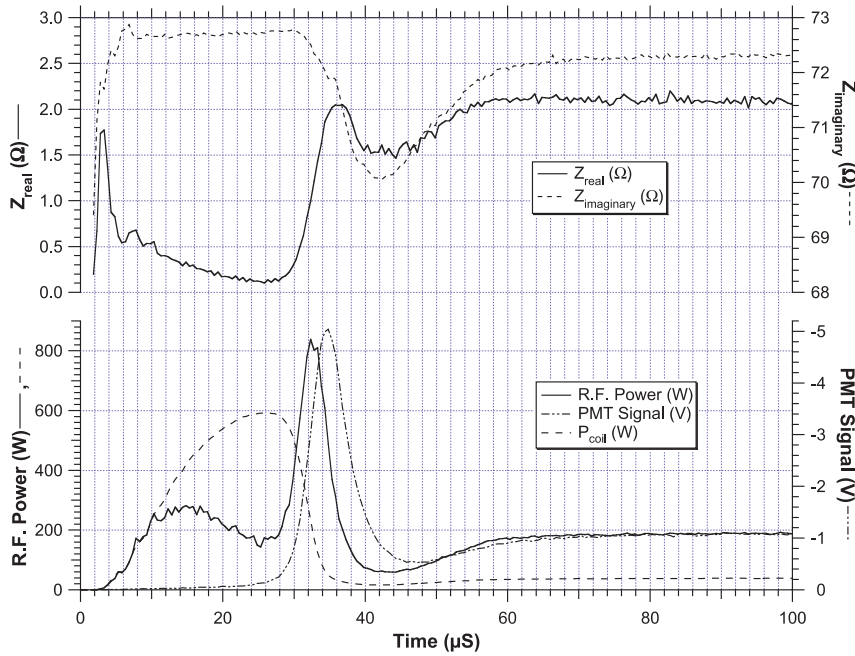


**Figure 5.** Details of the transient region,  $Z_{real}$  and  $Z_{imaginary}$  (upper curves); rf power calculated from equations (1) and (2), PMT signal and  $P_{coil}$  (from equation (7)) for a 100 Hz, 10% duty cycle rf pulse in 5 mTorr argon. The rf power supply was set at 200 W.

where  $I_{meas}$  is the rf current measured by the probe,  $R_{coil}$  is the measured resistance of the coil, and  $L_{coil}$  is the measured inductance of the coil. The measured values of  $R_{coil}$  and  $L_{coil}$  are derived from current and voltage measurements made *in situ* on the coil under ‘no plasma’ conditions and are determined from the measured impedance of the coil. In general, the real and imaginary parts of the system impedance can be calculated by

$$Z_{real} = \frac{V_P}{I_P} \cos(\phi) \quad (9)$$

and

$$Z_{imaginary} = \frac{V_P}{I_P} \sin(\phi) \quad (10)$$

where  $V_P$ ,  $I_P$ , and  $\phi$  are defined as in equation (2) and are determined by both the DFT and LSF methods. We then set  $R_{coil} \equiv Z_{real}$  (‘no plasma’) and  $L_{coil} \equiv (1/\omega)Z_{imaginary}$  (‘no plasma’). In practice,  $R_{coil}$  and  $L_{coil}$  were obtained from the cw calibration runs discussed previously. From ten measurements over a cw power range of 1–500 W the values for  $R_{coil}$  and  $L_{coil}$  as defined above were  $0.421 \pm 0.007 \Omega$

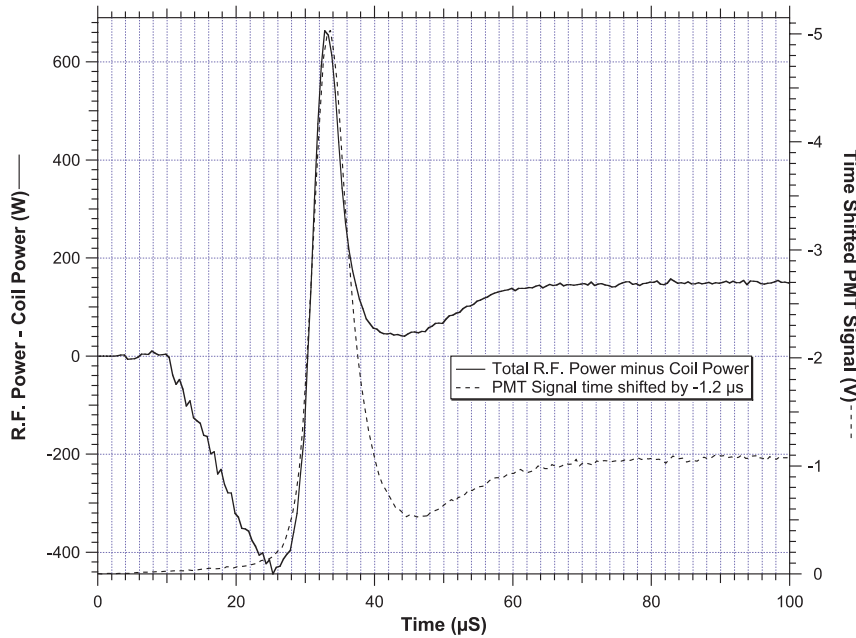


**Figure 6.** Net rf power and time-shifted PMT signal under the same conditions as figure 5.

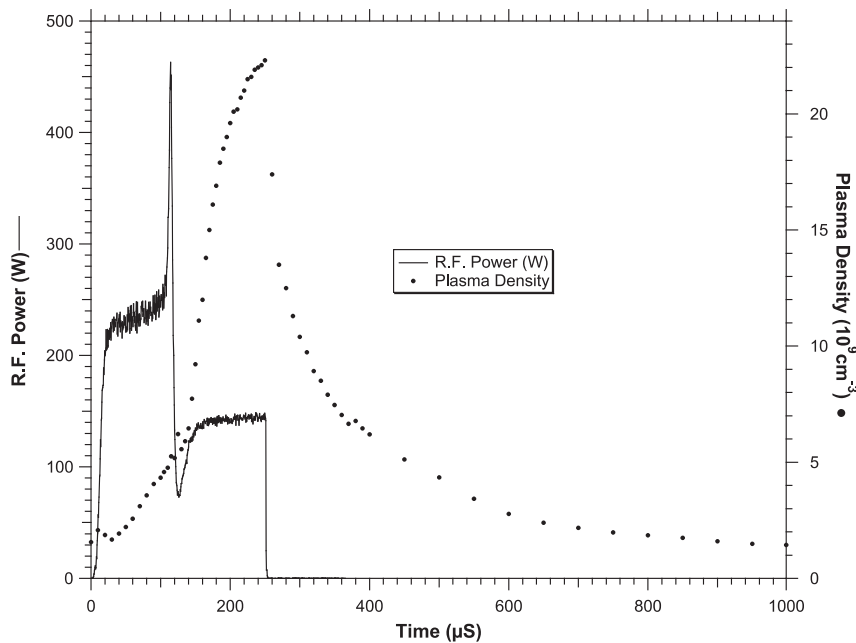


**Figure 7.** Rf power and measured plasma density (from Langmuir probe) for a 1 kHz, 25% duty cycle rf pulse in 5 mTorr argon. The rf power supply was set at 150 W.

and  $0.858 \pm 0.003 \mu\text{H}$ , respectively. The power to the coil calculated by equations (7) and (8) assumes that all of the measured current flows through the coil. While this is a reasonable assumption under inductive coupling by the plasma, it overestimates the power to the coil under capacitive coupling conditions. This will be shown later in the data. The upper axes show the time-dependent  $Z_{real}$  and  $Z_{imaginary}$  obtained from the current and voltage measurements. Following the application of the rf pulse,  $Z_{real}$  briefly increases due to the rapidly changing rf current amplitude then drops back to the  $0.42 \Omega$  of the coil at approximately  $10 \mu\text{s}$ . At this point  $Z_{real}$  decreases below the coil resistance until the transient

begins, at which time  $Z_{real}$  rapidly increases by a factor of more than 10. On the other hand,  $Z_{imaginary}$  decreases by only about 4% briefly during the transient and then recovers to within 1% of the coil value during the remainder of the pulse. Watanabe *et al* [18] show that when the plasma is capacitively coupled the real part of the discharge impedance,  $R_{cc}$ , appears in parallel with the real part of the coil impedance, while under inductively coupled conditions the real part of the discharge impedance,  $R_{ic}$ , appears in series with the real part of the coil impedance. This is seen in the behaviour of  $Z_{real}$  during the pulse. Following the initial  $10 \mu\text{s}$ ,  $Z_{real}$  drops below the  $0.42 \Omega$  resistance of the coil, indicating a resistance in parallel with

the coil resistance. This indicates a weakly ionized plasma has formed within the first 10  $\mu\text{s}$  and the initial coupling to the plasma is capacitive. At its minimum  $Z_{real}$  drops to approximately  $0.12 \Omega$ , which gives  $R_{cc} \approx 0.17 \Omega$ . After the transient,  $Z_{real}$  is larger than the coil resistance, indicating a resistance in series with the coil resistance. Following the transient,  $Z_{real}$  stabilizes at approximately  $2.1 \Omega$ , which gives  $R_{ic} \approx 1.7 \Omega$ . Hence in the transient region the discharge changes from capacitive to inductive coupling. This is also seen in the lower axes of figure 5 by comparing the rf power calculated from equations (1) and (2) and the power delivered to the coil,  $P_{coil}$ , calculated from equation (7). For, roughly, the first 10  $\mu\text{s}$  after application of the rf pulse, all of the rf power delivered shows up in the coil. At somewhat later times, but before the transient,  $P_{coil}$  exceeds the total rf power, which is physically impossible. The region where the coil power exceeds the total power occurs because the real part of the coil/plasma system has decreased below that of the coil alone. Hence the measured power is less than one would calculate assuming the resistance of the coil is the real part of the system impedance. As previously discussed, this indicates a real component in parallel with the coil resistance and indicates the plasma is capacitively coupled. Another way of looking at this is that the peak current used in equation (7),  $I_{meas, peak}$ , is larger than that which actually flows through the coil due to the capacitance of the discharge. After the transient, the power to the coil is only about 20% of the total rf power. After observing this capacitive coupling scheme, this region was also checked for harmonic content (as discussed in section 5) with no measurable power in the harmonics. The origin of the power 'spike' observed at the transition from capacitive to inductive load is not clear. The rf power supply is designed to run at constant power under changing load conditions. It is not clear, however, how fast the supply can adjust to this changing load. Before the transition region the rf voltage is very high in order to maintain the set power through the inductive load. After the transition region, the rf voltage is reduced to maintain the same power through the more resistive load of the plasma/coil. The 'spike' may simply be the result of the power supply's inability to reduce voltage fast enough to compensate for the rapidly changing load from the plasma. It is also seen in figure 5 that the PMT signal trails the rf power 'spike' by approximately 2  $\mu\text{s}$ . This time delay is the result of two effects. First of all, the SR 560 amplifier adds, approximately, a 1.2  $\mu\text{s}$  delay to the PMT signal. Second, the rf power 'spike' includes both power to the coil and power to the plasma. If one subtracts the coil power from the total power this skews the rf power spike approximately 0.7  $\mu\text{s}$  to later times.

The result of this is shown in figure 6 where the 'net' rf power (total minus coil) is compared with the PMT signal shifted by 1.2  $\mu\text{s}$  to remove the amplifier delay. The curves then overlap to within the 0.5  $\mu\text{s}$  window over which the data is averaged. In figure 7, total power measured is plotted along with time-resolved Langmuir probe data. This is for a 1 kHz repetition rate at a 25% duty cycle with the rf supply set for 150 W. In spite of higher rf power before the power 'spike', the probe data shows a more gradual increase in the plasma density, and a much more rapid increase in the plasma density following the 'spike'. This in all probability reflects the more efficient coupling between the coil and the plasma in the inductively

coupled mode. No transient effects, as seen in the rf power data and PMT data, are seen in the probe data. This is most likely to be due to the position of the probe tip which is 20 cm away from the rf window of the plasma source. The rapid changes in the plasma density will tend to be 'washed out' by diffusion to the probe. To increase the time resolution in the probe data, it is necessary, as part of future research, to place the tip inside the plasma source.

## 7. Conclusions

The results presented have demonstrated the successful application of a time-resolved technique for characterizing a pulsed rf ICP. Power has been measured with an accuracy of better than 10% from segments of digitized current and voltage waveforms. Hardware design has been implemented in the experiment to minimize stray capacitance and to ensure better signal sampling with careful positioning of the probes near the coil. These measures proved to be very important in reproducing measurements for calibration purposes. Furthermore, to apply the technique, one must use an oscilloscope that has at least two channels with the following capabilities: (1) long recording capability, (2) high digitizing rate (at least 2 GHz) and (3) high timing accuracy (of the order of 7 ps). By measuring the complex impedance of the system during the rf pulse, the transition of the plasma from capacitive to inductive coupling was observed. The observation of a sharp 'spike' in the rf power delivered to the plasma during the pulse coincides with a rapid rise in the real part of the load impedance and a rapid fall in the rf voltage. Finally, the results are verified with time-resolved Langmuir probe and PMT measurements.

The motivation for this work was the need to accurately determine the rf power into a pulsed ICP. Because of the inductive nature of the load, significant effort is required to obtain accurate measurements using what would appear to be a simple technique. For pulsed power measurements we feel the results justify the effort, especially when compared to the results obtained using traditional power meters with a pulsed system. For cw measurements this is probably not the case. Existing power meters which measure the rf power into the matching network are probably adequate for all but the most detailed work.

## Acknowledgment

This work was supported by The Air Force Office of Scientific Research.

## References

- [1] Coultas D K and Keller J H 1990 *European Patent Application* 0379828A2
- [2] Ogle J S 1990 *US Patent Specification* 4,948,458
- [3] Hopwood J, Guarnieri C R, Whitehair S J and Cuomo J J 1993 *J. Vac. Sci. Technol. A* **11** 147
- [4] Hopwood J, Guarnieri C R, Whitehair S J and Cuomo J J 1993 *J. Vac. Sci. Technol. A* **11** 152
- [5] Hopwood J 1993 *Appl. Phys. Lett.* **62** 940
- [6] Mahoney L J, Wendt A E, Barrios E, Richards C J and Shohet J L 1994 *J. Appl. Phys.* **76** 2041
- [7] Wainman P N, Lieberman M A, Lichtenberg A J, Stewart R A and Lee C 1995 *J. Vac. Sci. Technol. A* **13** 2464

- 
- [8] Miller P A, Hebner G A Greenberg K E, Pochan P D and Aragon B P 1995 *J. Res. Natl Inst. Stand. Technol.* **100** 427
- [9] Ashida S, Lee C and Lieberman M A 1995 *J. Vac. Sci. Technol. A* **13** 2498
- [10] Trottenberg Th, Melzer A and Piel A 1995 *Plasma Sources Sci. Technol.* **64** 450
- [11] Samukawa S and Mieno T 1996 *Plasma Sources Sci. Technol.* **5** 132
- [12] Sugai H and Nakamura K 1995 *J. Vac. Sci. Technol. A* **13** 887
- [13] Charles C, Boswell R W and Kuwahara H 1995 *J. Appl. Phys.* **67** 40
- [14] Boswell R W and Vender D 1995 *Plasma Sources Sci. Technol.* **4** 534
- [15] Ashida S, Shim M R and Lieberman M A 1996 *J. Vac. Sci. Technol. A* **14** 391
- [16] Sobolewski M A 1992 *J. Vac. Sci. Technol. A* **10** 3550
- [17] Sobolewski M A 1998 *Appl. Phys. Lett.* **72** 1146
- [18] Watanabe M, Shaw D M, Collins G J and Sugai H 1999 *J. Appl. Phys.* **85** 3428

### **2.3 Time-Resolved Langmuir-Probe Measurements on Pulsed ICP Source**

A commercial Langmuir-probe system that can be operated in a boxcar averaging mode was used to measure time-resolved electron and ion densities and electron temperatures on a repetitively pulsed ICP in argon. The probe was positioned inside the ICP source region, near the rf window, to follow closely the temporal variation of the plasma parameters with time resolution of  $\sim 7 \mu\text{s}$ . The rf power at 13.56 MHz was pulsed by applying 100% square-wave modulation to the output of an rf generator that was capable of supplying up to 5 kW cw output. Modulation frequencies could be varied between 100 Hz and 30 kHz, with duty cycles between 10% and 90%. Along with the Langmuir-probe data, current and voltage measurements at the coil were used to measure time-resolved rf power and complex impedance of the coil-plasma system with a time resolution of  $0.5 \mu\text{s}$ . A photomultiplier tube (PMT) with narrow band filter was used to monitor the time dependence of the plasma emission. At lower rep rates and/or duty cycles, the ICP changed from capacitively coupled to inductively coupled during the rf pulse. During this transition a large transient was observed in the rf power, plasma emission, and electron and ion densities. Results were obtained for a variety of rep rates, duty cycles, and rf powers.

The results of this investigation were documented by Wei Guo (ISSI) and Charles DeJoseph, Jr. (AFRL) in a paper that was presented at the 28<sup>th</sup> IEEE International Conference on Plasma Science, 2001.

### **2.4 Plasma Diagnostics on Pulsed Argon ICP Source**

A planar ICP source was characterized using current and voltage probes, a commercially built Langmuir-probe system, and a fast photomultiplier with narrow-band filter. The rf supply operated at 13.56 MHz and could be 100% power modulated to allow pulsed operation of the source. By digitally recording long current and voltage waveforms and using accurate phase correction for the electronics, time resolved rf power and complex impedance were measured during a pulse. With the Langmuir probe operated in a boxcar mode, time-resolved electron and ion densities along with electron temperatures were also measured. Data were obtained for rep rates between 1 KHz and 10 KHz and duty cycles of 10% and 25% with average powers (during the pulse) from 50 to 500 W. The behavior of the complex impedance showed that the discharge was capacitively coupled at the beginning of a pulse and later became inductively coupled. During a single pulse the plasma exhibited a sharp peak in power loading, which was also observed in the photomultiplier signal and the plasma density. Peak plasma densities on the order of  $10^{12} \text{ cm}^{-3}$  were measured.

The results of this investigation were documented by Charles DeJoseph, Jr. (AFRL) and Wei Guo (ISSI) in a paper that was presented at the 54<sup>th</sup> Annual Gaseous Electronics Conference, 2001. The visual materials for this presentation are included on subsequent pages.

# PLASMA DIAGNOSTICS ON A PULSED ARGON ICP SOURCE



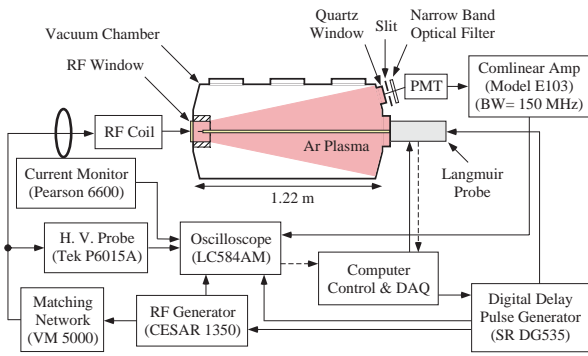
**Charles A. DeJoseph, Jr.**  
**Air Force Research Laboratory**  
**Wei Guo**  
**Innovative Scientific Solutions, Inc.**  
**(ISSI)**

## ABSTRACT

A planar inductively coupled plasma (ICP) source is characterized using current and voltage probes, a commercially-built Langmuir probe system, and a fast photomultiplier with narrow band filter. The rf supply operates at 13.56 MHz and can be 100% power modulated to allow pulsed operation of the source. By digitally recording long current and voltage waveforms and using accurate phase correction for the electronics, time resolved rf power and complex impedance are measured during a pulse. With the Langmuir probe operated in boxcar mode, time resolved electron and ion densities along with electron temperatures are also measured. Data will be presented for rep rates between 1 KHz and 10 KHz and duty cycles of 10% and 25% with average powers (during a pulse) from 50 to 500 watts. It will be shown from the behavior of the complex impedance that the discharge is capacitively coupled at the beginning of a pulse and later becomes inductively coupled. During a single pulse the plasma exhibits a sharp peak in power loading which is also seen in the photomultiplier signal and the plasma density. Peak plasma densities on the order of  $10^{12} \text{ cm}^{-3}$  have been measured.

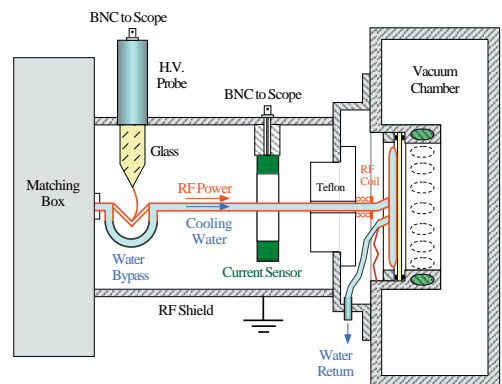
ISSI

## SCHEMATIC OF THE EXPERIMENT



ISSI

## RF COUPLER SECTION



ISSI

## TIME RESOLVED RF POWER MEASUREMENTS

- METHOD:** Compute power from segments of digitized current and voltage waveforms.
  - Current and voltage probes plus digital oscilloscope
- PROBLEM:** Phase must be measured very accurately since current and voltage are near 90° out of phase. Given  $f=13.56\text{MHz}$ ,
 
$$P = \frac{V_p I_p}{2} \cos(\phi) = \frac{V_p I_p}{2} \cos\left(\frac{\pi}{2} - \delta\right) = \frac{V_p I_p}{2} \sin(\delta) \approx \frac{V_p I_p}{2} \delta$$

$$\frac{\Delta P}{P} \approx \frac{\Delta \delta}{\delta}$$
 From our coil:  $R = 0.77\ \Omega$ ,  $L = 1.21\ \mu\text{H}$ ,  $TAN(\phi) = \frac{\omega L}{R}$ ,  $\delta = 7.5 \times 10^{-3}\ \text{rad}$ 

$$\text{For } \frac{\Delta P}{P} = 10\%, \Delta \delta \approx 0.8\ \text{mrad}, \text{ and } \Delta t = \frac{\Delta \delta}{\omega} \approx 9\ \text{pS}$$

ISSI

## RF POWER MEASUREMENTS (CONT.) CURRENT AND VOLTAGE MEASUREMENTS

- Phase calibration is done using c.w. power by assuming all power goes into coil when no plasma is present (vacuum).
  - Phase calibration consists of a constant correction due to cable and probe delays and a "variable" correction due to scope gain and slew rate. Variable correction depends on amplitude of current and voltage waveforms.
- Chief source of error in power measurement is uncertainty in phase determination. For all plasma conditions  $\phi \approx 90^\circ$ , so:
 
$$\Delta P \approx \frac{V_p I_p}{2} |\sin(\phi)| \Delta \phi \approx \frac{V_p I_p}{2} \Delta \phi$$
  - In practice,  $\Delta \phi$  is found to be  $\approx 0.5\ \text{mrad}$
- Harmonic content is found to be negligible ( $<0.2\%$ ) in all measurements

ISSI

## RF POWER MEASUREMENTS (CONT.) METHOD OF CALCULATION

- RF Power computed by three methods (sanity check):
  - Discrete Fourier Transform (DFT)
  - Integral of I-V over N-periods
  - Least-squares fit to sine function
- Details:
  - DFT and least-squares methods give phase ( $\phi$ ), peak voltage ( $V_p$ ), and peak current ( $I_p$ ) directly. Power is
 
$$P = \frac{V_p I_p}{2} \cos(\phi)$$
  - For integral method:  $P = \frac{1}{T} \int_0^T V(t)I(t)dt$ 

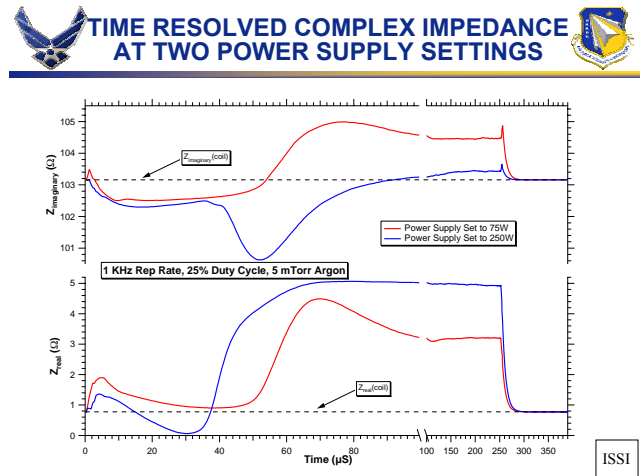
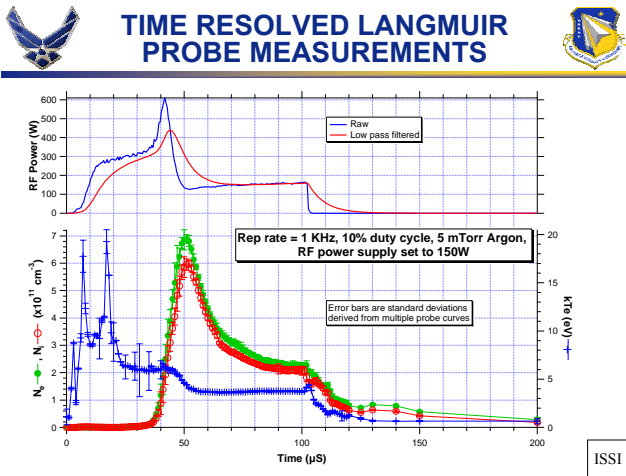
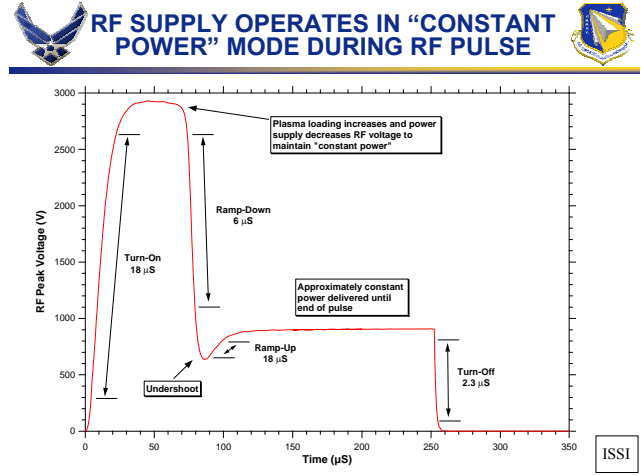
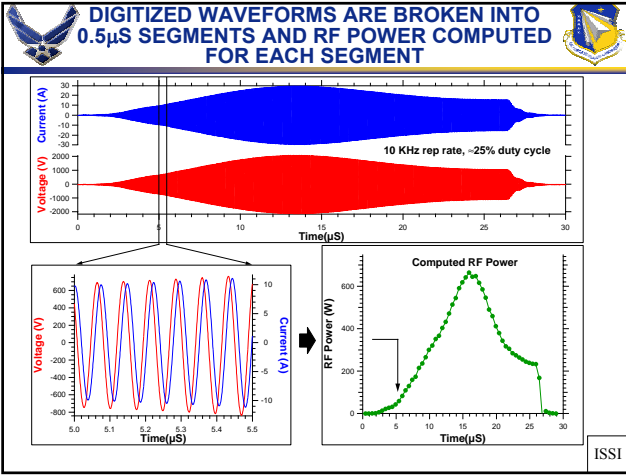
$$V_p = \left[ \frac{2}{T} \int_0^T V(t)^2 dt \right]^{1/2} \quad I_p = \left[ \frac{2}{T} \int_0^T I(t)^2 dt \right]^{1/2} \quad \phi = \cos^{-1} \left( \frac{2P}{V_p I_p} \right)$$
  - For all methods:  $Z_{imaginary} = \frac{V_p}{I_p} \sin(\phi)$   $Z_{real} = \frac{V_p}{I_p} \cos(\phi)$

ISSI

## LANGMUIR PROBE MEASUREMENTS

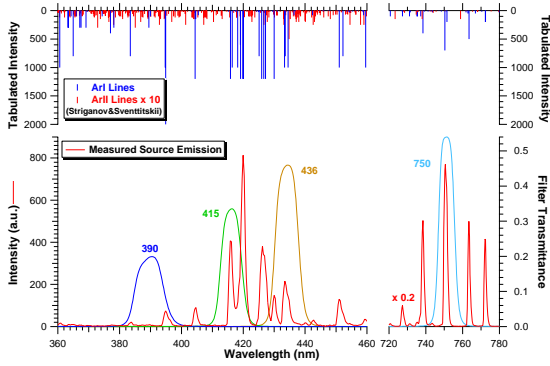
- Langmuir probe is commercial system (Scientific Systems, Inc.) with scanning capability
  - System is operated in boxcar mode with variable delay from initiation of RF pulse
  - Time constant for probe measurements is  $\approx 7\ \mu\text{S}$ 
    - Data from current and voltage measurements or photomultiplier data must be convolved with low pass filter before comparison with Langmuir probe data

ISSI





## TIME RESOLVED EMISSION WAS ACQUIRED USING FOUR DIFFERENT NARROW-BAND FILTERS: 390, 415, 436, AND 750 nm



ISSI



## NEUTRAL ARGON LINES SELECTED BY EACH FILTER



### 390 nm

Wavelength	Intensity	E <sub>l</sub> (eV)	E <sub>u</sub> (eV)	Lower State	Upper State
3834.679	800	11.83	15.06	4s11/21	6p11/20
3864.287	10	11.83	15.03	4s11/21	6p3/22
3866.275	5	11.83	15.03	4s11/21	6p3/21
3876.060	10	11.83	15.03	4s11/21	6p5/22
3894.660	300	11.83	15.01	4s11/21	6p11/21
3899.978	100	11.72	14.90	4s11/20	4p3/21
3947.665	1000	11.55	14.69	4s3/22	5p3/22
3948.979	2000	11.85	14.69	4s3/22	5p11/21
3979.715	10	11.62	14.74	4s3/21	5p11/20

### 415 nm

Wavelength	Intensity	E <sub>l</sub> (eV)	E <sub>u</sub> (eV)	Lower State	Upper State
4158.591	1200	11.55	14.53	4p3/22	5s3/22
4164.180	1000	11.55	14.52	4s3/22	5p3/21
4181.884	1000	11.72	14.69	4s11/20	5p11/21
4190.714	600	11.55	14.51	4s3/22	5s5/22
4191.029	1200	11.72	14.66	4s11/20	5p3/21
4198.318	1200	11.62	14.58	4s3/21	5s11/20
4200.675	1200	11.55	14.50	4s3/22	5s5/23

### 436 nm

Wavelength	Intensity	E <sub>l</sub> (eV)	E <sub>u</sub> (eV)	Lower State	Upper State
4272.189	1200	11.82	14.52	4s3/21	5s3/21
4300.101	1200	11.82	14.51	4s3/21	5s5/22
4333.561	1000	11.83	14.69	4s11/21	5p3/22
4335.338	800	11.83	14.69	4s11/21	5p11/21
4345.187	1000	11.83	14.66	4s11/21	5p3/21
4363.786	80	11.62	14.46	4s3/21	5s11/21
4423.995	80	11.72	14.52	4s11/20	5p3/21

### 750 nm

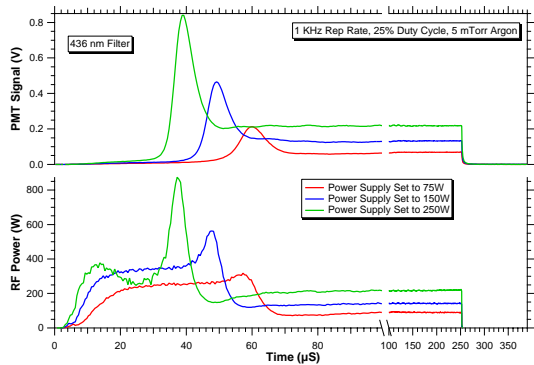
Wavelength	Intensity	E <sub>l</sub> (eV)	E <sub>u</sub> (eV)	Lower State	Upper State
7412.334	15	13.28	14.85	4p3/21	4p11/22
7422.260	6	13.28	14.95	4p3/21	4p15/22
7426.290	12	13.30	14.97	4p3/22	4p15/23
7436.330	30	13.17	14.84	4p3/22	6s3/22
7438.250	10	13.08	14.74	4p3/23	4s3/22
7471.168	4	11.62	13.28	4s3/21	4p3/21
7484.240	15	13.15	14.81	4p3/21	4s5/22
7503.869	700	11.83	13.48	4s11/21	4p11/20
7510.420	10	13.30	14.95	4p3/22	4p15/22
7514.651	200	13.62	13.27	4s3/21	4s11/20
7618.330	30	13.33	14.95	4p11/21	4p13/22

From Striganov and Sventitskii

ISSI



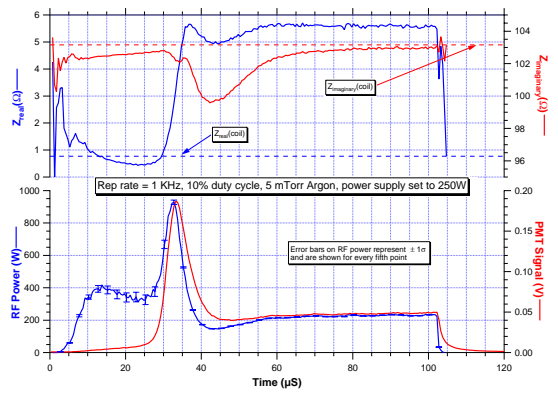
## TYPICAL PMT SIGNAL AT THREE DIFFERENT POWER SUPPLY SETTINGS



ISSI

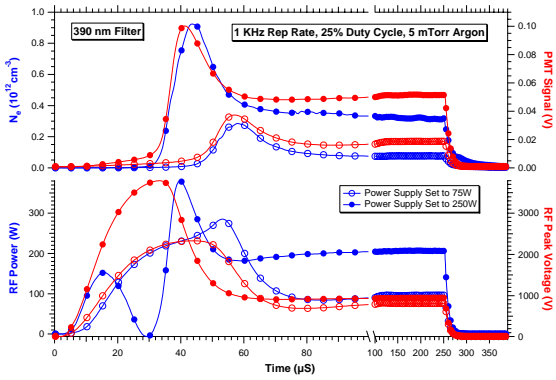


## DATA FROM TIME RESOLVED CURRENT AND VOLTAGE MEASUREMENTS



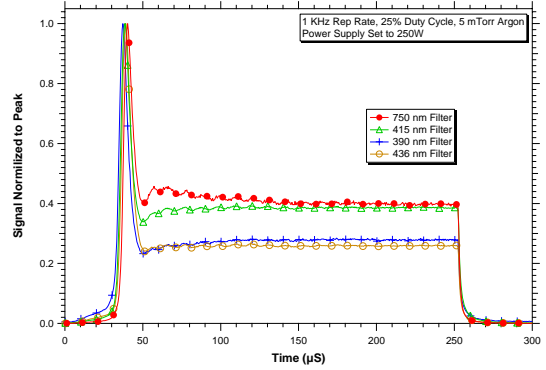
ISSI

**TIME RESOLVED RF POWER, PEAK VOLTAGE, ELECTRON DENSITY, AND PMT SIGNAL AT TWO POWER SUPPLY SETTINGS**



ISSI

**SHAPE OF PMT SIGNAL DEPENDS ON CHOICE OF OPTICAL FILTER**



ISSI

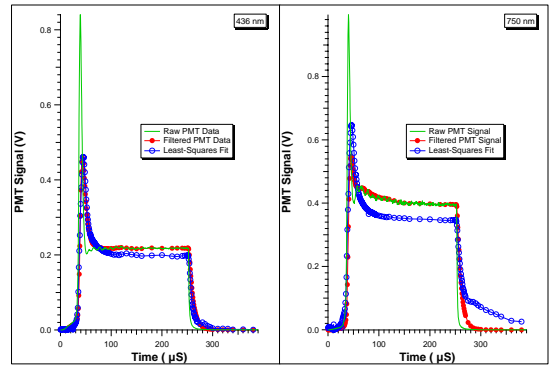
**EMPIRICALLY, CONSIDER A SIMPLE MODEL FOR EMISSION**

$$S_F(t) = \int S(t')F(t-t')dt' = cn_e(t)^a \exp\left[-\frac{b}{kT_e(t)}\right]$$

- $S(t)$  = measured PMT signal
- $S_F(t)$  = low-pass filtered PMT signal
- $F(t)$  = low-pass filter function ( $\tau=7\mu\text{s}$ )
- $n_e(t)$  = measured electron density
- $kT_e(t)$  = measured electron temperature
- $c, a, b$  = constants

ISSI

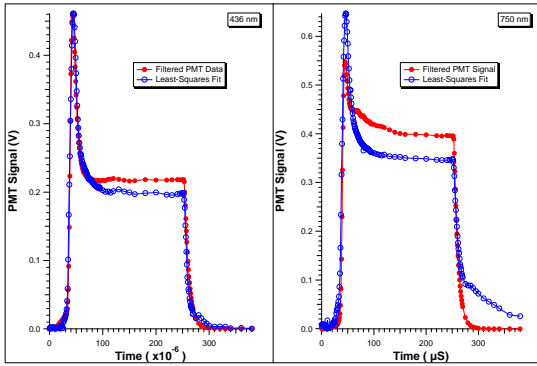
**390 AND 436 DATA FIT MODEL WELL- 750 AND 415 DO NOT**



ISSI



## 390 AND 436 DATA FIT MODEL WELL- 750 AND 415 DO NOT



ISSI



## FOR 436 nm, SIMPLE MODEL DESCRIBES DATA WELL



$$S_F(t) = cn_e(t)^a \exp\left[-\frac{b}{kT_e(t)}\right]$$

$$a = 2/3 \pm 0.02, b = 3 \pm 0.2 \text{ eV}$$

1)  $b = 3 \text{ eV}$  implies excitation is likely from metastable level (either  $4s[3/2]2$  at 11.55 eV or  $4s'[1/2]0$  at 11.72 eV)

2) Based on (1) above;  $a = 2/3$  implies metastable population goes like  $n_e^{-1/3}$  ????????

ISSI



## SUMMARY AND CONCLUSIONS



- Time resolved RF current and voltage, Langmuir probe, and optical emission data have been obtained on a pulsed ICP at 13.56 MHz
- Complex impedance measurements indicate discharge transitions from predominately capacitive coupling to inductive coupling during pulse
- Simple model describes time dependent behavior of emission for 390 and 436 nm narrow band filters.
  - Model implies that emission is predominately by excitation from metastable levels

ISSI

### 3.0 MEASUREMENTS IN NITROGEN PULSED ICP

#### 3.1 Investigation of Mode Transitions in Pulsed ICP System

Mode transitions in a low-pressure, repetitively pulsed, rf (13.56-MHz)-excited ICP source were investigated using current and voltage probes on the rf coil. In addition, time-resolved Langmuir-probe measurements of electron temperature, plasma potential, and plasma density were made during these mode transitions. A third diagnostic utilized a fast photomultiplier with narrow-band filters to monitor time-resolved plasma emission. Argon was used as a representative atomic gas, while nitrogen was used as a representative molecular gas. Both pure gases and mixtures were used in the experiment. During a single rf pulse, the discharge was observed to run either capacitively coupled or to change from capacitive to inductive mode. Once the transition was made to the inductive mode, it was active until the end of the pulse. The observed mode changes were a function of pulse width, rf power, gas pressure, and gas mixture. By comparing the Langmuir-probe data from each mode and during a transition, a set of criteria based on the plasma characteristics was established to predict the operating mode of this ICP. Results were obtained for plasmas generated under various conditions.

The results of this investigation were documented by Wei Guo (ISSI) and Charles DeJoseph Jr. (AFRL) in a paper that was presented at the 29<sup>th</sup> IEEE International Conference on Plasma Science, 2002.

#### 3.2 Time-Resolved Rotational Temperature Measurements of N<sub>2</sub> and N<sub>2</sub><sup>+</sup> in Pulsed ICP

A planar ICP source was operated at 14.56 MHz with 100% power modulation of the rf supply. Repetition rate and duty cycle were variable, but typical values were 1 KHz and 25%. A half-meter spectrometer with a gated, intensified CCD array was used to acquire time-resolved emission spectra from the N<sub>2</sub>(C-B) and the N<sub>2</sub><sup>+</sup>(B-X) band systems at pressures of 10-20 mTorr in pure N<sub>2</sub>. The limited spectral resolution of the system (0.1 nm) and the complexity of the emission prevented the use of Boltzmann plots to obtain rotational temperatures; therefore, a computed spectrum was least-squares fit to the measured band contours. The computed spectrum was a detailed line-by-line calculation that was convolved with the spectrometer instrumental line-shape function. Spectra containing overlapping bands from both systems could be fit simultaneously, with different temperatures assigned to each system. Rotational temperatures were obtained for each band system at gate widths of 0.5 μs and gate delays over the time span of the rf pulse. These data were compared with time-resolved rf power, complex impedance, and Langmuir-probe measurements.

The results of this study were documented by Charles DeJoseph, Jr. (AFRL), Wei Guo (ISSI), J. Heggemeier (University of Minnesota) in a paper that was presented at the 55<sup>th</sup> Annual Gaseous Electronics Conference, 2002. The visual materials for this presentation are included on subsequent pages.

# TIME RESOLVED ROTATIONAL TEMPERATURE MEASUREMENTS OF $N_2$ AND $N_2^+$ IN A PULSED ICP



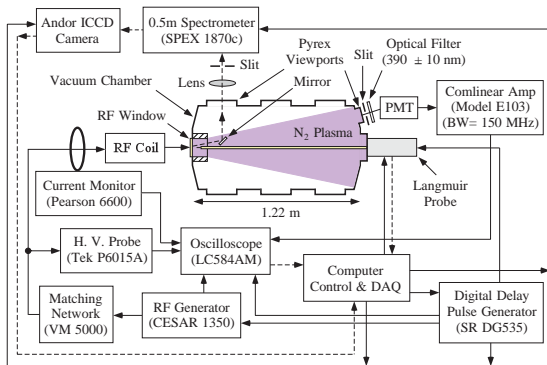
Charles A. DeJoseph, Jr.  
Air Force Research Laboratory  
Wei Guo  
Innovative Scientific Solutions, Inc.  
(ISSI) and  
Jeffry P. Heggemeier  
Dept. of Electrical Engineering,  
Univ. of Minnesota

## Abstract

A planar inductively coupled plasma (ICP) source is operated at 13.56 MHz with 100% power modulation of the rf supply. Repetition rate and duty cycle are variable but typical values are 1 KHz and 25%. A half-meter spectrometer with a gated, intensified CCD array is used to acquire time resolved emission spectra from the  $N_2$ (C-B) and the  $N_2^+$ (B-X) band systems at pressures of 10-20 mTorr in pure  $N_2$ . The limited spectral resolution of the system (0.1 nm) and the complexity of the emission prevent using "Boltzmann plots" to obtain rotational temperatures, so a computed spectrum is least-squares fit to the measured band contours. The computed spectrum is a detailed line-by-line calculation convolved with the spectrometer instrumental line shape function. Spectra containing overlapping bands from both systems can be fit simultaneously with different temperatures assigned to each system. Rotational temperatures obtained for each band system at gate widths of  $0.5\mu s$  and gate delays over the time span of the rf pulse will be presented. These data will be compared with time resolved rf power, complex impedance, and Langmuir probe measurements.

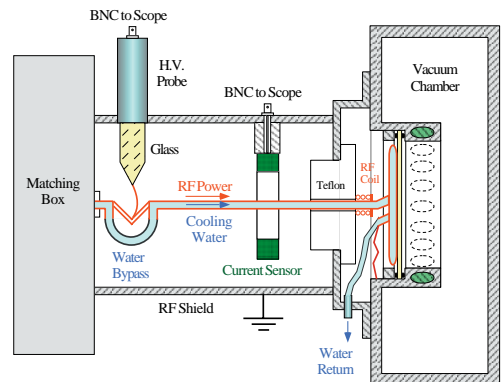
ISSI

## Schematic of the Experiment



ISSI

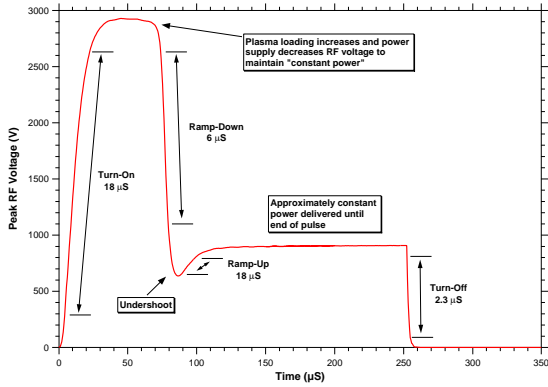
## Rf Coupler Section



ISSI



## Rf Supply Operates In "Constant Power" Mode During Rf Pulse



ISSI



## Time Resolved Rf Power Measurements



- METHOD:** Compute power from segments of digitized current and voltage waveforms.
  - Current and voltage probes plus digital oscilloscope
- PROBLEM:** Phase must be measured very accurately since current and voltage are near 90° out of phase. Given  $f=13.56\text{MHz}$ ,

$$P = \frac{V_r I_r}{2} \cos(\phi) = \frac{V_r I_r}{2} \cos\left(\frac{\pi}{2} - \delta\right) = \frac{V_r I_r}{2} \sin(\delta) \approx \frac{V_r I_r}{2} \delta$$

$$\frac{\Delta P}{P} \approx \frac{\Delta \delta}{\delta}$$

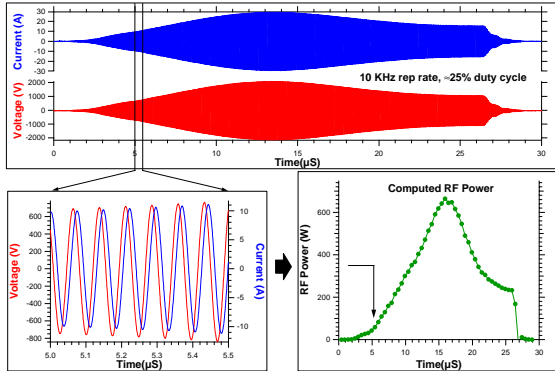
From our coil :  $R = 0.77 \Omega$ ,  $L = 1.21 \mu\text{H}$ ,  $TAN(\phi) = \frac{\omega L}{R}$ ,  $\delta = 7.5 \times 10^{-3} \text{ rad}$

$$\text{For } \frac{\Delta P}{P} = 10\%, \Delta \delta \approx 0.8 \text{ mrad, and } \Delta t = \frac{\Delta \delta}{\omega} \approx 9 \text{ pS}$$

ISSI



## Digitized Waveforms are Broken into 0.5µs Segments and Rf Power Computed for Each Segment



ISSI



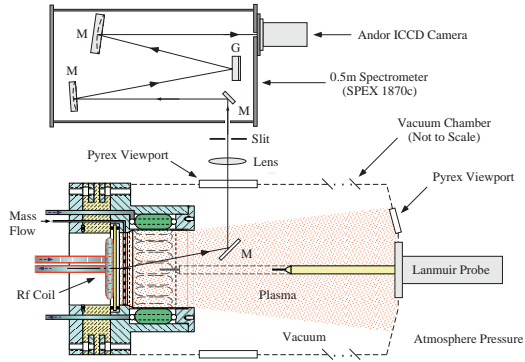
## Time Resolved Rotational Temperature Measurements



- Use intensified, gated CCD array with half-meter spectrometer to capture a time series of emission spectra from the RF discharge
  - Optimize data collection for early, middle, and late in RF pulse by varying gain, gate width, and signal averaging time
- Use detailed line-by-line calculation to synthesize emission spectrum of  $N_2(\text{C-B})$  (2<sup>nd</sup> positive system) and  $N_2^+(\text{B-X})$  (1<sup>st</sup> negative system) – assume optically thin
  - Use least-squares fit to determine rotational temperature of each band system and relative vibrational upper state densities
  - Use different spectral regions to optimize signal for each band system and check consistency of measurements

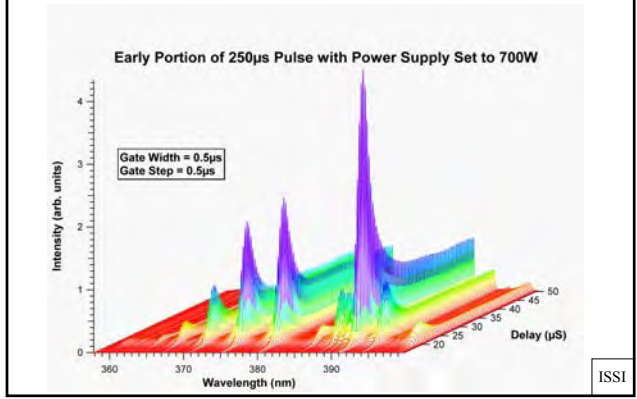
ISSI

## Detail of the Emission Spectrometer Interface



ISSI

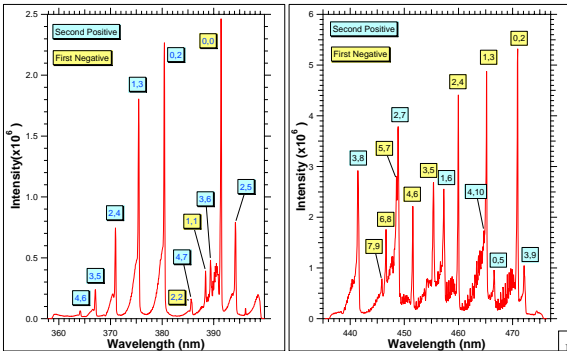
## Spectra are Captured as a Function of Delay From Beginning of Rf Pulse



ISSI

## Pertinent Bands are Identified for Fitting

Fits are Performed on Different Spectral Regions



ISSI

## Synthesize N<sub>2</sub> Spectrum for Fitting to Measured Data

- The intensity of an isolated rovibrational line can be written:

$$I_{v',j'}^{v'',j''} = N_{v',j'} A_{v',j'}^{v'',j''} \frac{hc}{\lambda_{v',j'}^{v'',j''}} = \frac{N_{v',j'} A_{v',j'}^{v'',j''}}{Q_r} S_{j'} e^{-E_j/kT} \frac{hc}{\lambda_{v',j'}^{v'',j''}}$$

- With a given line profile, the emission spectrum of the single line can be written:

$$L_{v',j'}^{v'',j''}(\lambda) = I_{v',j'}^{v'',j''} \phi(\lambda, \lambda_{v',j'}^{v'',j''})$$

- The measured profile, including the ILS, from the single line can then be written:

$$W_{v',j'}^{v'',j''}(\lambda) = \int_0^{\infty} I_{v',j'}^{v'',j''} \phi(\lambda', \lambda_{v',j'}^{v'',j''}) P(\lambda, \lambda') d\lambda' = I_{v',j'}^{v'',j''} P_c(\lambda, \lambda_{v',j'}^{v'',j''})$$

ISSI

## Synthesize N<sub>2</sub> Spectrum for Fitting to Measured Data (cont.)

- The measured spectrum from a single vibrational band can be written:

$$W_{v''}(\lambda) = \sum_{j''j'} I_{v''j''} P_i(\lambda, \lambda_{v''j''}^{j''j'}) = N_{v''} f_{v''}(\lambda, T)$$

- The *calculated* spectrum is therefore given by:

$$W(\lambda) = \sum_{v''} W_{v''}(\lambda) = \sum_{v''} N_{v''} f_{v''}(\lambda, T)$$

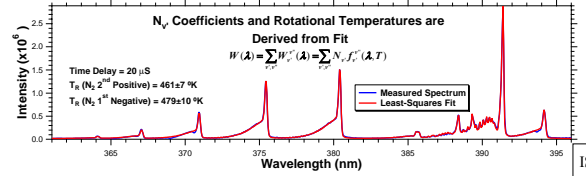
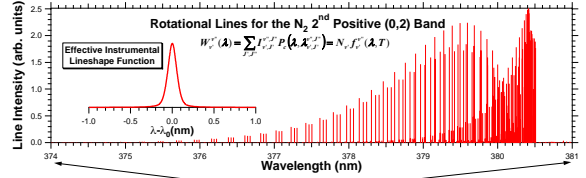
- The *measured* spectrum also includes an average over the extent of the plasma and can be written:

$$\langle W(\lambda) \rangle_x = \int W(\lambda, x) dx = \int W(\lambda, x, T(x)) dx$$

ISSI

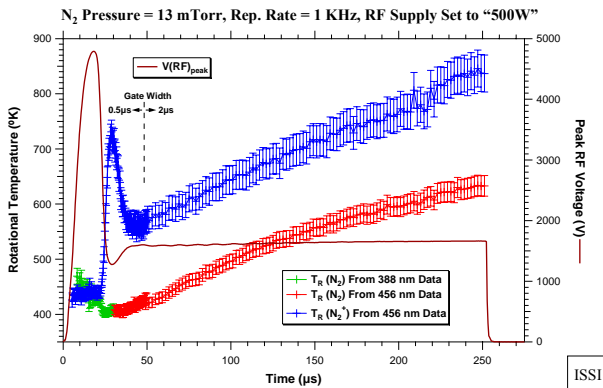
## Synthetic Spectrum is Least-Squares Fit to Measured Data

Rovibrational Lines are Convolved with Effective ILS



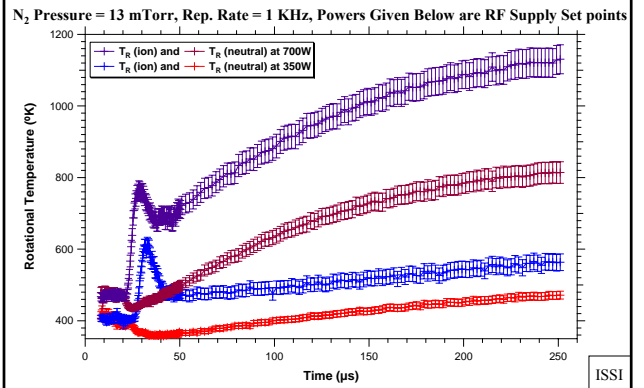
ISSI

## Temperature Derived From Spectra: Multiple Gate Widths; Two Spectral Regions

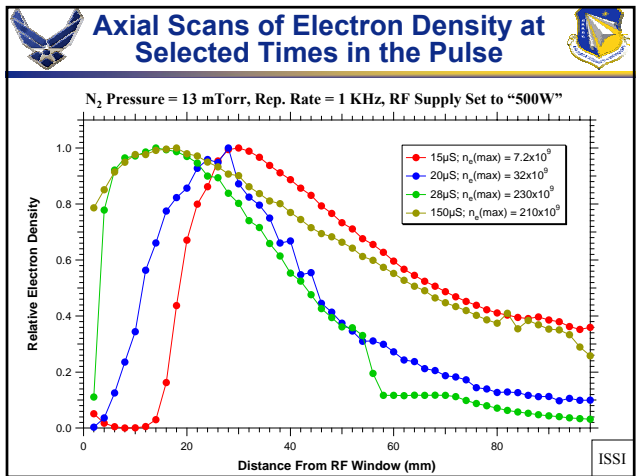
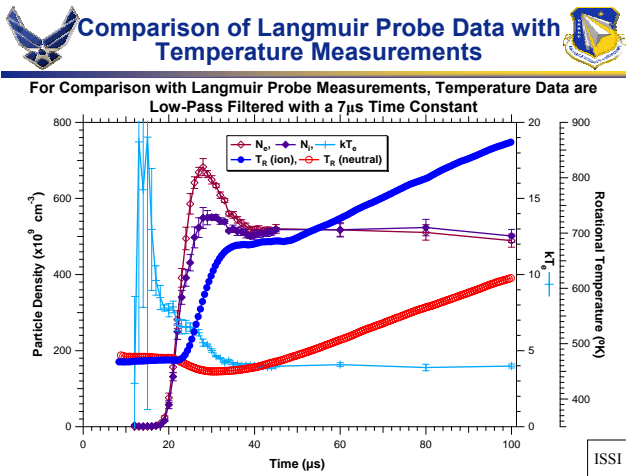
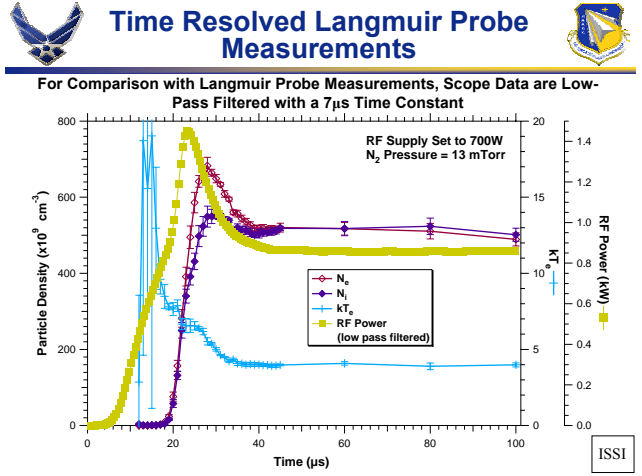
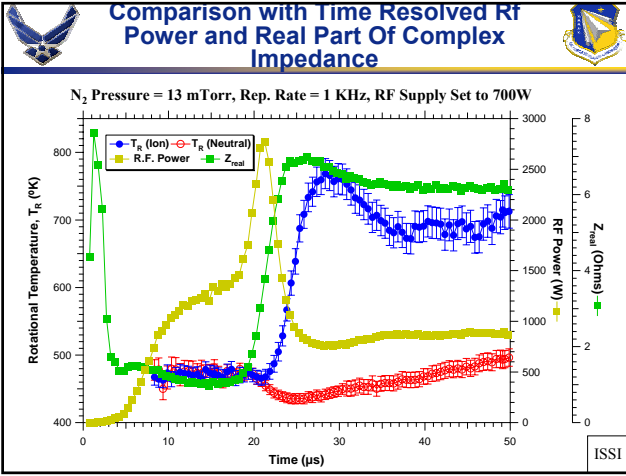


ISSI

## Effect of Rf Power on Rotational Temperatures



ISSI





## Summary and Conclusions



- Time resolved rotational temperatures have been determined from the  $N_2$  2<sup>nd</sup> positive emission and the  $N_2^+$  1<sup>st</sup> negative emission in a pulsed ICP at 1KHz repetition rate.
- Early in the pulse, the ion and neutral temperatures are approximately equal. The discharge is primarily capacitively coupled during this time.
- As the discharge transitions to the inductive mode, the ion temperature rises sharply above the neutral temperature and stays higher for the remainder of the RF pulse.
  - The temperature rise correlates with the rise in the real part of the complex impedance of the discharge.

ISSI

### TASK 3. STUDIES OF CHARGED-PARTICLE PROCESSES

In the performance of this task, ion chemistries have been studied in compounds including gases relevant to plasma-etching processes such as  $\text{CF}_3\text{Br}$ ,  $\text{CF}_3\text{I}$ ,  $\text{NO}_2$ ,  $\text{CH}_3\text{NO}_2$ ,  $\text{l-C}_4\text{F}_8$ , and  $\text{c-C}_5\text{F}_8$ , gases relevant to plasma-enhanced chemical-vapor deposition such as diethylzinc  $\text{Zn}(\text{C}_2\text{H}_5)_2$  and hexamethyldisiloxane ( $\text{Si}_2\text{OC}_6\text{H}_{18}$ ), and gases relevant to combustion such as  $\text{n-C}_8\text{H}_{18}$ ,  $\text{n-C}_{10}\text{H}_{22}$ ,  $\text{C}_{10}\text{H}_8$  (naphthalene),  $\text{C}_6\text{H}_6$  (benzene), Quadricyclane ( $\text{C}_7\text{H}_8$ ), JP-10 ( $\text{C}_{10}\text{H}_{16}$ , tetrahydrodicyclopentadiene), and  $\text{n-C}_4\text{H}_{10}$ . A study on pyridine ( $\text{C}_5\text{H}_5\text{N}$ ) was also carried out in collaboration with a research group at NASA that recently performed theoretical calculations on the ionization cross sections of benzene and pyridine as part of a program to investigate the role played by electron-impact dissociative ionization in the processes of DNA damage by space radiation. The results of the Task-3 effort have been documented in twelve refereed papers that have been published in scientific journals. The citations for these papers are given below, and reprints from the journal or conference proceedings in which they were published are included on subsequent pages.

- 1) "Comparisons of Electron Impact Ionization and Ion Chemistries of  $\text{CF}_3\text{Br}$  and  $\text{CF}_3\text{I}$ ," C. Q. Jiao, B. Ganguly, C. A. DeJoseph, Jr., and A. Garscadden, *Int. J. Mass Spectrom.* **208**, 127 (2001).
- 2) "A Mass Spectrometry Study of n-Octane: Electron Impact Ionization and Ion-Molecule Reactions," C. Q. Jiao, C. A. DeJoseph, Jr. and A. Garscadden, *J. Chem. Phys.* **114**, 2166 (1 February 2001).
- 3) "Electron Collision Processes in Nitrogen Trifluoride," C. Q. Jiao, P. Haaland, and A. Garscadden, in *Gaseous Dielectrics IX* (Proceedings of the Ninth International Symposium on Gaseous Dielectrics, May 21-25, 2001, Ellicott City, MD) (L. G. Christophorou and J. K. Olthof, Eds.) (Kluwer Academic/Plenum, New York, 2001), pp. 127-132.
- 4) "Collisions by Electrons and by Ions in the Ignition Process," C. Q. Jiao, C. A. DeJoseph, Jr., and A. Garscadden, AIAA Paper No. 2001-2950 presented at the Weakly Ionized Gases Conference, 11-14 June 2001, Anaheim, CA.
- 5) "Absolute Cross-Sections for Electron Impact Ionization of  $\text{NO}_2$ ," C. Q. Jiao, C. A. DeJoseph, Jr., and A. Garscadden, *J. Chem. Phys.* **117**(1), 161 (1 July 2002).
- 6) "Formation of Positive and Negative Ions in  $\text{CH}_3\text{NO}_2$ ," C. Q. Jiao, C. A. DeJoseph, Jr., and A. Garscadden, *J. Phys. Chem. A* **107**(42), 9040 (23 October 2003).
- 7) "Ion Chemistry in Diethylzinc," C. Q. Jiao, C. A. DeJoseph, Jr., and A. Garscadden, *Int. J. Mass Spectrom.* **235**(1), 83 (June 2004).
- 8) "Ion Chemistries in Hexamethyldisiloxane," C. Q. Jiao, C. A. DeJoseph, Jr., and A. Garscadden, *J. Vac. Sci. Technol. A: Vac. Surf. Films* **23**(5), 1295 (September 2005).

- 9) "Ion Chemistry in Quadricyclane," R. Lee, C. Q. Jiao, C. A. DeJoseph, Jr., and A. Garscadden, *J. Phys. D: Appl. Phys.* **38**(18), 3550 (21 September 2005).
- 10) "Ionization of Octafluorocyclopentene,  $c\text{-C}_5\text{F}_8$ ," C. Q. Jiao, C. A. DeJoseph, Jr., and A. Garscadden, *J. Phys. D: Appl. Phys.* **38**(7), 1076 (7 April 2005).
- 11) "Kinetics of Electron Impact Ionization and Ion-Molecule Reactions of Pyridine," C. Q. Jiao, C. A. DeJoseph, Jr., R. Lee, and A. Garscadden, In Press, *International Journal of Mass Spectrometry* (2006).
- 12) "Charge Transfer Reactions in Xe Plasma Expansion," C. Q. Jiao, A. Garscadden, and B. N. Ganguly, Submitted to *Journal of Applied Physics*.

Another paper entitled, "Ion Chemistries in  $n\text{-C}_4\text{H}_{10}$ ," is in preparation for submission to the *International Journal of Mass Spectrometry*.

In addition to the studies mentioned above, the following instrument improvements have been made and experimental methods developed during this reporting period:

- (1) A modified Fourier Transform Mass Spectrometer (FTMS) trapping cell was successfully constructed; screen electrodes were added in front of the two original trapping plates. The purpose of the additional electrodes was to provide a very shallow trapping well in most of the volume of the cell while still maintaining a steep potential drop at the edges of the cell; in this way, high trapping voltages can be applied to the cell for collecting most of the kinetically energetic ions and, at the same time, maintaining the electron-energy dispersion sufficiently small to permit fine energy-resolved cross-section measurements.
- (2) The gas manifold was replaced with one having two sections (upper and lower sections, each connecting to a leak valve) with the same volume for mixing gases in situations where the sample gases have significant non-ideal gas behavior. Two different gases can be placed separately into the two sections of the manifold and then allowed to mix for achieving the desired pressure ratio.
- (3) An electron cup was added to the trapping-cell assembly for improving the accuracy of measuring the electron current at high electron energies.
- (4) The trapping cell was re-aligned with the magnetic field to achieve greater linearity of the ion motions in the cell.
- (5) A new preamplifier was added to the FTMS hardware to increase the mass limit of ion detection. With this preamplifier the mass of the ion to be detected can be as low as 1 amu without application of a calibration factor for accurate quantification of the ion current. Previously, the lower mass limit was  $\sim 15$  amu.

(6) The FTMS database system has been upgraded on two occasions. With each upgrade the FTMS experiments could be performed more efficiently, quickly, and automatically.

(7) A new experimental method was developed that allows the study of a mixture of Ar with a gas of interest at a ratio as high as 100:1. The partial pressure of Ar, therefore, can be raised up to  $5 \times 10^{-6}$  Torr for the purpose of thermalizing energetic ions. This technique enables the study of chemistries of thermalized ions rather than the unknown excited states of ions.

(8) An FTMS technique called collision-induced dissociation (CID) was adapted for the purpose of probing the fragmentation paths in dissociative electron-impact ionization and the composition or structure of product ions. New experimental protocols were developed and computer programs revised.

(9) Another FTMS technique called trapping-potential dependence was adapted for the purpose of examining the ion-kinetic-energy profiles. In addition to providing information on the ion kinetic energy, this technique also permits calibration of the intensities of kinetically excited ions that are formed by electron-impact ionization in the trapping cell.

## **APPENDIX**

### **Ohio University Final Report on the Development of Nitride Thin Films by Ion-Beam Deposition**

## Final Report on the Development of Nitride Thin Films by Ion Beam Deposition

Funded by AFOSR through ISSI, F33615-00-C-2055

Start 15 Nov 2000 End 30 Apr 2005

The purpose of this grant was to characterize nitride thin films that were deposited by ion beam deposition. Specifically, carbon nitride, boron nitride and aluminum nitride thin films would be deposited by ion beam techniques and their physical, electrical and optical properties would be determined. To guide the work, reviews were undertaken of the literature on ion beam deposition of these materials. These reviews were attached to earlier reports and will not be reproduced here or attached to this report. From these reviews it was concluded that the majority of the work should concentrate on carbon nitride material as that is where we could make the most impact in terms of characterization of the material. This was because of the work already undertaken by others on aluminum nitride and boron nitride and because depositing these materials would entail setting up an additional ion source to sputter the metal component. We knew that this would considerably increase the complexity of the depositions and the time to deposit a sample. This was later shown to be true when ion beam assisted films were made using sputtered carbon as the source of the carbon in the carbon nitride films.

The work on characterization of carbon nitride deposited by ion beam techniques has been extensive during this program. At Ohio University we have received nearly 200 samples over the lifetime of the contract and for each sample have acquired at least 3 spectra and in some cases more than 10 spectra in order to track their behavior as a function of heat treatment, or to check on the uniformity of a particular approach to making the samples.

The contract has also supported a Ph.D. student for three years, who graduated in 2004. His thesis was titled "Deposition and Characterization of Diamond-Like Films with and without Hydrogen and Nitrogen". He did much of the ion beam analysis work for this contract. He was a co-author on the 5 papers published. He was able to complement the work on this contract with his own study of the properties of carbon nitride films deposited by unbalanced-biased magnetron (UBM) sputtering. He showed that the properties of the films did not depend on the technique used to deposit them but on the final composition and to some extent the energy available during the deposition process. UBM sputtering is somewhat similar to ion beam assisted deposition in that not only are hyper-thermal species deposited on the substrate but, because of the unbalance magnetic field supporting the plasma, the plasma extends to close to the surface of the substrate. Thus, with the aid of a potential applied to the substrate it is possible to bombard the substrate with ions from the plasma. Thereby creating an environment similar to that found under low energy ion beam assisted deposition.

Shown in **Figure 1** are the possible variations in composition that can be achieved by the different techniques used in this study. Each apex of the triangle represents a material of 100% of that element, so diamond or graphite would be at the top of the triangle. Each edge represents varying the composition of the film between two elements with none of the third element present. So that polyethylene is about two thirds of the way down one side of the C-H edge and represents the

upper limit on  $\text{CH}_x$  diamond-like carbon (DLC) films. Along the C-N edge can be found  $\text{C}_3\text{N}_4$  and it can be seen that we have never achieved that ratio of carbon to nitrogen. The highest percentage of nitrogen was achieved ( $\sim 40\%$ ) with ion beam sputter of graphite with a nitrogen beam while bombarding the growing film with a nitrogen beam.

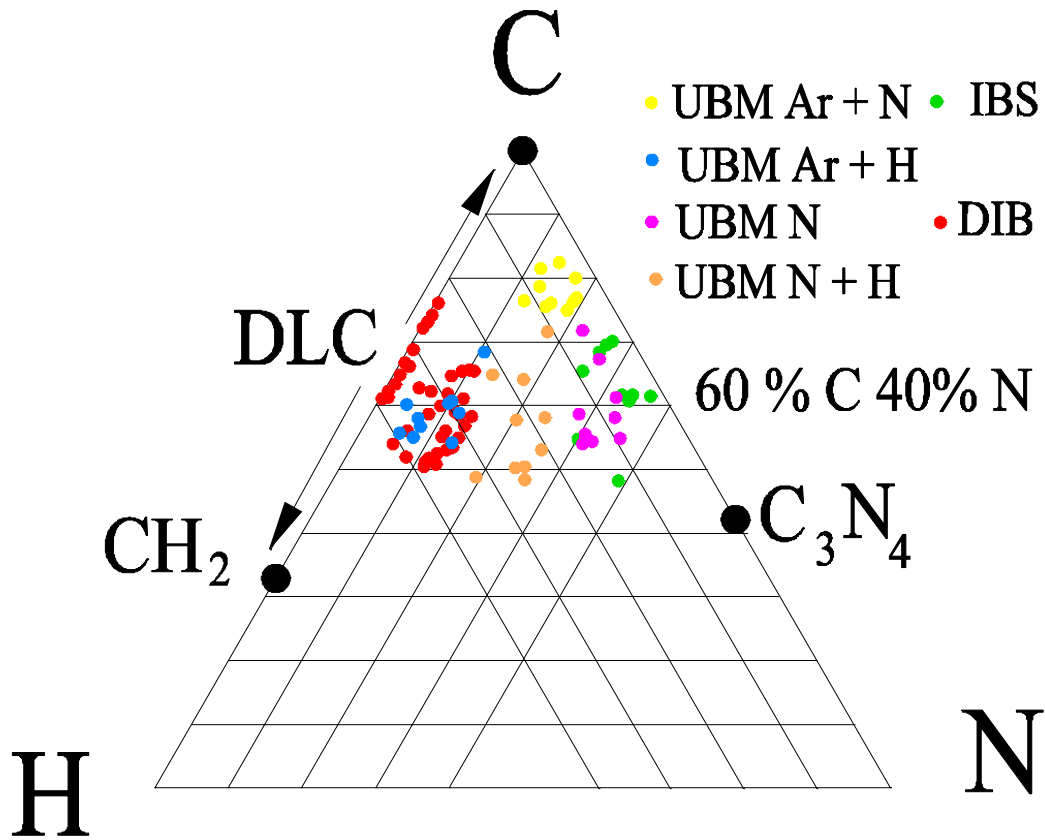


**Figure 1. Phase diagram of stoichiometries of materials deposited by both ion beam techniques and unbalanced-biased magnetron sputtering.**

One of the objectives of the Ph.D. study was to study the effect of adding nitrogen to DLC films to see if in small quantities could dope these films just as other members of group 15 (old group 5) of the periodic table can be n-type dopants of amorphous or polycrystalline silicon or germanium. The result of this work was that as soon as nitrogen is added in significant amounts ( $>1\%$ ) to the DLC films, the band gap falls, as shown in **Figure 2**. The graph shows the compensating effect of hydrogen, in most semiconducting materials, as well as showing that the presence of nitrogen introduces traps in the band gap, shown by the increasing width of the Urbach tail.

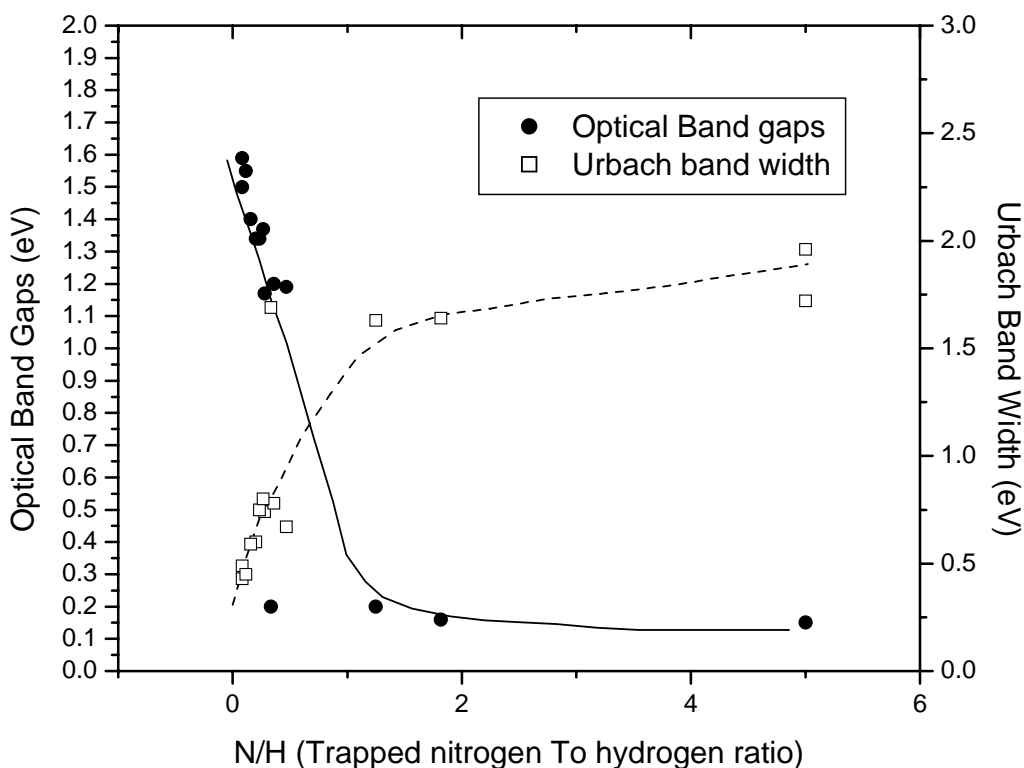


**Figure 2. UV-visible optical band gap data as a function of nitrogen to hydrogen ratio.**

Thus, the general result appears to be that adding nitrogen will lead to a conducting material but not through a simple doping mechanism in which there is a defined activation energy but through the insertion of states into the gap at many different levels. The underlying message is that the C-N bonds are not in the form that we need for the insulating material predicted by the theory of Liu and Cohen<sup>1</sup>, and that some other parameter is going to need to be changed before we can create those bonds, either the precursor material, or the temperature of the substrate during the deposition. These could both be avenues for future work.

There are instances in our own work, and in the work of others, of  $CN_x$  films that are insulating but these may be due to the presence of  $CH_x$  layers introduced inadvertently or by design<sup>2</sup>. One direction this work could proceed in is to examine the properties of multilayer structures since these multilayer structures could have interesting electronic properties. However, as Cameron has pointed out there are “many conflicting conclusions about the effect of nitrogen in the carbon

matrix.”<sup>3</sup> From the work of Baker et al.<sup>4</sup> it appears that deposition temperature is a critical parameter when trying to achieve high resistivity material. They went as low as 80 K to achieve insulating-like material, and needed to go down to 140 K to exceed  $10^9$  ohm.cm.

In addition to examining the properties and composition of the films as-deposited, we have also examined the stability of the films and in particular the stability of hydrogen, which in DLC is a marker of changes in those films from insulating to conducting, as hydrogen is lost. One curiosity of this work was that above 600°C there was significant uptake of hydrogen in the films. This was eventually shown to be probably due to hydrogen diffusing through the quartz tube used in the furnace and being trapped in the films. This suggests that these films may be able to catalyze the production of atomic hydrogen since the gas will arrive on the surface of the growing film as a molecule but most likely diffuse as an atom.

As part of the work on this contract, we have built an electrical measurement system that enabled us to make resistivity measurements through the film, as well as across the film, and as a function temperature down to 50K. The electrical measurements we have made on some of our films exhibit Frenkel-Poole conduction. This is a process in which the conductivity is not Ohmic but also not Schottky. The process is controlled by the electric field in the material and is somewhat like electric field emission at a surface in that the number of carriers, and hence the conductivity, is affected by the electric field in the material. Normally only the drift velocity is affected by the electric field strength but through this mechanism the number of carriers increases in proportion to the electric field.

In summary, we have made significant contributions to the understanding of DLC and carbon-nitride films and how they are related. We have shown that UBM and ion beam assisted deposition can both deposit similar films over a wide range of deposition conditions but that the ion beam approach does offer better control. There have been many results published from this work, a Ph.D. student has been educated through this contract and is contributing to the scientific community in the US, and the research infrastructure at Ohio University has been improved and expanded.

1 A.Y. Lui, M.L. Cohen, “Structural properties and electronic structure of low-compressibility materials:  $\beta$ -Si<sub>3</sub>N<sub>4</sub> and hypothetical  $\beta$ -C<sub>3</sub>N<sub>4</sub>”, Phys. Rev. B 41 (1990) 10727

2 M. Aono, S. Nitta, “High resistivity and low dielectric constant amorphous carbon nitride films: application to low-k materials for ULSI”, Diamond and Related Materials 11 (2002) 1219

3 D.C. Cameron, “Optical and electronic properties of carbon nitride”, Surface and Coatings Technology 169-170 (2003) 245

4 M.A. Baker \*, P. Hammer, C. Lenardi, J. Haupt, W. Gissler, “Low-temperature sputter deposition and characterisation of carbon nitride films”, Surface and Coatings Technology 97 (1997) 544